공학박사 학위논문

평면 이온 트랩에 레이저로 인해 유도된 전하의 위치 파악 방법 개발

Development of a Method for Estimating Locations of Laser-Induced Stray Charges in Surface-Electrode Ion Traps

2023년 8월

서울대학교 대학원

전기 · 정보공학부

정 창 현

평면 이온 트랩에 레이저로 인해 유도된 전하의 위치 파악 방법 개발

지도 교수 조동일

이 논문을 공학박사 학위논문으로 제출함
2023년 6월

서울대학교 대학원
전기 · 정보공학부
정창현

정창현의 공학박사 학위논문을 인준함
2023년 6월

위원장 박남규

부위원장 조동일

위원 정윤찬

위원 김태현

위원 최태영

감사의 글

길고 긴 대학원 생활의 끝자락에 서니, 마치 군대를 제대할 때와 같이 시원섭섭한 마음이 드는 것 같습니다. 수많은 좋은 분들을 만날 수 있었고, 그분들에게 많은 것들을 배울 수 있었습니다. 특히, 저의 지도 교수님이신 조동일 교수님께 진심으로 감사드립니다. 조동일 교수님의 희생과 지원 덕분에 대학원 생활을 무사히 마칠 수 있었습니다. 교수님을 만나 뵙고 교수님께 지도를 받을 수 있었던 건 저에게 정말 큰 행운이었고, 교수님께 지도를 받는 과정에서 많은 성장을 할 수 있었습니다. 특히, 모든 현상을 가장 기본적이고 일반적인 전제부터 생각할 수 있는 힘을 기를 수 있었고, 결과적으로 고정 관념을 갖고 틀에 박혀 생각하는 잘못된 습관을 고칠 수 있었습니다. 졸업한 이후에 새로운 삶을 살아가는 과정에서도 교수님께 받은 가르침과 은혜를 잊지 않고, 항상 겸허하고 감사한 마음을 가지고 살도록 하겠습니다.

제 마음속 제2의 지도 교수님이신 김태현 교수님께도 감사의 말씀을 올리고 싶습니다. 회사에 계실 때부터 많은 도움과 가르침을 주셨습니다. 특히, 김태현 교수님께 깊이 생각하는 방법을 배울 수 있었습니다. 교수님의 도움 덕분에 연구를 무사히 마칠 수 있었고, 대학원에서의 많은 일들을 무탈하게 넘길 수 있었습니다. 사실 교수님과 있었던 일 중 가장 기억에 남는 일은, 교수님과 두레미담에서 저녁 식사를 하며 결혼에 대한 대화를 나눴던 일입니다. 당시 교수님과 대화하며 인생의 선배로부터 현실적인 조언을 들을 수 있었고, 동시에 향후 제가 미래에 어떻게 결혼 생활을 해야 할

것인가에 대하여 재고하는 시간을 가질 수 있었습니다.

앞선 두 분의 교수님과 함께 논문 심사를 수락해 주신 박남규 교수님과 정윤찬 교수님, 최태영 교수님께도 감사의 인사를 드립니다. 교수님들께서 바쁘신 와중에도 논문 심사에 참석해 주시고, 좋은 말씀들을 남겨주신 덕분에 더욱 행복한 심사가 될 수 있었습니다.

저의 영원한 사수이자, 정신적 지주가 되어준 석준이형에게 감사합니다. 같이 이온 트랩 공정을 하던 2년 반이라는 시간 동안 공정뿐만 아니라 삶에 대해서도 배울 수 있었습니다. 또한, 졸업한 이후에도 많은 조언과 도움을 주셔서 더욱 감사합니다. 졸업한 민재형과 윤재형, 홍진이형, 욱이형, 형정이형, 태재형, 서형이형, 태일이형, 지석이형, 훈이형, 종민이형, 종윤이형, 민기, 진우, 승현이, 현택이, 태훈이에게도 감사합니다. 덕분에 연구실에서 많은 추억을 쌓을 수 있었습니다. 대학원 생활 마지막까지 함께 한 준호에게도 고맙습니다. 혼자 했으면 더욱 힘들 뻔했던 길을 함께해 준 덕분에 덜 힘들었습니다. 대학원 동기인 철홍이형에게도 고맙고, 먼저 졸업한 동기인 지호에게도 고맙습니다. 함께 롤도 하고 맛있는 것도 먹어준 태호와 영석이, 대영이에게도 고맙고, 연구실에서 희로애락의 시간을 함께 보낸 태엽이와 정현이에게도 고맙습니다.

대학원 생활 전반전에 한창 공정할 때, 많은 도움을 주셨던 서울대 반도체공동연구소의 김조원 선생님과 박종승 선생님, 김건주 선생님, 이규 선생님, 김진경 선생님, 장래혁 선생님, 박유경 선생님, 최종윤 실장님께 감사합니다. 청정실에서 방진복을 뒤집어쓴 와중에도 선생님들과 인사하고 대화하면, 답답함이 해소되고 기분

전환되는 일도 많았습니다.

긴 대학원 생활 동안 경제적, 정신적 지원을 해 주신, 사랑하고 존경하는 부모님께 정말 감사드립니다. 제가 혹시나 부담을 갖게 될까 봐 늘 저를 먼저 배려해 주시고 무한한 응원을 해주시며, 지친 마음으로 주말에 집에 갈 때마다 늘 따뜻하게 반겨 주셨습니다. 대학원 생활 후반전에 졸업이 늦어지는 저를 바라보시며 속상해하는 일이 많으셨을 텐데, 앞으로는 좋은 기억만 남겨드릴 수 있는 아들이 되도록 노력하겠습니다.

얼마 전에 튼튼이를 출산한 누나와 자형에게도 고맙습니다. 4년 터울이라 학창 시절부터 성인 시절까지 많은 시간을 보내진 못했지만, 늘 응원하고 있다는 사실을 알아줬으면 좋겠습니다. 앞으로 한 아이의 부모님으로서 살아갈 누나와 자형을 응원하겠습니다.

대학원 생활 후반의 시간을 함께 견뎌준, 사랑하는 여자친구 홍지은에게도 감사합니다. 2020년 6월 30일부터 함께 시간을 보내며, 대학원에서 지친 마음의 빛 이자 오쏘몰이 되어주었습니다. 특히, 대학원에서 일이 잘 안 풀려서 지치고 힘들 때, 지은이를 만나면 특유의 밝음과 사랑스러움 덕분에 다시 앞으로 나아갈 힘을 얻을 수 있었습니다. 지은이가 제 곁에서 항상 응원해 주고 힘이 되어준 만큼, 저도 지은이에게 힘이 되어줄 수 있고 행복을 줄 수 있는 사람이 되도록 노력하겠습니다.

주변에서 도움을 준 모든 분들에게 감사를 표합니다.

2023년 6월 30일

Abstract

The development of a universal quantum computer based on surface-electrode ion traps has gained significant attention in recent years due to their scalability, reproducibility, and integration capabilities. However, the small distance between trapped ions and the nearest electrode renders these traps highly sensitive to even slight variations in surrounding electric fields. Of particular concern is the issue of stray electric fields originating from the trap surface, which can induce undesired micromotion of the ions and have a detrimental impact on the fidelity of quantum-gate operations.

A laser-induced stray charge is one of the sources that cause stray electric fields at the location of trapped ions. The stray charge typically occurs when photoelectrons emitted from electrode surfaces accumulate on nearby dielectric surfaces. Since the amount of laser-induced stray charges varies over time, it becomes challenging to keep the stability of trapped ions over extended periods solely by compensating for previously observed stray electric fields, and therefore periodic compensation for the stray electric fields is required. Additionally, ion traps commonly utilize high-frequency lasers, which raises the possibility of stray charges being generated by the lasers. When the laser-induced stray charges become problematic, the suppression of such charges is inefficiently achieved by adjusting the laser propagation paths using trial and error, as the locations of the stray charges are unknown.

In this dissertation, a method for estimating the locations of laser-induced stray charges in surface-electrode ion traps is developed. How the electric potential at the ion location changes in the presence of an electric charge is theoretically modeled, and the resulting shift in the secular frequency is derived from the potential change. By analyzing the secular frequency shift, the model enables inverse estimation of stray charge locations under certain conditions. Specifically, measurements of the secular frequency shift can be performed at multiple ion locations in surface-electrode ion traps, resulting in the unique determination of stray charge locations. To verify the effectiveness of the proposed method, simulations are conducted for scenarios where stray charges occur at various locations, and the resulting secular frequency shifts are observed at multiple ion positions. The locations of stray charges are then estimated from the secular frequency shifts observed in the simulation results, and the estimated locations are compared with those derived from the theoretical model. Experimental evaluation of the proposed method is also carried out by intentionally producing electric charges at a single location using a laser, and by measuring the resulting secular frequency shift. The location of produced charges is estimated from the measurement result, and the estimated location is consistent with the spot where the laser is irradiating. The results show that the developed method is capable of accurately determining the locations of laser-induced stray charges in surface-electrode ion traps, which can contribute to enhancing the reliability and stability of ion-trap quantum computing systems efficiently.

Keywords: laser-induced stray charge, location of stray charge, surface-electrode ion trap, trapped ion, secular frequency

Student Number: 2016-20975

Contents

List of Figures

List of Tables

Chapter 1

Introduction

1-1. Quantum Information Basics

The quantum bit (qubit) is a fundamental element of quantum information processing. In contrast to classical bits, which can only exist in the states $|0\rangle$ or $|1\rangle$, the qubit can exist in an arbitrary superposition of states, denoted as:

$$|\psi\rangle = \alpha|0\rangle + \beta|1\rangle, \tag{1.1}$$

where α and β are complex numbers, and $|\alpha|^2 + |\beta|^2 = 1$, representing the probability amplitudes of the qubit being in the $|0\rangle$ and $|1\rangle$, respectively. Both $|0\rangle$ and $|1\rangle$ are vectors in a two-dimensional complex vector space, which corresponds to an orthonormal basis in this vector space. The superposition property of qubits allows for their unique computational capabilities in quantum information processing (QIP).

Two classical bits can only represent one of the following four configurations ($|00\rangle$, $|01\rangle$, $|10\rangle$, and $|11\rangle$). However, two qubits can simultaneously represent four states as follows:

$$|\psi\rangle = \alpha_{00}|00\rangle + \alpha_{01}|01\rangle + \alpha_{10}|10\rangle + \alpha_{11}|11\rangle. \quad (1.2)$$

Similar to the single qubit, each state is measured with a probability of $|\alpha_x|^2 (x \in \{00,01,10,11\})$, and the sum of $|\alpha_x|^2$ is 1. In general, N qubits can represent 2^N states simultaneously. When measuring quantum systems, the quantum state collapses, and a random output is obtained. However, as Feynman pointed out, the exact probability of each state can be determined by repeating the same measurement multiple times.

Quantum gates that are commonly used in quantum computing include the Pauli gate, the controlled-NOT (CNOT) gate, and the Mølmer-Sørenson gate. The Pauli gate is a single-qubit gate represented by σ_x, σ_y, and σ_z matrices, which can be expressed as follows:

$$\sigma_x = \begin{bmatrix} 0 & 1 \\ 1 & 0 \end{bmatrix}, \sigma_y = \begin{bmatrix} 0 & -i \\ i & 0 \end{bmatrix}, \sigma_z = \begin{bmatrix} 1 & 0 \\ 0 & -1 \end{bmatrix}. \quad (1.3)$$

Among these, σ_x is analogous to the classical NOT gate, and σ_z is known as the phase-flip gate. The two-qubit CNOT gate is represented by the matrix shown below:

$$\text{CNOT} = \begin{bmatrix} 1 & 0 & 0 & 0 \\ 0 & 1 & 0 & 0 \\ 0 & 0 & 0 & 1 \\ 0 & 0 & 1 & 0 \end{bmatrix}. \quad (1.4)$$

In other words, if the CNOT gate is defined as $\hat{U}_{CNOT}$, it operates as follows:

$$\hat{U}_{CNOT}|00\rangle = |00\rangle$$

$$\hat{U}_{CNOT}|01\rangle = |01\rangle$$

$$\hat{U}_{CNOT}|10\rangle = |11\rangle$$

$$\hat{U}_{CNOT}|11\rangle = |10\rangle. \tag{1.5}$$

When the first qubit is $|1\rangle$, then the second qubit is flipped. Two-qubit gates, such as the CNOT gate, are closely related to quantum entanglement. When two qubits are entangled, their quantum states cannot be separated. For instance, if the two quantum states A and B are described by the following equation:

$$|\psi\rangle = \frac{1}{\sqrt{2}}(|0\rangle_A|0\rangle_B + |1\rangle_A|0\rangle_B), \tag{1.6}$$

the state is not entangled, as it can be factored into:

$$|\psi\rangle = \frac{1}{\sqrt{2}}(|0\rangle_A + |1\rangle_A)|0\rangle_B. \tag{1.7}$$

Thus, the measurement result of A does not affect the state of B. Conversely, the following state is entangled:

$$|\psi\rangle = \frac{1}{\sqrt{2}}(|0\rangle_A|0\rangle_B + |1\rangle_A|1\rangle_B). \tag{1.8}$$

In this case, measuring the state of A would affect the state of B.

To be utilized as a physical system for quantum computing using the qubits and quantum gates discussed earlier, David DiVincenzo proposed five conditions in 2000 [1]:

- A scalable physical system with well-characterized qubits
- State initialization of qubits
- Long coherence times
- A universal set of quantum gates
- Capability of qubit measurements

Several physical systems have been developed that meet these requirements. For example, optical systems such as photons [2], solid-state systems such as quantum dots [3] or superconductors [4], and atomic systems using neutral atoms [5] and trapped ions [6] have been extensively studied. The optical systems are capable of easily implementing quantum entanglement using spontaneous parametric down-conversion. However, confining photons poses a challenge, requiring a second system for information storage. The solid-state systems are scalable and exhibit fast quantum gate operations, but suffer from relatively short coherence times on the order of milliseconds, and routing for measuring the multiple quantum state is challenging. Atomic systems, on the other hand, offer isolated internal states from the surrounding environment, and are amenable to the manipulation of atomic qubits using lasers or microwaves [7, 8]. Although neutral atoms have a limitation in terms of their short lifetime, trapped ions can have relatively long lifetimes and coherence times [9], and have demonstrated a large number of entangled states [10]. This makes the trapped-ion system one of the promising candidates for implementing QIP.

1-2. Ion Trap

This section provides an overview of ion traps, including a brief history, ion species commonly used in trapped-ion experiments, and types of ion traps, as described in Section 1-2-1. It also discusses the development of surface-electrode ion traps, which are extensively studied for their potential in realizing quantum computers, as described in 1-2-2.

1-2-1. Ion Trap Overview

The ion trap utilizes combinations of either an oscillating electric field and an electrostatic field or a static magnetic field and an electrostatic field to confine charged particles in space. Originally studied in the 1950s for use as a mass spectrometer [11], the ion trap gained significant interest in the 1990s after confirming that qubits can be implemented using the internal (electronic) states of trapped ions. This has led to various applications in QIP, such as quantum computers [12], quantum simulators [13], and quantum machine learning [14], using ion qubits.

The ion trap is divided into two types, one is the Paul trap which uses an oscillating electric field and an electrostatic potential [15], and the other is the

Penning trap which utilizes a static magnetic field and an electrostatic potential [16]. Of the two types, linear Paul traps are typically used in the development of quantum computers [17], although there have been recent reports of research cases using the Penning trap for quantum computing [18]. In both types of traps, photo-ionized atoms are laser-cooled, and the resulting ion crystal performs quantum computation. The trap depth of the ions is typically high, allowing the atoms to remain inside the trap over a long time.

Two stable energy levels of a single trapped ion are used as qubits. Figure 1-1 shows the ion types commonly used for quantum computing, which can be categorized into optical qubits composed of quadrupole transitions, such as $^{40}\mathrm{Ca}^{+}$ [19], $^{88}\mathrm{Sr}^{+}$ [20], and $^{138}\mathrm{Ba}^{+}$ [21], and hyperfine qubits composed of hyperfine transitions in the ground state with non-zero nuclear spins, such as $^{25}\mathrm{Ma}^{+}$ [22], $^{43}\mathrm{Ca}^{+}$ [23], $^{137}\mathrm{Ba}^{+}$ (or $^{133}\mathrm{Ba}^{+}$) [24], and $^{171}\mathrm{Yb}^{+}$ [25]. The lifetime of electrons in an excited state in optical qubits is limited to only a few to tens of seconds, which is a disadvantage compared to hyperfine qubits that have reported coherence times of several tens of minutes [26]. However, the optical qubits have a low probability of interacting with the cooling cycle transition, which makes them suitable for achieving high fidelity in qubit manipulation.

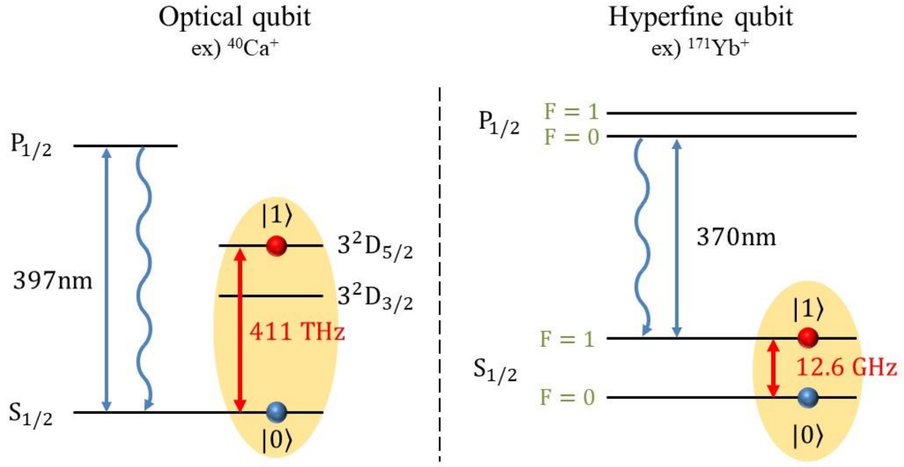

Figure 1-1. Energy level diagrams of an optical qubit and a hyperfine qubit. The optical qubit shows the energy level diagram of $^{40}Ca^+$, whereas the hyperfine qubit illustrates the diagram of $^{171}Yb^+$. The yellow circles indicate the qubit transitions.

The Paul trap can be categorized into different types, including the ring trap, linear trap, and surface trap [27]. The ring trap applies an RF voltage to the hyperbolic electrode, with the endcap electrodes on the top and bottom serving as the RF ground, as illustrated in Figure 1-2. The ring trap was commonly used in the early stages of ion trap research for basic physics experiments, such as frequency standards and mass spectrometers [28, 29]. However, the ring trap has limitations in terms of manipulating a large number of ion qubits and expanding to three dimensions.

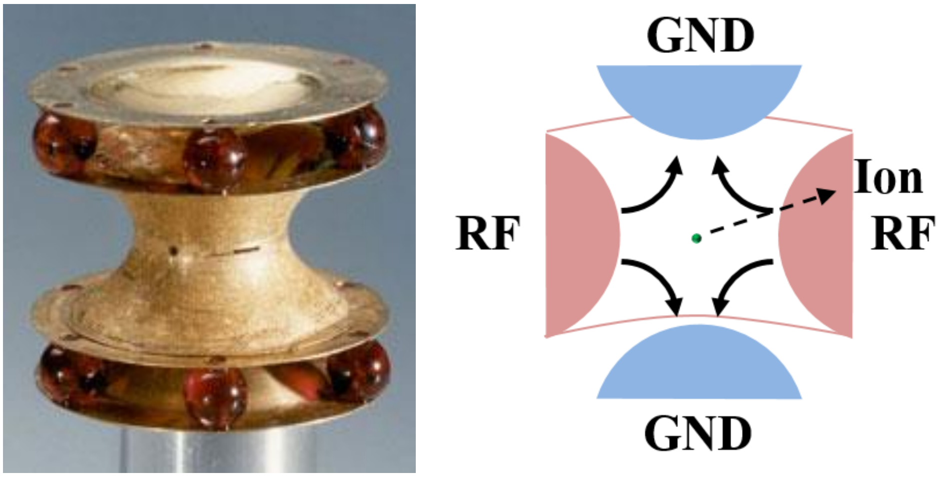

(a) (b)

Figure 1-2. Picture and schematic of the ring trap. (a) The picture of a ring trap made by Wolfgang Paul [15]. An ion is trapped inside the ring trap. (b) The schematic of the ring trap. The black arrows show the direction of the electric field when the RF voltage is positive.

To address the scalability limitation of the ring trap, the linear trap was developed by replacing the hyperbolic electrode with a linear one [30]. In the linear trap, as depicted in Figure 1-3, an RF voltage is applied to two of the four cylindrical electrodes diagonally, while a DC voltage is applied to the other two opposite diagonals, creating a pseudopotential with an RF null parallel to the longitudinal direction of the RF electrode. However, since the pseudopotential alone cannot confine the ions in the axial direction (the longitudinal direction of the RF electrode), endcap electrodes are added at both ends of the rod electrode, and a DC voltage is applied to confine the ions axially [31].

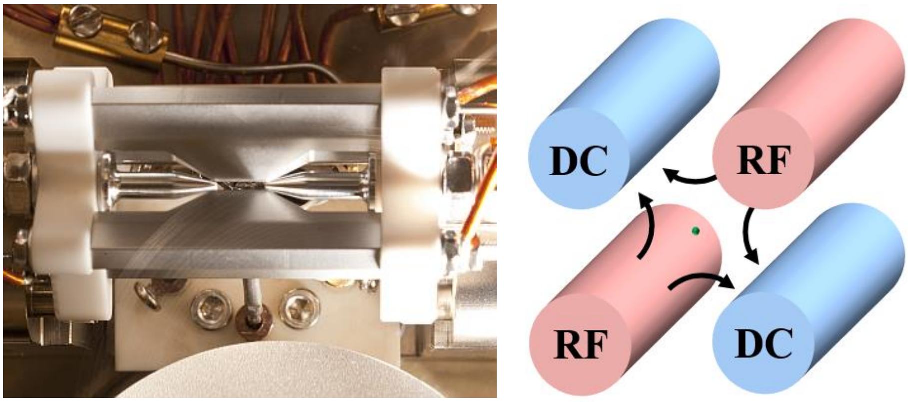

(a) (b)

Figure 1-3. Picture and schematic of the linear trap. (a) The picture of a blade trap made by the University of Innsbruck [32]. (b) The schematic of the 4-rod linear trap. The red and blue rods indicate RF and DC electrodes, respectively. The black arrows show the direction of the electric field when the RF is positive.

After the pioneering work of Cirac and Zoller in physically implementing quantum computation using trapped ions, numerous research groups have conducted QIP experiments using the linear trap. These groups have employed different electrode structures, including the rod [31, 33], blade [32, 34], and sheet [35] geometries. However, the fabrication and assembly processes for linear traps depend on the specific machining or assembly capabilities of each group, which can introduce risks of misalignment and other errors. Moreover, scalability is limited in linear traps as there is a maximum number of ions that can be confined linearly, and precise control of ion positions or spacing is challenging. To overcome these limitations, surface-electrode ion traps have been developed as an alternative approach.

1-2-2. Development of Surface-Electrode Ion Traps

The surface-electrode ion trap is a three-dimensional (3D) linear trap implemented on a two-dimensional (2D) plane using microfabrication technology [36, 37]. As shown in Figure 1-4, it achieves an RF null in a direction parallel to the longitudinal direction of the RF electrode by incorporating DC electrodes both inside and outside the RF electrodes. Unlike the linear trap, where axial confinement is achieved by endcap electrodes at both ends of the RF electrode, the surface-electrode ion trap can achieve axial confinement through DC voltages applied to the segmented outer DC electrodes [38].

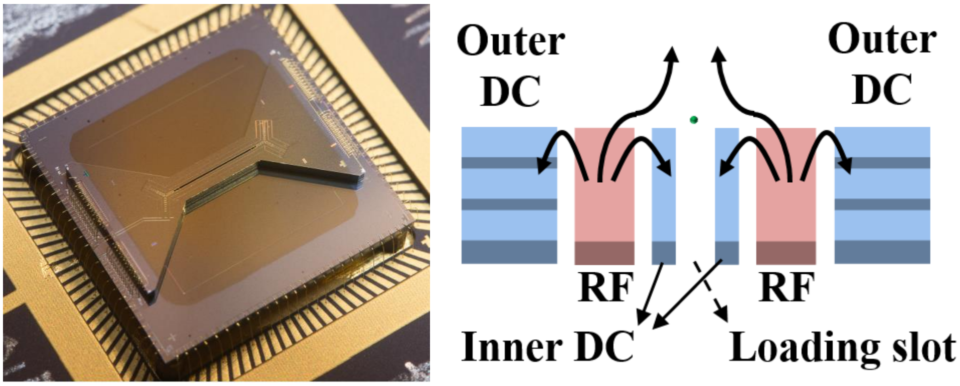

(a) (b)

Figure 1-4. Picture and schematic of the surface-electrode ion trap. (a) The picture of a surface-electrode ion trap made by Sandia [39]. (b) The schematic of a surface-electrode ion trap. The green dot indicates a single trapped ion. The blue and red regions show DC and RF electrodes, respectively. Black arrows indicate the direction of electric fields when the RF voltage is positive.

The surface-electrode ion trap is made using microfabrication technology or microelectromechanical system (MEMS) fabrication technology, which offers advantages in reproducibility [40] and miniaturization [41, 42], and enables the implementation of complex structures [43–45]. In addition, the surface-electrode ion trap can be fabricated using various substrate materials, such as silicon [46–48], GaAs [49], quartz [50, 51], and sapphire [52, 53], allowing for design flexibility. Another advantage is the inclusion of a large number of DC electrodes, which enables precise adjustment of trapped ions to desired locations, enhancing scalability [54–57]. However, it must be noted that surface-electrode ion traps have smaller distances between the trapped ions and the nearest electrode compared to macroscopic linear traps [58, 59]. Consequently, the trapped ions in surface-electrode ion traps may be affected by surface problems, including electric field noises [60, 61] and electrostatic charges caused by lasers [62].

The first reported microfabricated ion trap was developed by D. Stick *et al.* using a GaAs substrate and MEMS fabrication technologies, as shown in Figure 1-5 [49]. The trap was designed in a 3D shape with alternating layers of AlGaAs and GaAs grown on the GaAs substrate using molecular beam epitaxy. However, the asymmetric configuration of the electrodes led to low radial confinement, resulting in the loss of trapped ions. In the same year, a surface-electrode ion trap with a 2D structure was developed, as shown in Figure 1-6 [63, 64]. This design was found to be more suitable for microfabrication or MEMS fabrication technologies, offering high precision and reproducibility. However, issues regarding breakdown due to the narrow spacing between electrodes placed on the same plane have arisen [65].

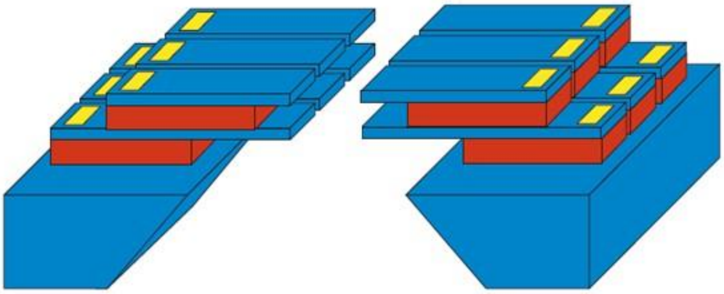

Figure 1-5. A schematic of the first Microfabricated ion trap developed by D. Stick *et al.* [49].

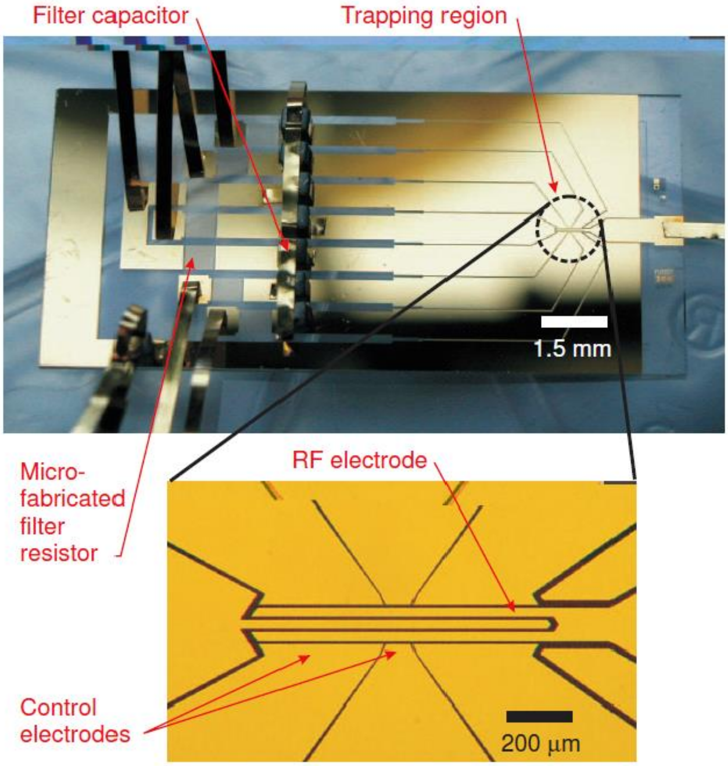

Figure 1-6. A picture of a 2D surface-electrode ion trap developed by S. Seidelin *et al.* [63].

To mitigate the risk of breakdown, researchers proposed a structure that could increase the breakdown voltage by implementing the inner DC electrodes on a plane lower than the RF electrode, which would increase the distance between DC and RF electrodes. Furthermore, an oxide-nitride-oxide (ONO) layer, which alternately stacks silicon dioxide (SiO_2) and silicon nitride (Si_3N_4), has been applied to enhance the breakdown voltage [66]. To prevent the dielectric pillar under the top electrode from being exposed to trapped ions [67], an overhang structure of the electrode was developed, and a method of coating the sidewall of the dielectric pillar with metal was also developed [68]. Since electric charges can accumulate in the silicon layer on the side of the loading slot and affect the trapped ions, a sloped loading slot structure was developed [69].

An example of a fabrication method for a surface-electrode ion trap utilizing the overhang structure, metal coating on the sidewall of the dielectric pillar, and sloped loading slot structure is shown in Figure 1-7. The overhang structure is implemented by using the process of the sacrificial layer (red material in (g) below), and the metal coating on the sidewall of the dielectric pillar ((f) in Figure 1-7) is achieved using the step coverage feature of metal sputtering. The sloped loading slot is constructed using the anisotropic wet etching characteristics of silicon and the Bosch process ((a) and (j) in the figure below). Additionally, if the material of the top electrode can be naturally oxidized, it is typically coated with gold to prevent the formation of the native oxide film on the electrode.

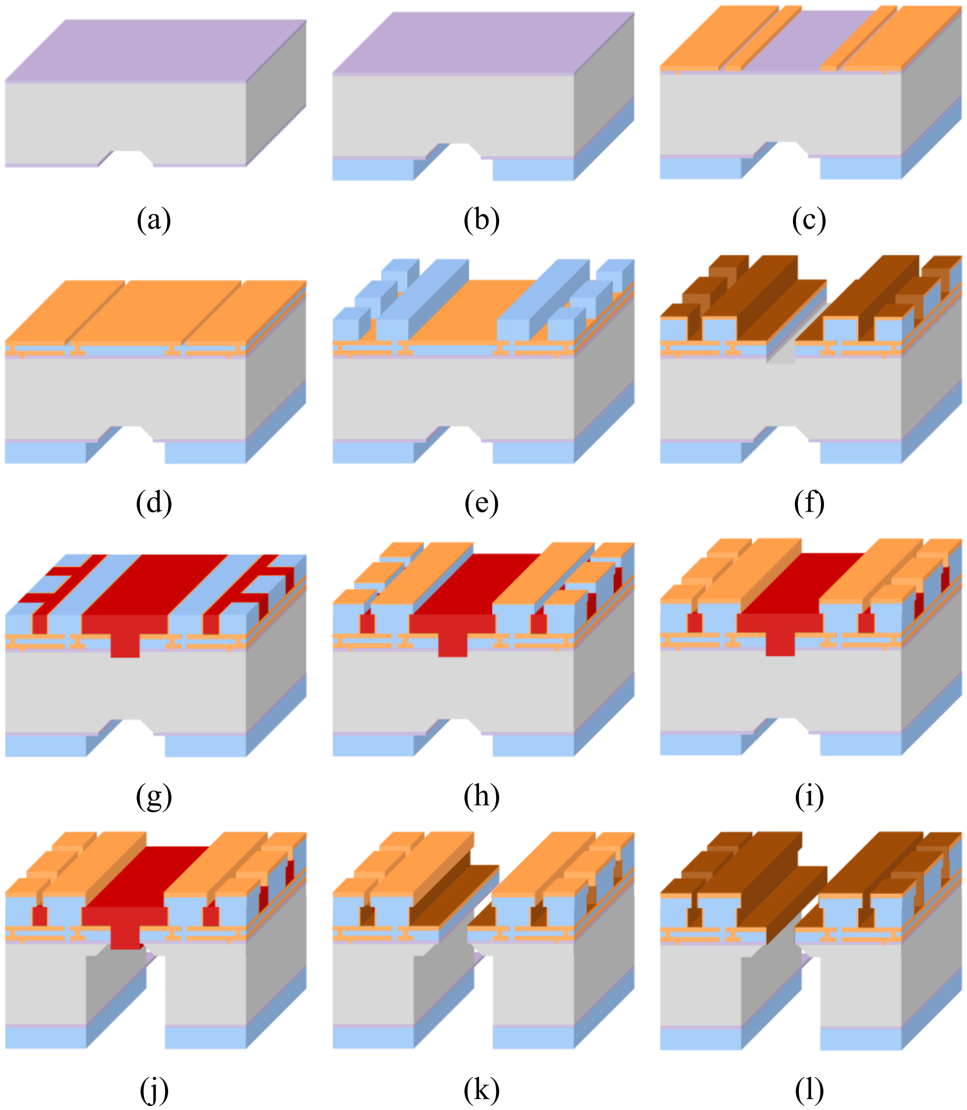

Figure 1-7. A fabrication flow chart of a surface-electrode ion trap developed by C. Jung *et al.* [69, 70]. The gray, purple, blue, orange, brown, and red regions indicate the silicon substrate, Si_3N_4, SiO_2, aluminum-copper alloy (1 wt%), gold, and polyimide, respectively.

The surface-electrode ion trap is commonly regarded as a quantum charge-coupled device (QCCD) architecture [71, 72]. The QCCD is a strategy for operating a large number of ion qubits with one surface trap and involves dividing the surface trap into different regions, such as a gate zone, load zone, and auxiliary zone, as shown in Figure 1-8. Ion shuttling techniques have been investigated to move the ions smoothly to the desired region, while swapping techniques have been developed to change the location of ions. This architecture was initially proposed by D. Kielpinski *et al.* in 2002 [37] and is currently being researched by Quantinuum (previously Honeywell) [72].

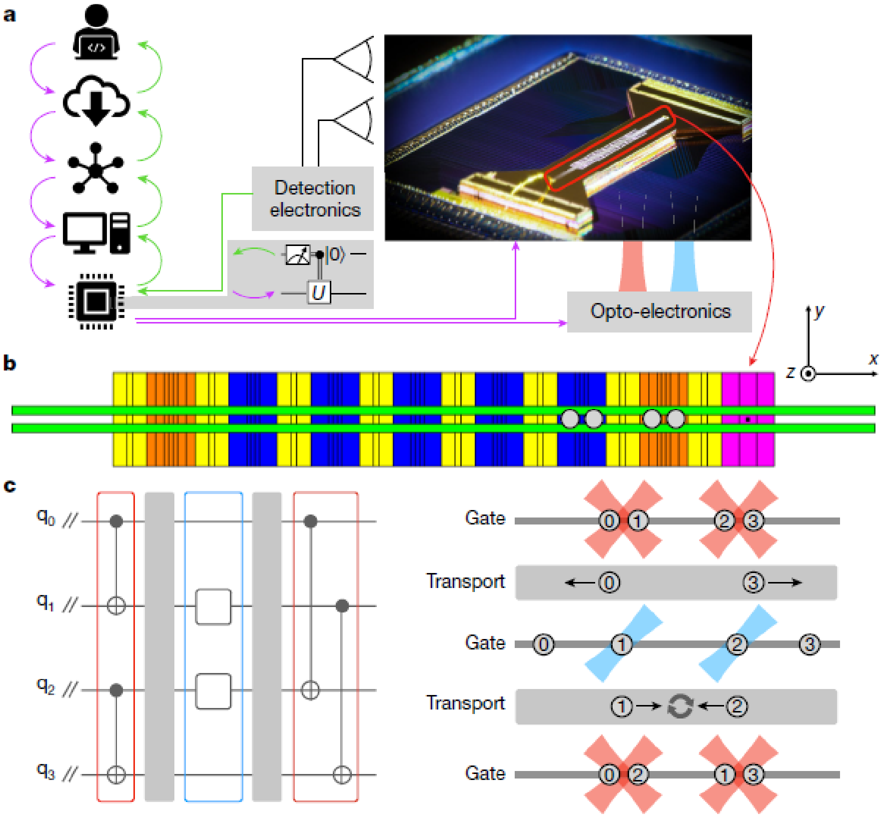

Figure 1-8. A schematic of QCCD proposed by J. M. Pino *et al.* [72].

The modular universal scalable ion-trap quantum computer (MUSIQC) is an alternative approach for operating a large number of ion qubits, which uses multiple ion traps that can be operated independently [73–75]. As shown in Figure 1-9, each ion trap in the MUSIQC is a small computation module called an elementary logic unit (ELU). The information between the ELUs is exchanged through an optical switch. In the MUSIQC architecture, the surface-electrode ion trap is used as ELUs, and IonQ is one of the companies primarily researching this approach.

Modular quantum computers can also be implemented using multiple ion trap arrays [44]. By matching the heights of different surface traps, ions can be physically moved between the traps to transmit quantum information. Although this approach is still in the conceptual stage, it is expected to be developed further in the future.

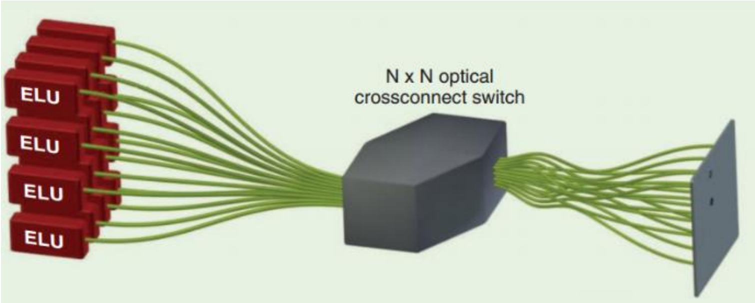

Figure 1-9. A schematic of MUSIQC using an optical cross-connect switch and ELUs. In the ELU, photons are entangled with trapped ions, and the quantum information encoded in the photons is exchanged in the optical switch.

Recent years have seen an increase in research on miniaturizing ion trap systems by integrating optical components or electrical elements into the surface trap [76]. In QIP with ion qubits, it is crucial to detect the light emitted from the trapped ions, and therefore optical access to individual ions is crucial

[41, 77]. While optical fibers are commonly used to collect the fluorescence from the ions [78–80], they can cause perturbations near the trapped ions [81]. By integrating an optical access hole, the dielectric surface can be prevented from being exposed to the ions, and the optical fiber can be placed near the ions [82–84]. Furthermore, integrating an optical waveguide can facilitate the addressing of multiple ions [85–87]. The use of a Si_3N_4 waveguide and a grating coupler has demonstrated the addressing of individual ions, enabling the delivery of light of various wavelengths to the trapped ions.

The integration of electrical elements, such as trench capacitors and current-carrying wire (CCW), into surface-electrode ion traps has gained attention in recent years. For instance, poly-silicon and thermal oxide were used to implement a trench capacitor of approximately 100 pF [88], while low-pressure chemical vapor deposition Si_3N_4 and silicon substrate were used to fabricate a trench capacitor of 1 nF [39]. Moreover, research has been conducted on integrating magnetic field gradients to operate the Zeeman qubit. A permanent magnet made of SmCo was included under the surface trap, but a manual alignment of the trap and magnet was required [89]. The CCWs have also been integrated to create a static or oscillating magnetic field gradient. The CCWs have been implemented in-plane as a part of electrodes [90, 91], or fabricated under surface traps [92, 93]. Although the latter method has a burden associated with the damascene process, a larger gradient can be obtained by reducing the distance between trapped ions and the wires.

In recent years, the distinction between linear and surface traps has become less clear. Previously, surface traps were typically defined by their use of microfabrication technology, but a macroscopic linear trap has been developed by stacking wafers, as shown in Figure 1-10 [40, 94]. A blade trap was microfabricated using conventional microfabrication technology by inserting a SiO_2 wafer with a thickness of hundreds of micrometers between two silicon wafers, and the electrode was fabricated using microfabrication techniques. This method achieved a microfabricated blade trap with high reproducibility and a high trap depth of 1 eV [40].

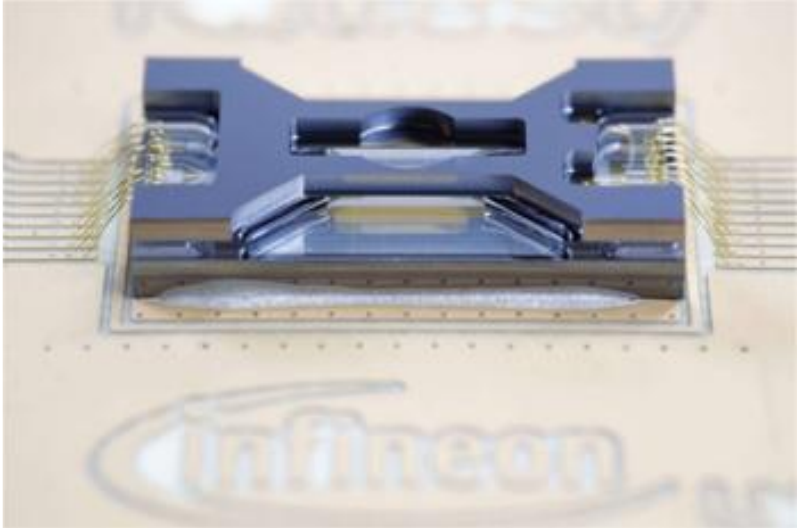

Figure 1-10. A picture of a microfabricated 3D ion trap reported by S. Auchter *et al.* [40].

1-3. Laser-Induced Stray Charge

A laser-induced stray charge can induce stray electric fields at the location of trapped ions [95, 96]. The stray charge is typically generated when photoelectrons emitted from electrode surfaces accumulate in nearby dielectric surfaces or when electrons are ejected from the anti-reflection (AR) coating of the glass substrate [62]. This charging phenomenon can be modeled as a photoelectric effect on a metal surface modified with a thin insulating film [97]. In this model, photoelectrons trapped in the native oxide layer form electron-hole pairs with the image charge in the electrode, which may create an electric field in the form of a dipole [62]. The rate of charging can be described by the following rate equation [97]:

$$\dot{Q} = \alpha - (\delta + \gamma)Q, \tag{1.9}$$

where α is the rate at which new charges are accumulated by an incident laser and depends on the frequency and intensity of the incident laser. The δ is a constant for the rate at which new charges are prevented from accumulating by existing charges, and γ indicates a constant for the rate at which accumulated charges are dissipated. The above model was verified in various surface traps using different laser frequencies, intensities, and electrode materials [62, 97].

The accumulation of laser-induced stray charge is a time-dependent phenomenon [40, 98], which poses a challenge to keep the stability of trapped ions over long periods, even if an additional electric field is applied to compensate for the resulting stray electric field. The charging rate slows down over time, as described by Eq. (1.9). To minimize the impact of stray charges, typical ion-trap experiments are performed under conditions of slow charging rates, achieved by exposing the surface-electrode ion trap to the laser for an extended period. However, this solution is not entirely satisfactory since stray charges can still accumulate over time, even after several months of laser exposure. Therefore, a more permanent solution to the problem of laser-induced stray charges is required.

In most ion trap experiments, high-frequency lasers are used [6, 99], which can result in the emission of photoelectrons from the trap surface. These photoelectrons can accumulate in the surrounding dielectric surfaces, leading to the generation of stray electric fields on the trapped ions. To suppress the generation of stray charges, the laser propagation paths can be adjusted until the measured stray electric field appears to be minimized [100]. However, this process may be inefficient, since the locations of the stray charges are unknown beforehand.

1-4. Dissertation Overview

In this dissertation, a method for estimating the locations of laser-induced stray charges in surface-electrode ion traps is developed [101]. By identifying the locations of stray charges, the following advantages can be achieved.

- Possibility of characterizing laser-induced stray charges when stray electric fields are detected on trapped ions
- Increasing the efficiency of ion-trap experimental design to avoid or suppress the laser-induced stray charges, leading to improved reliability and stability of ion-trap systems

In the subsequent sections, the developed method is theoretically analyzed and experimentally evaluated. In Chapter 2, a theoretical model is presented to verify how the electric potential at the trapped ion location changes in the presence of a laser-induced stray charge, and the magnitude of the shift in the secular frequency of a trapped ion is derived from the model. The location of the stray charge is then estimated from the secular frequency shift by using the inverse relationship between the stray charge and the secular frequency shift, subject to certain constraints to ensure a unique solution. This model is then extended to the case where stray charges are generated at multiple locations, and the number of distinguishable charge locations using this model is analyzed. In Chapter 3, simulations are performed to support the effectiveness of the developed method. Chapter 4 describes the experimental apparatus and the procedure used to experimentally demonstrate the method by irradiating the trap surface with a laser to intentionally produce electric charges at a single location, and the resulting secular frequency shift is measured at multiple ion positions to estimate the location of the produced charges. The estimated location is then compared to where the laser is actually irradiating. Afterward, Chapter 5 provides a comprehensive summary of the entire study and its findings.

Chapter 2

Theoretical model

In this chapter, a theoretical model is presented for estimating the locations of laser-induced stray charges in surface-electrode ion traps using the secular frequency of a trapped ion. In Section 2-1, the change in the secular frequency of the trapped ion is modeled in the presence of a laser-induced stray charge, and the principle of estimating the locations of the stray charge using the relationship between the secular frequency shift and the stray charge is described. In Section 2-2, constraints are considered to uniquely determine the locations of stray charges in the process of estimating their locations using the secular frequency shift of the trapped ion. The laser-induced stray charges can occur at multiple locations, and therefore the developed method is extended to estimate their multiple locations in Section 2-3.

2-1. Model for Single Stray Charge Location

The following discussion assumes a Paul trap, which confines charged particles in space using an oscillating electric field and an electrostatic field. Figure 2-1 shows a schematic of a surface-electrode ion trap with Cartesian coordinates. The surface trap typically has RF electrodes and inner/outer DC electrodes in a plane, and to measure the secular frequency at multiple ion positions (z_{ion}), the proposed method assumes that the trapped ion can move along the longitudinal direction of the RF electrode (z-axis in Figure 2-1).

When the trap center is positioned at $(0,0,z_{ion})$, the electric potential experienced by the trapped ion consists of a time-dependent part that varies sinusoidally at the RF drive frequency ω_{rf} and a time-independent electrostatic part as follows [102]:

$$\Phi_0(x,y,z,t) = \frac{1}{2}U_0(ax^2 + by^2 + c(z - z_{ion})^2) + \frac{1}{2}V_0\cos(\omega_{rf}t)(a'x^2 + b'y^2 + c'(z - z_{ion})^2), \qquad (2.1)$$

where U_0 and V_0 are the electrostatic potential and the drive RF voltage, respectively. For a linear trap, $c' = 0$ is assumed to be similar to Ref. [102]. The equation of motion of a single trapped ion oscillating along the z-direction at Φ_0 can be then written as

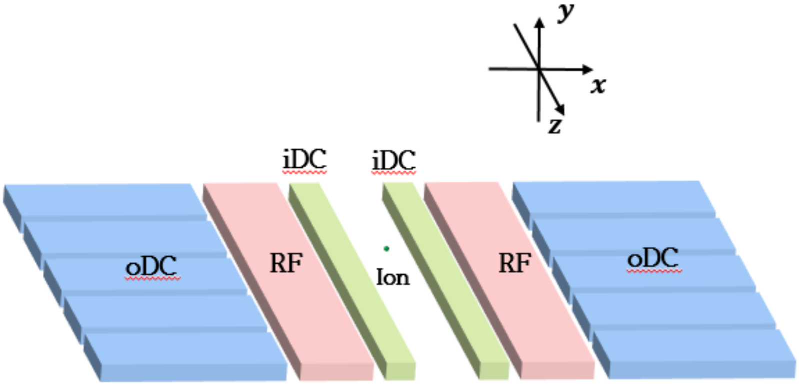

Figure 2-1. A schematic of a surface-electrode ion trap with Cartesian coordinates. A green dot, RF, oDC, and iDC indicate a single trapped ion, RF electrodes, segmented outer DC electrodes, and inner DC electrodes, respectively.

$$\ddot{z} = -\frac{1}{m} \times \frac{\partial}{\partial z}(Z|e|\Phi_0) = -\frac{Z|e|}{m} U_0 c(z - z_{ion}), \tag{2.2}$$

where $Z|e|$ and m are the electric charge and the mass of the trapped ion, respectively. The Eq. (2.2) describes the harmonic oscillation of a particle along the z-axis and the corresponding secular frequency ($\omega_{z0}(z_{ion})$) can be written as

$$\omega_{z0}(z_{ion}) = \sqrt{\frac{Z|e|}{m} \times \frac{\partial^2 \Phi_0}{\partial z^2}}\Bigg|_{z=z_{ion}} . \tag{2.3}$$

Let Φ_q be the potential generated by a laser-induced stray charge (Q)

when the stray charge is generated in the vicinity of the trapped ion. Then, the resulting secular frequency (ω_z) can be written as

$$\omega_z(z_{ion}) = \sqrt{\frac{Z|e|}{m}\left(\frac{\partial^2 \Phi_0}{\partial z^2} + \frac{\partial^2 \Phi_q}{\partial z^2}\right)}\Bigg|_{z=z_{ion}}. \tag{2.4}$$

In typical cases where $\frac{\partial^2 \Phi_q}{\partial z^2} \ll \frac{\partial^2 \Phi_0}{\partial z^2}$, Eq. (2.4) can be rewritten using Taylor expansion as

$$\omega_z(z_{ion}) \cong \omega_{z0}(z)\left[1 + \frac{\partial^2 \Phi_q}{2\partial z^2}\left(\frac{\partial^2 \Phi_0}{\partial z^2}\right)^{-1}\right]\Bigg|_{z=z_{ion}}. \tag{2.5}$$

Since the secular frequency shift in the z-axis ($\Delta\omega_z$) is $\omega_z - \omega_{z0}$, $\Delta\omega_z$ can be written as

$$\Delta\omega_z(z_{ion}) \cong \frac{Z|e|}{2m\omega_{z0}(z_{ion})} \times \frac{\partial^2 \Phi_q}{\partial z^2}\Bigg|_{z=z_{ion}}. \tag{2.6}$$

Let the charge Q be a point charge induced at (x_q, y_q, z_q) [62]. Also, let x_{ion}, y_{ion}, and z_{ion} be the coordinates of the trapped ion, respectively. The $\Delta\omega_z$ can be then written as

$$\Delta\omega_z(x_{ion}, y_{ion}, z_{ion}) \cong \frac{KQ(x_d^2 + y_d^2 - 2z_d^2)}{\omega_{z0}(z_{ion})(x_d^2 + y_d^2 + z_d^2)^{\frac{5}{2}}}, \tag{2.7}$$

where $K = -Z|e|/(8\pi\varepsilon_0 m)$, and x_d, y_d, and z_d indicate $(x_{ion} - x_q)$, $(y_{ion} - y_q)$, and $(z_{ion} - z_q)$, respectively. According to Eq. (2.7), when $z_d^2 < \frac{1}{2}(x_d^2 + y_d^2)$, the sign of $\Delta\omega_z$ is determined by the sign of Q.

Conversely, when $z_d^2 \gg \frac{1}{2}(x_d^2 + y_d^2)$, $\Delta\omega_z$ converges to zero. The resulting equation is obtained by taking the derivative of Eq. (2.7) with respect to z_{ion}, which is expressed as follows:

$$\frac{\partial}{\partial z_{ion}}(\Delta\omega_z) \cong -\frac{3Kz_d\left[3x_d^2 + 3y_d^2 - 2z_d^2\right]}{\omega_{z0}(z_{ion})[x_d^2 + y_d^2 + z_d^2]^{\frac{7}{2}}}. \tag{2.8}$$

According to Eq. (2.8), $\frac{\partial}{\partial z_{ion}}(\Delta\omega_z)$ approaches zero near $z_{ion} = z_q$. In other words, when z_q is fixed, z_q can be inferred from z_{ion} where a $\Delta\omega_z$ peak is observed. Also, the full width at half maximum (FWHM) of $\Delta\omega_z$ peak can be approximated as

$$\mathrm{FWHM} \cong 0.77\sqrt{x_q^2 + y_q^2}. \tag{2.9}$$

Thus, x_q and y_q can be inferred from the FWHM of $\Delta\omega_z$ peak. According to Eq. (2.7), Q is a proportional constant of $\Delta\omega_z$ peak, and therefore the amount of Q can be estimated from the magnitude of $\Delta\omega_z$ peak. In other words, in principle, the single stray charge location (x_q, y_q, z_q) can be estimated by fitting Eq. (2.7) to the measured $\Delta\omega_z(z_{ion})$.

2-2. Assumption

To ensure the unique determination of the location of stray charges from $\Delta\omega_z(z_{ion})$ measured at multiple ion positions $(0,0,z_{ion})$, constraints are considered. Various combinations of stray charge locations and other causes can lead to similar distributions of $\Delta\omega_z(z_{ion})$. It is assumed that the secular frequency is changed only by laser-induced stray charges, and other factors are negligible [61]. Furthermore, only stray charges close to the ion position are considered to change the secular frequency of the trapped ion, while the effect of other distant stray charges is negligible. This assumption can also be inferred from Eq. (2.7), which shows that the frequency shift due to stray charges far from the ion position approaches zero. The location of laser-induced stray charge is assumed to remain fixed over time. For stray charges on the trap surface, $|y_{ion} - y_q|$ is set to be equal to the ion height. In addition, Φ_0 is assumed to have the same curvature ($\partial^2\Phi_0/\partial z^2 = c$) independent of z_{ion}, and therefore $\omega_{z0}(z_{ion})$ is set to be uniform. The free parameters used during the curve fitting are x_q, z_q, and Q.

2-3. Model for Multiple Stray Charge Locations

In this section, the above model is extended to the case where the stray charges occur at multiple locations in the vicinity of the trapped ion. In this case, the electric potential generated by multiple Q_m is equal to the sum of $\Phi_{q,m}$ by each Q_m. When $\partial^2\Phi_{q,m}/\partial z^2 \ll \partial^2\Phi_0/\partial z^2$, $\Delta\omega_z$ can be approximated as

$$\Delta\omega_z(x_{ion}, y_{ion}, z_{ion}) \cong \frac{K}{\omega_{z0}(z_{ion})}\sum_{m=1}^{n}\frac{Q_m\left(x_{d,m}^2 + y_{d,m}^2 - 2z_{d,m}^2\right)}{\left(x_{d,m}^2 + y_{d,m}^2 + z_{d,m}^2\right)^{5/2}}, \qquad (2.10)$$

where Q_m indicates m-th stray charge induced at $\left(x_{q,m}, y_{q,m}, z_{q,m}\right)$, and $x_{d,m}$, $y_{d,m}$, and $z_{d,m}$ are $\left(x_{ion} - x_{q,m}\right)$, $\left(y_{ion} - y_{q,m}\right)$, and $\left(z_{ion} - z_{q,m}\right)$, respectively. When different stray charges are sufficiently far apart, the number of observed peaks in the plot of $\Delta\omega_z(z_{ion})$ can be equal to the number of charge locations, as depicted in Figure 2-2(a). In this case, the locations of different charges can be easily estimated from each peak in the $\Delta\omega_z(z_{ion})$ plot. However, when different charges are close together, only a single $\Delta\omega_z(z_{ion})$ peak can be observed, as shown in Figure 2-2(b). In this case, it is challenging to distinguish the locations of different charges. However, the proposed method can still work up to some degree. Thus, to figure out the number of stray charge locations that can be distinguished using the developed method when there is only a single dominant peak in the $\Delta\omega_z(z_{ion})$ plot, I try to fit the curve of Eq. (2.10) to numerous test data generated with the assumption of multiple stray charges at random locations. Note that all curve-fitting processes are performed using the SciPy library [103]. The curve-fitting algorithm is based on the least squares method, which is aimed at approximating the locations of stray charges. The estimated Q_m, $x_{q,m}$, and $z_{q,m}$ in the curve-fitting processes are then compared with the actual Q_m, $x_{q,m}$, and $z_{q,m}$ used for the generation of test data. To quantitatively analyze the effectiveness of the curve fitting for the numerous test data, the errors between the estimated values and the actual values are defined as the maximum value among the fractional errors of fitted parameters, such as Q_1, $x_{q,1}$, $z_{q,1}$, …, Q_n, $x_{q,n}$, $z_{q,n}$. Depending on the number of charge locations from 1 to 5, the average error rates are 0.0, 0.3±0.7, 3.3±4.4, 13.4±12.9, and 24.2±13.5 %, respectively, as illustrated in Figure 2-3. Note that the minimum distance between different charges is 10 μm in the test data. The increase in error rates with the number of stray charge locations is due to the increase in the number of free parameters, i.e., when the number of stray charge locations is 4, the number of free parameters to be determined is 12. Furthermore, the curve-fitting process often fails when the number of charge locations is 4 or more. Even if the curve fitting is successful, the reliability of the results is low, since both the average error rate and the margin of error are large when the number of charge locations is 4 or more. Thus, when there is a single dominant $\Delta\omega_z$ peak, it is concluded that up to three stray charge locations can be identified as long as different charges are separated by more than 10 μm, smaller than the typical size of beam waist used in ion traps, and the locations of four or more stray charges may be difficult to distinguish.

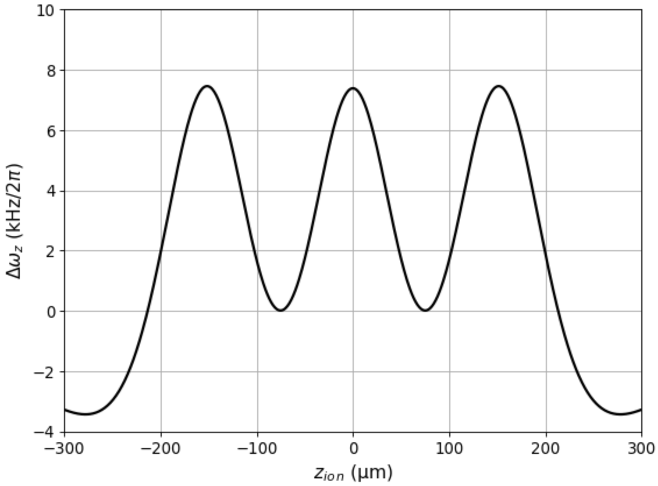

(a)

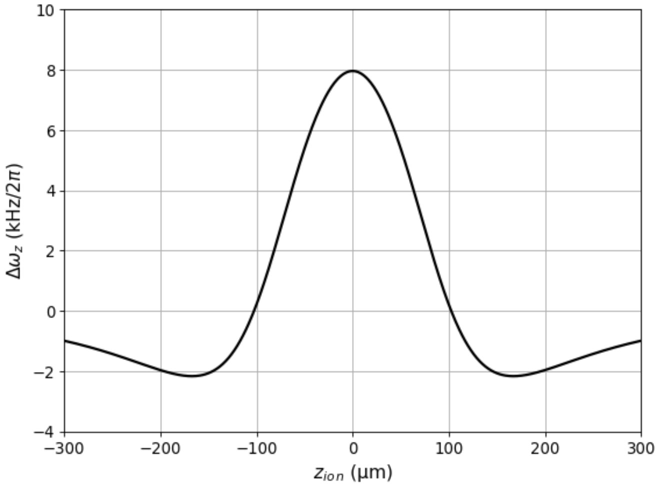

(b)

Figure 2-2. Calculation results of $\Delta\omega_z(z_{ion})$ when charges occur at three separate locations. (a) A calculation result of three $\Delta\omega_z$ peaks by three stray charges that are sufficiently far apart. (b) A calculation result of a single $\Delta\omega_z$ peak due to three stray charges close enough for each peak to overlap.

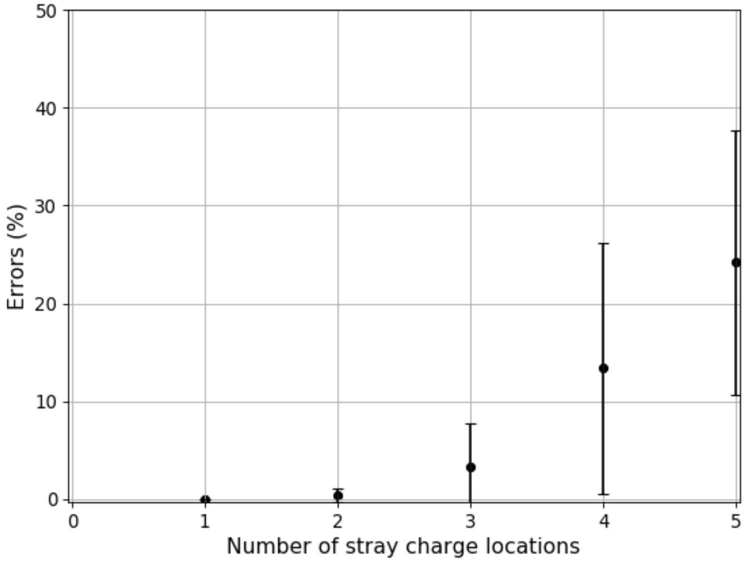

Figure 2-3. Errors between actual and estimated values for the number of stray charge locations. When the number of stray charge locations ranges from 1 to 5, the estimated average errors are 0.0, 0.3±0.7, 3.3±4.4, 13.3±12.9, and 24.5±13.5 %, respectively. Error bars indicate standard deviations.

In typical cases, the curve-fitting process must be performed without knowing the number of charge locations. Thus, during the curve-fitting process, I vary the number of free parameters necessary for multiple charge locations. When the number of free parameters is larger than the necessary free parameters, $Q_m = 0$ for some parameters is obtained, or the total charge at a single location is divided into two charges located at the same position. Conversely, when the number of free parameters is less than the minimum number to describe the actual situation, incorrect $x_{q,m}$ and $z_{q,m}$ are obtained. In this case, as the number of free parameters increases, completely different fitting results are obtained until the minimum number of free parameters is reached. Consistent results are then obtained once a sufficient number of free parameters are used. For instance, Figure 2-4 shows the simulation results of $\Delta\omega_z$ due to two different stray charges and the curve-fitting results for the input number of stray charge locations. Of the results, Figure 2-4(a) shows the curve-fitting result when the input number of stray charge locations is 1. The curve-fitted graph has a slight difference from the simulated graph. The estimated x_q , z_q , and the amount of Q are inconsistent with the input value. On the other hand, Figure 2-4(b) shows the curve-fitting results when the input number of stray charge locations is 3, and the graph that matches the simulated graph is obtained. Also, the obtained x_q and z_q are consistent with the input values. Regarding the amounts of charges, one of the two input charges is fully obtained, and the other is divided into two parts.

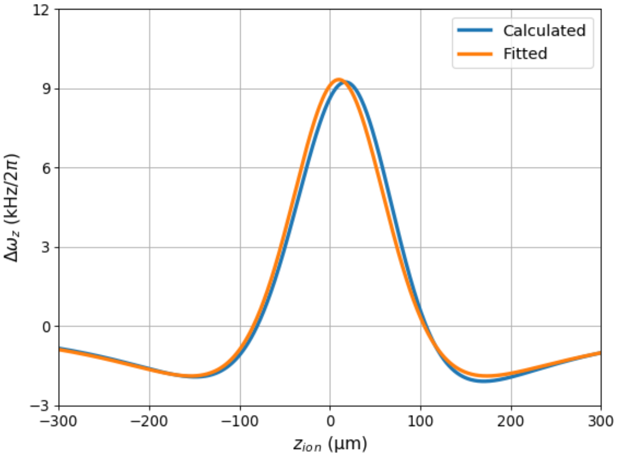

(a)

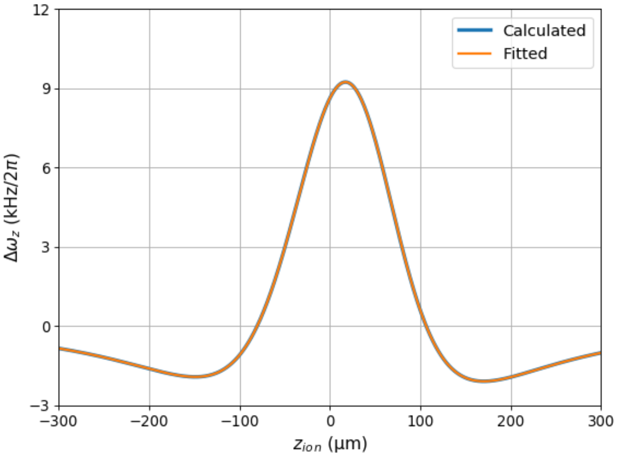

(b)

Figure 2-4. Simulation results of $\Delta\omega_z$ caused by two different stray charges and curve-fitting results of the different number of charge locations. (a) The simulation result and the curve-fitting result when the number of charge locations is 1. (b) The simulation result and the curve-fitting result when the number of charge locations is 3.

Chapter 3

Simulation

In this chapter, the theoretical model presented in Chapter 2 is validated by comparing it with computer simulation results through curve fitting. Before the comparison, the electric potential at the ion position is simulated, and the initial secular frequency (ω_{z0}) is calculated in Section 3-1. In Section 3-2, various scenarios, where stray charges occur, are simulated by introducing a point charge in the simulation. The resulting $\Delta\omega_z$ at multiple ion positions is then calculated and compared with the curve fitting results of Eq. (2.10) in Section 3-3.

3-1. Simulation of Trapping Potential

The trapping potential refers to the total potential at the location of trapped ions, and it can be simulated using the boundary element method (BEM) or the finite element method (FEM). The BEM approach solves linear partial differential equations using boundary conditions, and the charged particle optics (CPO) software is an example of a BEM tool. On the other hand, the FEM approach subdivides a large space into simpler parts to solve partial differential equations. The COMSOL Multiphysics software is a commonly used FEM tool. Although both CPO and COMSOL can be used to simulate the trapping potential, all the results presented in this chapter are obtained from COMSOL, as it yields comparable results within a 5% error.

The simulation of the trapping potential requires the analysis of the pseudopotential by an RF voltage and electrostatic potential by DC voltages. The first step is to create the layout of the ion trap to be simulated, and then simulate the electric field and potential at the trap center when 1 V is applied to each electrode. Note that the grounding of the electrodes may affect the simulation results. In the simulation presented below, all electrodes other than the one applying 1V are grounded, and the surrounding regions are also grounded.

In a linear trap, the pseudopotential at the trap center due to the RF voltages is given by the following equation:

$$\Psi_p = \frac{e^2 E^2}{4 m_{ion} \omega_{rf}^2}, \tag{3.1}$$

where e is the elementary charge and m_{ion} is the mass of the ion. In typical linear traps, the trapping position is the null point at the pseudopotential. Thus, as shown in Figure 3-1, the ion height can be approximately 108 μm from the simulated RF null point. In the case of our ion trap, the ion height cannot be changed since only a pair of RF electrodes are placed. However, the ion height can be adjusted by employing two pairs of RF electrodes.

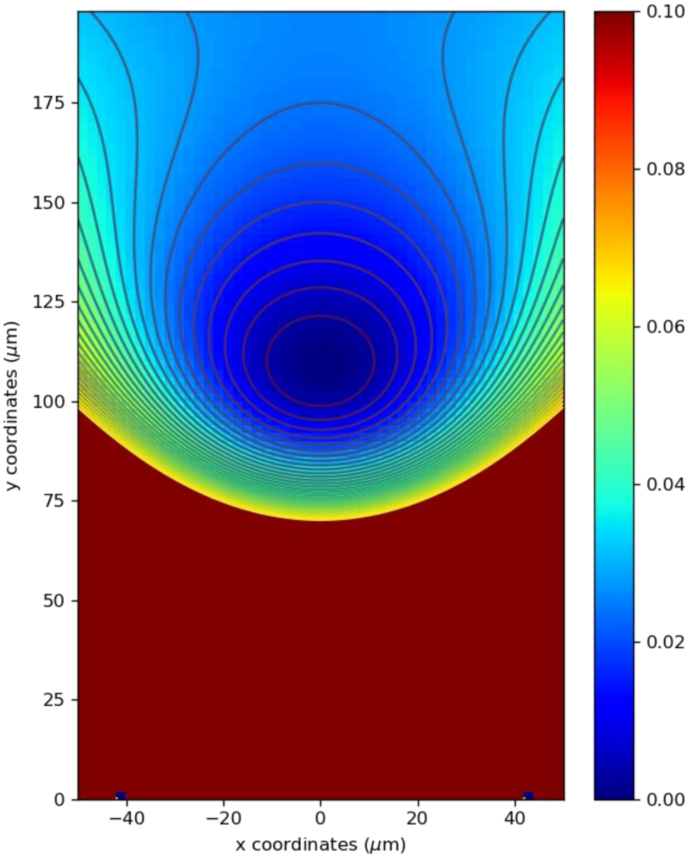

Figure 3-1. Simulation result of the RF pseudopotential. The deep blue region indicates the trap center.

A simulation of the total potential is performed by using a pair of inner DC electrodes and six pairs of outer DC electrodes. The first purpose of the DC voltages derived from the DC potential is to make the sum of the electric field at the ion location zero so that the micromotion does not occur. For example, consider the five-wire geometry shown in Figure 3-2. The outer-corner four DC electrodes are grouped (LT, LB, RT, and RB), the outer-center two electrodes are grouped (LC, RC), and the two inner electrodes are grouped (LI, RI). The voltages of each group are decomposed into symmetrical and asymmetrical components. In this case, components V_{SO}, V_{SC}, and V_{SI} can move the ions in the y-direction, and V_{AO}, V_{AC}, and V_{AI} may move the ions along the x-axis. The DC voltages applied to the segmented electrodes can displace the ions along the z-direction. Let E be the strength of the electric field applied by each component to the trap center. To minimize the micromotion of trapped ions, the electrostatic field component generated by the outer-corner electrode must be canceled with that by the inner electrodes. In other words, the following equations must be satisfied to remove the micromotion:

$$V_{SO}E_{ySO} + V_{SC}E_{ySC} + V_{SI}E_{ySI} = 0, \tag{3.2}$$

and

$$V_{AO}E_{xAO} + V_{AC}E_{xAC} + V_{AI}E_{xAI} = 0. \tag{3.3}$$

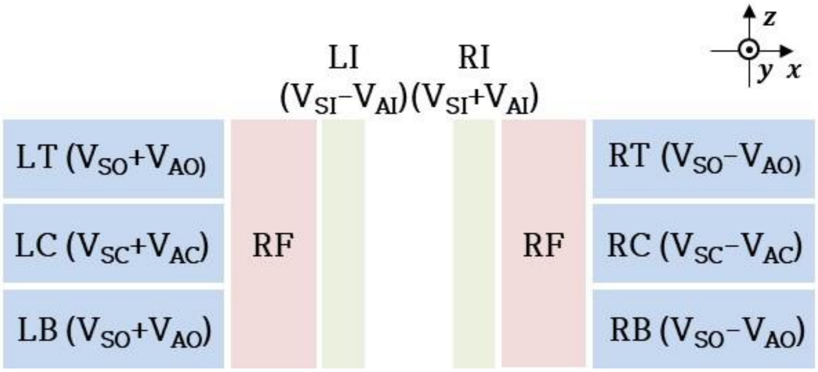

Figure 3-2. Simplified layout of electrodes in the vicinity of the trap center. The LT, LC, LB, LI, RI, RT, RC, and RB represent DC electrodes.

Another requirement for determining the DC voltage set is to rotate the ion's principal axis by approximately 45 degrees so that laser cooling can be carried out along all axes with a single laser in one direction. This requires the intentional application of V_{AO} and V_{AC}, while ensuring that the net electric field at the ion location is zero to avoid inducing micromotion. The resulting potential at the trap center in the $x-y$ plane is illustrated in Figure 3-3, where θ indicates the rotating angle, and x' and y' are the rotated principal axes. The trapped ion oscillates along the x' and y' directions, and therefore the secular frequencies in the radial directions are estimated in those directions. The Hessian matrix is used to calculate the electric field curvature, and the secular frequency in the z-axis is estimated with the same procedure.

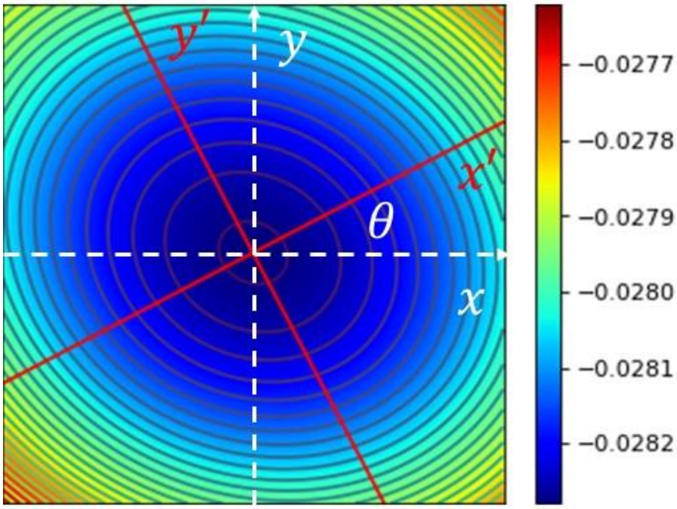

Figure 3-3. The simulation result of total potential in the radial plane. The θ indicates the rotating angle, and x' and y' are the rotated principal axes.

3-2. Simulation of Laser-Induced Stray Charge

To simulate the effects of stray charges in the COMSOL Multiphysics, a point charge is added, as shown in Figure 3-4. The location of the point is assumed to be $(55, -108, 0)$ μm, which corresponds to the position on an inner DC electrode of our surface-electrode ion trap. The electric potential at the trap center due to the point charge is then calculated.

The simulation assumes a displacement of the ion position by 40 μm, which corresponds to half the distance between the segmented DC electrodes of the ion trap used in the experiments, approximately 80 μm. To simply simulate the change in ion position, the point charge moves in increments of 40 μm instead of the trap center. This simulation is performed over a range from −240 to +240 μm.

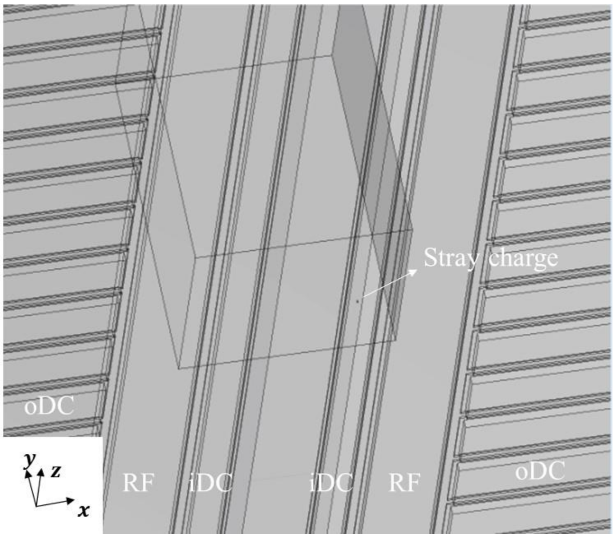

Figure 3-4. The layout of the surface-electrode ion trap and the point charge. The oDC and iDC indicate segmented outer DC and inner DC electrodes.

Figure 3-5 depicts the addition of the electric potential caused by the point charge to the secular frequency calculation code to simulate the impact of stray charges on the secular frequency. The potential at the trap center is obtained from this addition, and ω_z is estimated. The difference between the calculated ω_z and ω_{z0} yields $\Delta\omega_z$, which represents the secular frequency shift caused by the stray charge.

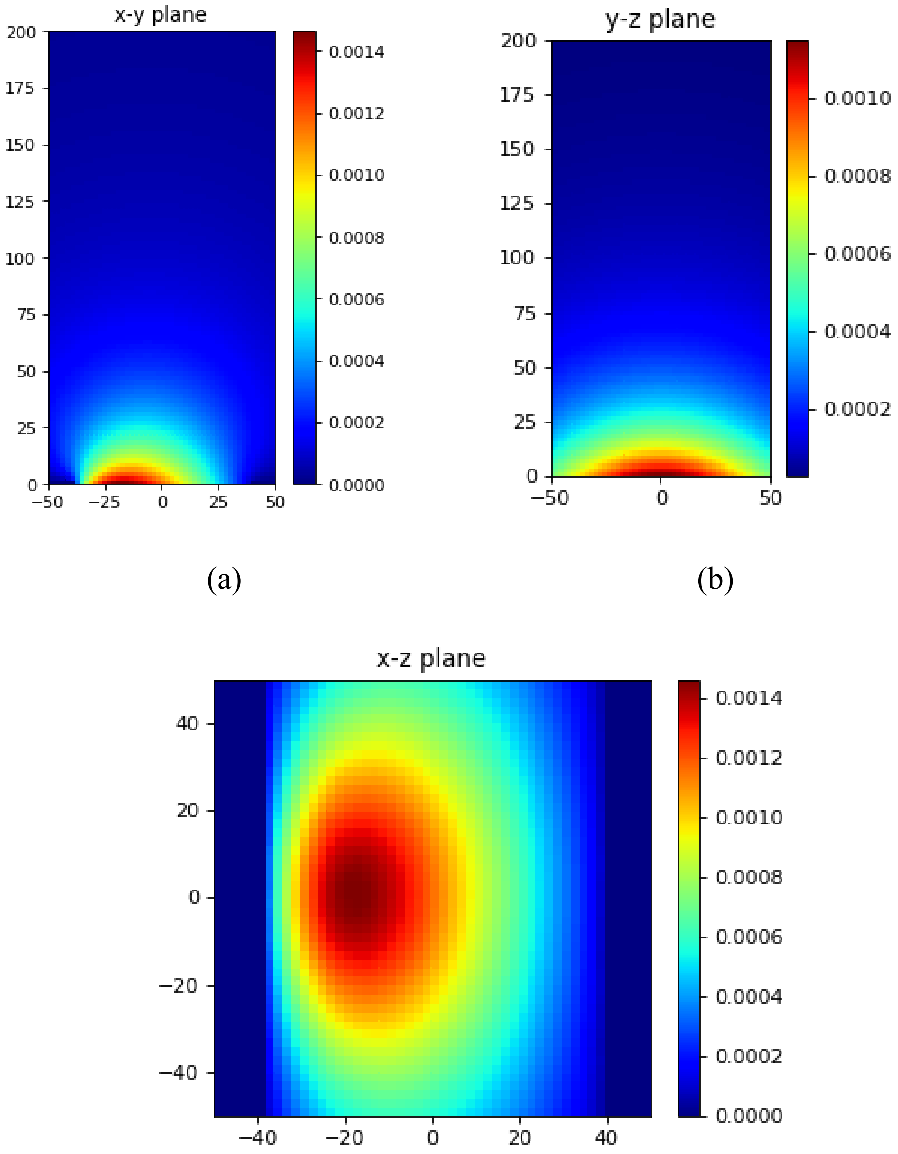

(a) (b)

(c)

Figure 3-5. Simulation results of the electric potential change at the trap center. All results show two-dimensional potentials, and (a), (b), and (c) illustrate the simulated potential in $x-y$, $y-z$, and $z-x$ planes, respectively.

3-3. Simulation Results

To support the effectiveness of the developed method, the curve-fitting results of Eq. (2.10) were compared with the simulation results. First, the simulation results of $\Delta\omega_z(z_{ion})$ by a single point charge was shown as the blue dots in Figure 3-6. The amount of the input charge was set to $-1000e$, and the charge was positioned at $(55, -108, 0)$ μm. As a result of curve fitting, a single peak was observed at $z_{ion} = 0$. The fitting results to the simulated $\Delta\omega_z$ is illustrated as the orange line in Figure 3-6. The estimated x_q and z_q were 63 and 0 μm, respectively, and Q was obtained as $-653e$. Even if n in Eq. (2.10) was increased up to 3, the fitting results of x_q and z_q were the same. Thus, the number of charge locations was inferred to be 1.

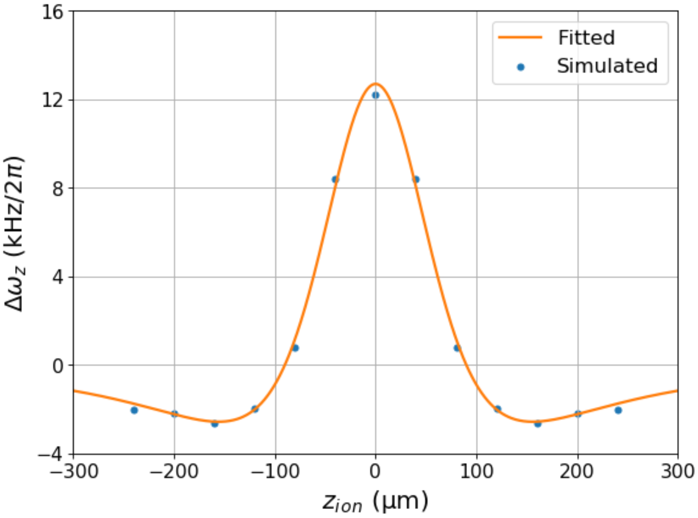

Figure 3-6. Curve fitting and simulation results of $\Delta\omega_z$ as a function of z_{ion}. The orange line and the blue dots indicate the curve-fitting result and simulation result, respectively.

Although the curve-fitting result and simulation result was comparable, a discrepancy existed. This discrepancy can be attributed to errors resulting from the use of a first-order approximation in the theoretical model or from inaccuracies in the simulation itself. Also, the neglect of ion position change, which can be taken into account in the simulation but not in the model, may contribute to the discrepancy.

Figure 3-7(a) shows the simulation result when the two charges are far apart (approximately 160 μm), and both charges were assumed to have an amount of $-1000e$. In this case, one of the charges was assumed to be located at −80 μm, and the other was set to be located at 80 μm along the z-axis while the $x_{q,m}$ and $y_{q,m}$ are 55 μm and −108 μm, respectively. When n was set to 1 during a curve fitting to Eq. (2.10), only a single peak at $z_{ion} = 0$ was observed. However, when n in Eq. (2.10) is 2 or more, two $\Delta\omega_z$ peaks located at two different positions were observed, as illustrated in the orange line in Figure 3-7(a). The estimated $z_{q,1}$ and $z_{q,2}$ were ± 80 μm, and both $x_{q,1}$ and $x_{q,2}$ were estimated to be 61 μm. Additionally, the estimated charge amount of both charges was $-643e$. Thus, the number of charge locations could be inferred to be 2. The results agreed with the actual values regarding the coordinates and the number of charge locations.

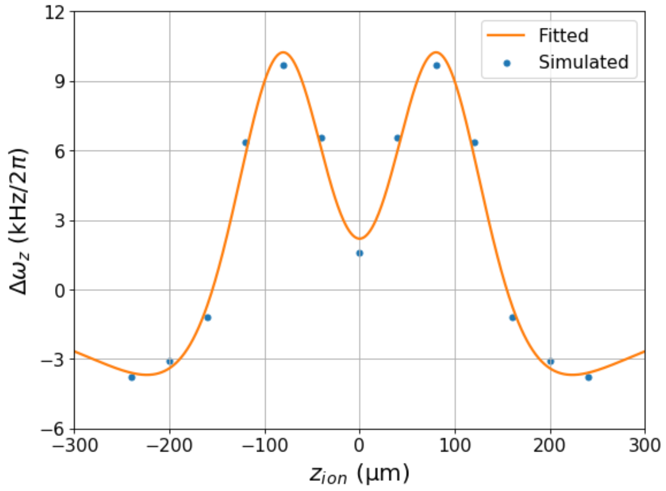

(a)

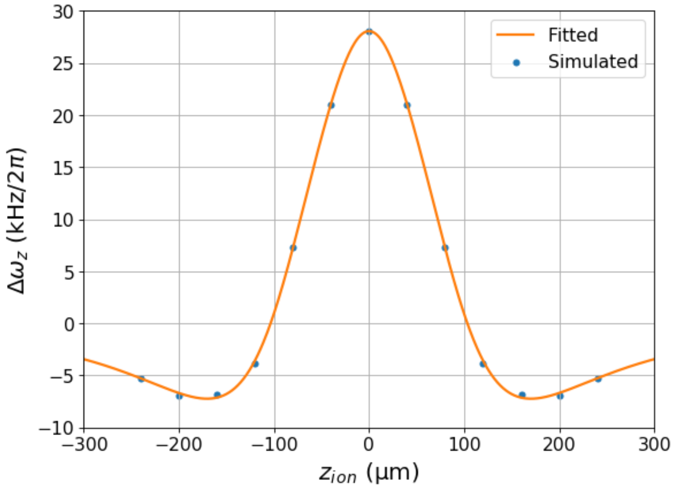

(b)

Figure 3-7. Curve fitting and simulation results of $\Delta\omega_z$ caused by multiple stray charges. (a) The simulation result of $\Delta\omega_z$ when two stray charges are far apart (approximately 160 μm). (b) The simulation result of $\Delta\omega_z$ when three stray charges are close together (approximately 40 μm).

The simulation result for the case where three charges are close together is shown in Figure 3-7(b). The $z_{q,1}$, $z_{q,2}$, and $z_{q,3}$ were −40, 0, and 40 μm, respectively, and the $x_{q,m}$ and $y_{q,m}$ were 55 μm and −108 μm, respectively. Also, all the charges were assumed to have an amount of $-1000e$. In this case, only a single peak was observed in the $\Delta\omega_z$ plot, as shown in the blue dots in Figure 3-7(b). When n was 1 in Eq. (2.10), a plot similar to the shape of blue dots was drawn, and the z coordinate of the peak was zero. Also, when n was 2 in Eq. (2.10), a graph similar to the distribution of blue dots was observed, and the estimated $z_{q,1}$ and $z_{q,2}$ were ± 33 μm. However, when n was 3 or more, three different z coordinates (± 42 μm and 0 μm) were obtained while still observing a single peak, as illustrated in the orange line in Figure 3-7(b). The estimated values for $x_{q,1}$, $x_{q,2}$, and $x_{q,3}$ were the same, at 51 μm, with estimated charge amounts of $-550e$ for the charge at $z_{ion} = 0$ and −564e for the charges at $z_{ion} = \pm 42$ μm. From these observations, it could be concluded that there were three distinct charge locations, consistent with the coordinates of actual charge locations.

Chapter 4

Experiment

This chapter presents experiments conducted to validate the efficacy of the developed method. The experimental setup is described in Section 4-1. First, a surface-electrode ion trap is designed and fabricated. Then, laser modules are prepared to trap ionized atoms, while electronics are employed to generate the trapping potential. With this experimental apparatus, single $^{174}\mathrm{Yb}^{+}$ ions are trapped, and the trapping conditions are optimized. In Section 4-2, the methods to observe the secular frequency are explained, and the secular frequency is measured. The measurement results of the secular frequency at multiple ion positions are then analyzed. Furthermore, the developed method is experimentally evaluated by producing electric charges at a single location by shining a laser, and the resulting secular frequency shift is measured over time. In Section 4-3, the same experiment is repeated with the locations of laser irradiation changed, and the resulting secular frequency shift is obtained at multiple ion positions. The location of produced charges is estimated from the measured secular frequency shift. The estimated location is compared with the location where the laser is irradiating in Section 4-4.

4-1. Experimental Setup

The ion-trap experiment basically requires an ion trap loaded in a vacuum chamber, a laser cooling system for ionized atoms, an electronic system to create the trapping potential, and an imaging system to detect the fluorescence emitted from trapped ions. A surface-electrode ion trap made of silicon and $^{174}\mathrm{Yb}^{+}$ ions are selected for the experiment. Three different lasers with wavelengths of 369.5, 398.9, and 935.2 nm are used for cooling, ionization, and repumping of the ytterbium ions. A helical resonator and a digital-to-analog converter (DAC) system are employed to deliver the RF voltage and DC potential, respectively. A commercial objective lens, a charge-coupled device (CCD), and a photomultiplier tube (PMT) are utilized to collect photons emitted from the trapped ions.

4-1-1. Surface-Electrode Ion Trap

In this experiment, a surface-electrode ion trap with aluminum copper alloy (AlCu) was used. The surface-electrode ion trap was fabricated on a silicon substrate with a size of 6 mm × 6 mm. A pair of RF electrodes, a pair of inner DC electrodes, located between the two RF electrodes, and 32 pairs of outer DC electrodes were included in the surface-electrode ion trap to displace trapped ions in a direction parallel to the longitudinal direction of the RF electrodes. The dimensions of the electrodes were 80 μm for the width of the loading slot, 37 μm for the width of the inner DC, 75 μm for the width of the RF electrode, and 8 μm for the inter-electrode spacing so that the ions were trapped approximately 108 μm above the trap surface. The width of the segmented outer DC electrode was 70 μm, and all electrodes were placed on the same plane. All electrodes had an overhang structure with a length of 4 μm to prevent exposure of the oxide pillar under the top electrode to trapped ions. To reduce the probability of laser scattering by minimizing the length of the laser path passing over the surface-electrode ion trap, the laser propagation paths were considered as shown in Beams 1 and 2 in Figure 4-1. In addition, as an additional laser propagation path, Beam 3 penetrating the slot was also designed.

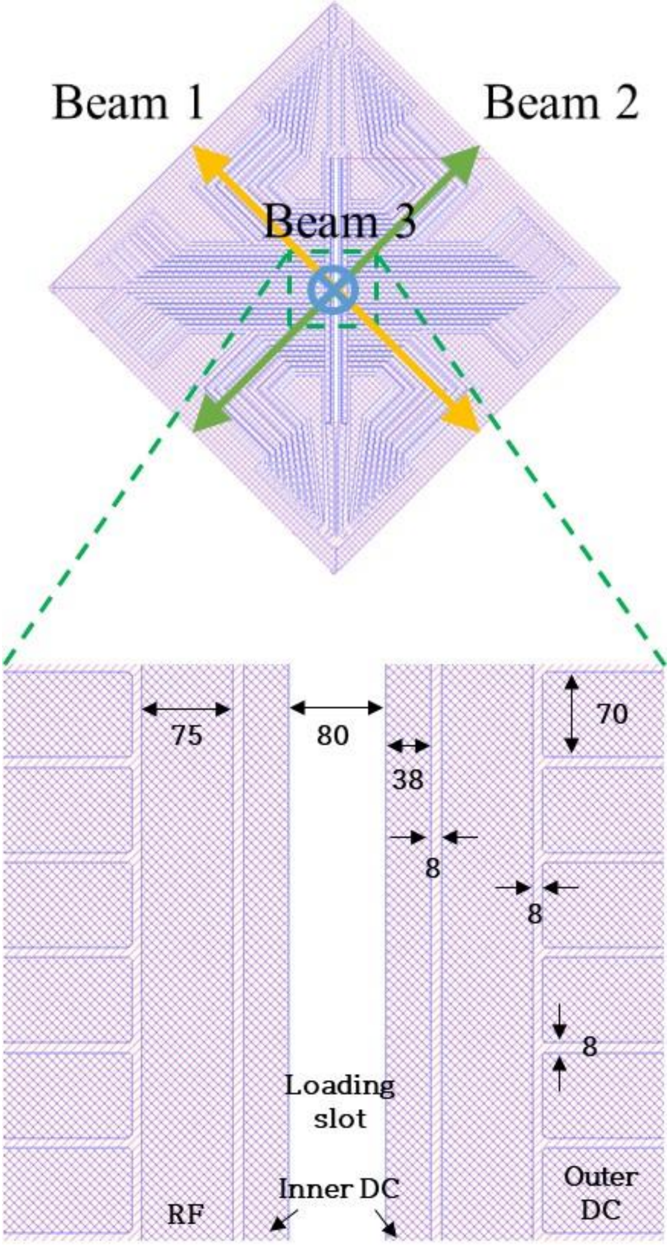

Figure 4-1. A schematic of the surface-electrode ion trap used in the experiment, including its layout and dimensions [70, 104]. Beams 1, 2, and 3 illustrate laser propagation paths. All values are given in micrometers.

The designed surface trap was implemented using the MEMS fabrication process. Figure 4-2 shows the fabrication flow chart of the surface-electrode ion trap. The most important process in all fabrication processes is cleaning. Thus, before beginning the fabrication process, cleaning with the Piranha solution was performed. The Piranha solution was prepared by mixing sulfuric acid and hydrogen peroxide in a ratio of 4:1, and a 4-inch (100) silicon wafer was immersed in the solution for 10 minutes. Thereafter, deionized (DI) water was applied to clean the wafer. The Si_3N_4 layers were deposited to a thickness of approximately 0.2 μm on both sides of the silicon substrate using a plasma-enhanced chemical vapor deposition (PECVD) process (Figure 4-2(a)). Then, approximately 1.6 μm of AlCu alloy (1 wt%) was constructed on the front surface using sputtering. The AlCu alloy was employed to prevent the formation of aluminum hillocks. After patterning the photoresist (PR) etch mask through conventional photolithography, the 1st AlCu layer was patterned through inductively coupled plasma (ICP) etching. Also, the Si_3N_4 layer under the AlCu layer was opened where the loading slot was created, by using a magnetically enhanced reactive ion etching (MERIE) process. The remaining PR etch mask after the etching process was removed with a PR stripper and a PR ashing process.

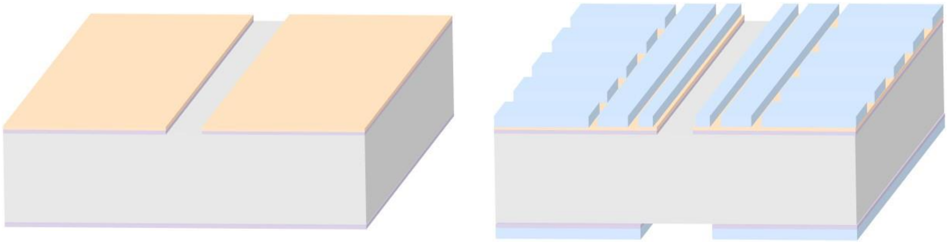

(a) Si_3N_4 and 1st AlCu patterning (b) SiO_2 deposition & patterning

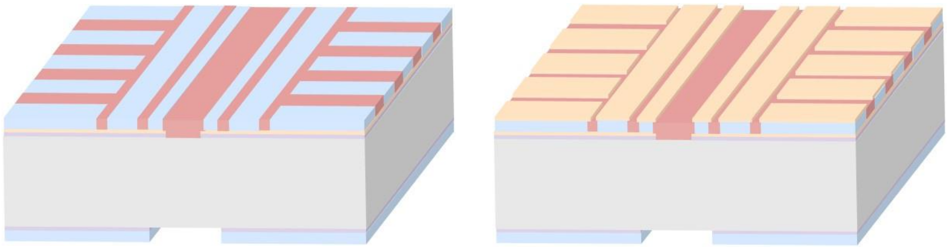

(c) PI coating & CMP (d) 2nd AlCu patterning

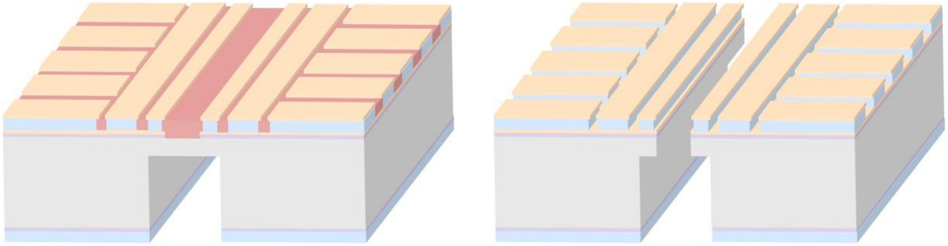

(e) Backside DRIE (f) PI removal & front side DRIE

Figure 4-2. Fabrication flow chart of the surface-electrode ion trap [70, 104]. The gray, purple, orange, blue, and red regions indicate silicon, Si_3N_4, AlCu, SiO_2, and PI, respectively.

A 10-μm thick SiO_2 layer was deposited using the PECVD process (Figure 4-2(b)). To compensate for the stress accumulated on the wafer, the thick SiO_2 layers were deposited on both sides like Si_3N_4 layers. Then, the 10-μm thick SiO_2 layer on the back side was also patterned using the MERIE process. This thick SiO_2 layer is used as an etch mask for the Bosch process to form the loading slot. The Si_3N_4 layer under the etched SiO_2 layer was also removed in this process. The SiO_2 layer on the front side was then etched using the MERIE process after going through PR patterning. In this process, the selectivity of SiO_2/PR was important. The typical selectivity of SiO_2/PR is 1.5~3:1. When the PR is thick, the etch profile (how vertical the oxide pillar is) typically becomes low. Conversely, when the PR is thin, the etch profile is improved; however, there is a potential risk of damaging the layer that needs to be protected during the etching process. Fortunately, our MERIE machine had a selectivity of nearly 5:1, and therefore approximately 2.8-μm thick PR was used to etch the 10-μm thick SiO_2 layer. Note that the thickness of PR was measured using an alpha step machine after patterning the PR.

After etching the 10-μm thick SiO_2 layer on the front side, the PR strip process was carried out, and then polyimide (PI) is spin-coated on the front side (Figure 4-2(c)). Since at least a 10-μm thick PI layer was required to cover the etched oxide pillar, a PI-540 was employed. To prevent the formation of voids during the curing of PI, after spin-coating of PI, the curing process was performed as follows: (1) 110˚C on a hot plate for 15 minutes, (2) 150˚C on the hot plate for 15 minutes, and then (3) 300˚C on the hot plate for 90 minutes. The dehydrated PI layer was planarized by a chemical mechanical polishing (CMP) process. After the CMP process, cleaning was performed using DI water for over 30 minutes. Note that organic solvents, such as acetone, can dissolve the PI, and therefore it must be careful in using organic solvents in this cleaning process.

The 2nd AlCu layer to be used as top electrodes was sputtered on the flat layer (Figure 4-2(d)). The thickness of the AlCu layer was approximately 1.6 μm. The PR patterning and ICP etching processes were applied to pattern the 2nd AlCu layer. The exposed silicon substrate was etched from the back side using the Bosch process (Figure 4-2(e)). In this process, the uniformity of the Bosch process in our machine was low, and therefore a fabrication margin of approximately 50 μm was left without forming the slot at once. The remaining PI was removed by a boiled PR stripper (Baker PRS-2000), and the Bosch process was carried out again from the front side of the substrate (Figure 4-2(f)). Scanning electron microscope (SEM) images of the fabricated surface-electrode ion trap are shown in Figure 4-3.

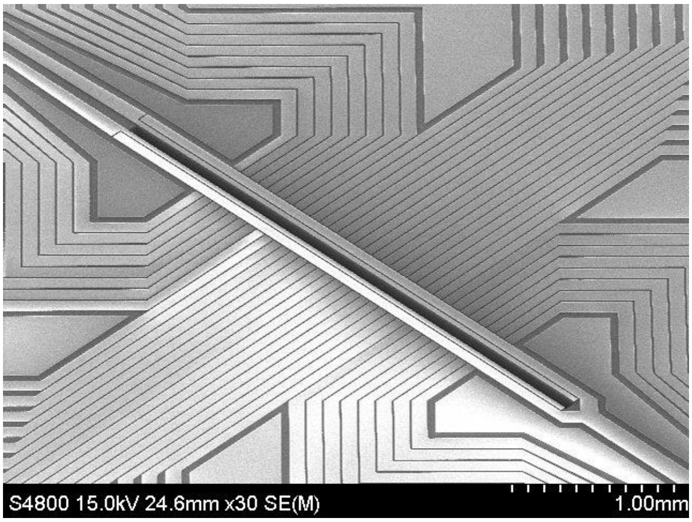

(a)

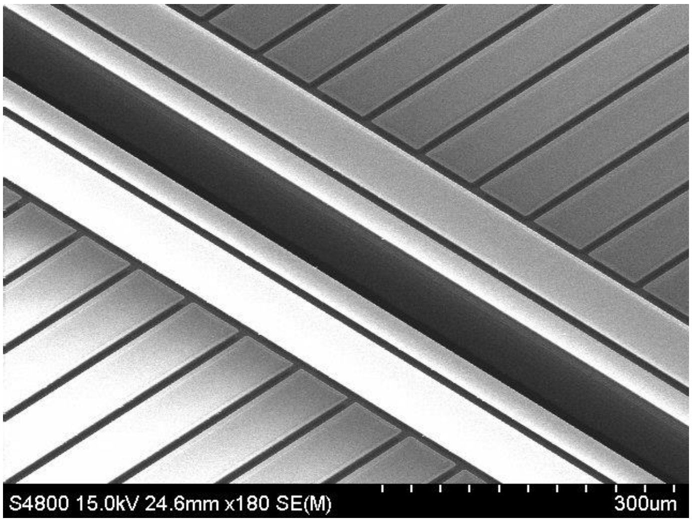

(b)

Figure 4-3. The SEM images of the fabricated surface-electrode ion trap [70, 104]. (a) A large area view at low magnification. (b) A magnified view around the trap center.

The electric connection of the fabricated surface-electrode ion trap was tested, and no issues were found. Next, as shown in Figure 4-4, the surface-electrode ion trap was mounted on a ceramic pin grid array (CPGA) and wire-bonded, with silicon spacers placed beneath the trap to enable laser propagation parallel to the trap surface. Single-layer capacitors of 820 pF were connected to all DC electrodes to prevent RF coupling. The capacitors were glued on the outside of the CPGA using a conductive epoxy (Epotek H21D) and annealed at 180°C on a hot plate. To ensure an unobstructed laser propagation path through the slot, a hole was drilled in the center of the CPGA.

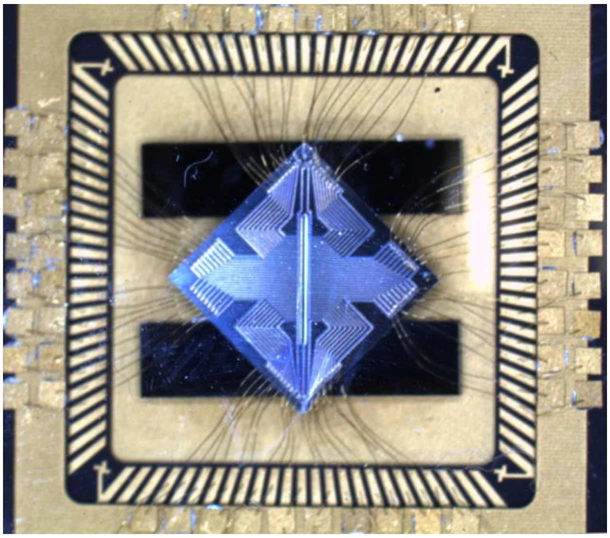

Figure 4-4. An optical view of the fabricated surface-electrode ion trap on the CPGA package [68, 104]. Single-layer capacitors are glued on the outside of the CPGA, and all electrodes and capacitors are wire-bonded.

The assembled surface-electrode trap was installed in a vacuum chamber, as shown in Figure 4-5. The vacuum was held while baking the system at approximately 200°C to remove any outgassing issues and then stored at room temperature. The final vacuum inside the chamber was estimated to be less than 2.0×10^{-11} Torr. To enhance the collection of photons emitted from trapped ions, a recessed viewport was installed on the front of the chamber so that the objective lens could be brought closer to the trap surface. Additionally, a ground shield was added to prevent the charging of the trap surface due to ambient light. The ion pump was left connected to continually maintain the vacuum inside the chamber, and the ion gauge was also left connected to continuously monitor the vacuum level inside the chamber.

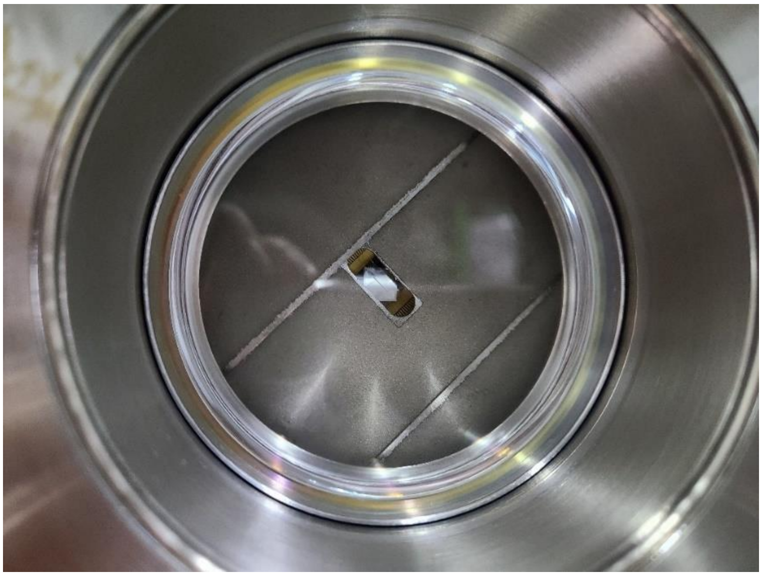

Figure 4-5. A picture of the surface-electrode ion trap mounted inside the vacuum chamber [105].

4-1-2. Lasers

The 369.5-nm, 398.9-nm, and 935.2-nm lasers were prepared to trap $^{174}\mathrm{Yb}^{+}$ ions. The 369.5- and 398.9-nm lasers were purchased from Moglab, while the 935.2-nm laser was from Toptica, and all lasers were modularized. To set up the 369.5 nm, an optical breadboard of 450 mm × 450 mm was used, as depicted in Figure 4-6. Electro-optics modulators (EOM) and an acoustic optics modulator (AOM) were installed to modulate and turn on and off the 369.5-nm laser. The threshold current and beam shape of the laser were measured after mounting the laser head to the edge of the breadboard. The threshold current is the value at which lasing starts and is the point at which flashing occurs when the output laser is reflected on a fluorescent paper. Additionally, the point at which the laser output becomes 1 mW is also considered a threshold when measuring the laser output with an optical power meter. The output beam shape was monitored using a beam profiler. To modify the elliptical beam shape of the 369.5-nm laser into a circular shape and minimize losses in both the optical isolator and fiber coupling, a pair of cylindrical lenses were placed between the laser head and the optical isolator.

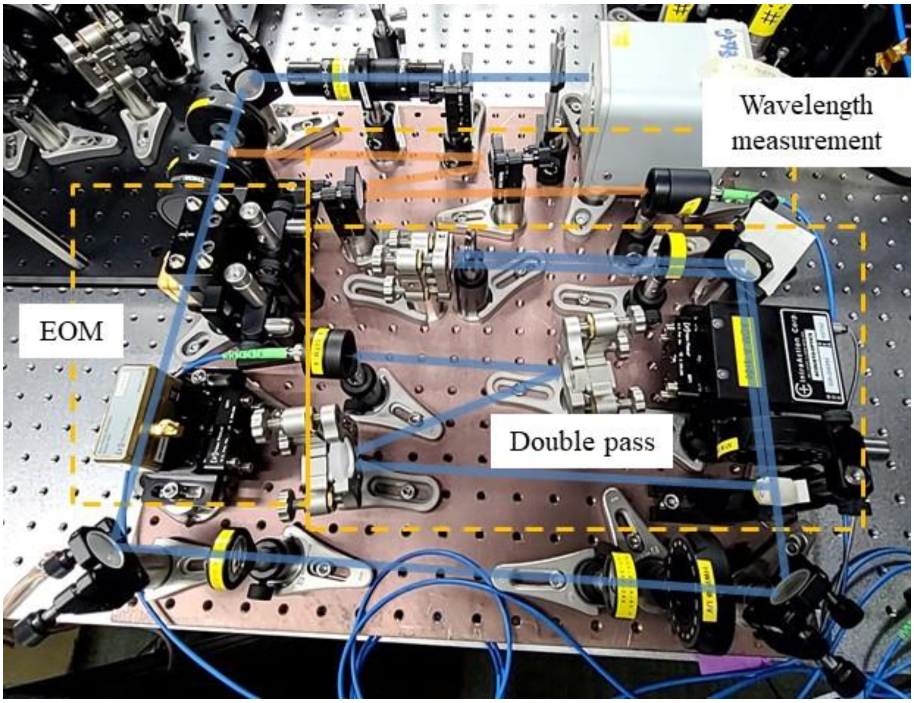

Figure 4-6. A picture of the 369.5-nm laser module. The blue and orange lines indicate the main laser path and the path for reading the laser frequency.

The laser delivered in a circular shape was aligned to pass through the optical isolator. According to the principle of the Faraday mirror, the optical isolator used polarization to prevent the light from traveling backward when the transmitted light was reflected. The beam power decreased to approximately 80% after passing through the optical isolator. Then, the laser passed through the half-wave plate (HWP) and then through the polarized beam splitter (PBS), dividing the laser path into two branches so that some were reflected and the others were passed. The dividing ratio could be controlled by the HWP, and the light reflected from the PBS was approximately 5% of the incident laser. After fiber coupling the reflected laser, it was sent to a wavelength meter and used to read the laser frequency. The laser transmitted in the PBS passed through the quarter-wave plate (QWP) and HWP, and then through a 2.1-GHz EOM and a 7.4-GHz EOM. If only the polarization was well matched, the loss was less than 10% in the 2.1-GHz EOM, however, the power loss reached almost 50% in the 7.4-GHz EOM. When passing through the EOMs, it was advantageous to transmit a small beam size because the aperture of the EOM was as small as 1 mm. However in the AOM, since diffraction occurred well when the beam size was as large as 3 mm, a pair of plano-convex lenses was used, and then the beam size was increased by approximately 3 times.

An additional PBS was utilized to separate the fiber coupling area from the double pass area. An HWP was placed in front of the PBS so that the laser incident on the PBS could be transmitted as much as possible and then passed through the AOM with maximum efficiency. Since the diffraction efficiency of the AOM was polarization-dependent, the polarization of the incident laser was crucial. However, the polarization state was not heavily considered in this laser module because the polarization returned in an inverted state after passing through the AOM and then passing again in the reverse direction. Fortunately, the diffraction ratio of the laser incident to the AOM was above

50% since the polarization state was maintained vertically while passing through the PBS. The first-order diffractive laser could be used for switching, and therefore only the 200-MHz shifted laser in the AOM could utilize this function. The zeroth-order laser was clipped with an iris, and only the first-order laser was reflected by the mirror and passed through the AOM again. As a result, the 400-MHz red-detuned laser was passed through the QWP again and reflected from the PBS. The reflected laser was fiber-coupled with an efficiency of approximately 40%. Therefore, the laser output from the laser head of approximately 10 mW was fiber-coupled up to approximately 100 μW, and the laser power delivered to the ions could be adjusted based on the power input to the AOM.

The 398.9-nm laser was designed simpler than the 369.5-nm laser because the installation of EOM and AOM was not required, as shown in Figure 4-7. As in the previous procedure, the output laser from the laser head passed through the optical isolator and then was delivered to a beam splitter. A window without AR coating was used, and two beams reflected from the front and back sides of the window were used for reading the laser frequency and charging experiments. A D-shaped mirror was placed in the middle of the path of the two beams to separate the two parallel beams. The main laser path transmitted in the window could be directly fiber-coupled and sent to the vacuum chamber. However, the 398.9-nm laser was used to ionize neutral Yb atoms and did not need to be delivered while operating the ions. Thus, a flip mirror was installed in the middle of the laser path to share the 398.9-nm laser with another chamber. It was designed to select which chamber to ionize neutral Yb atoms according to the state of the flip mirror.

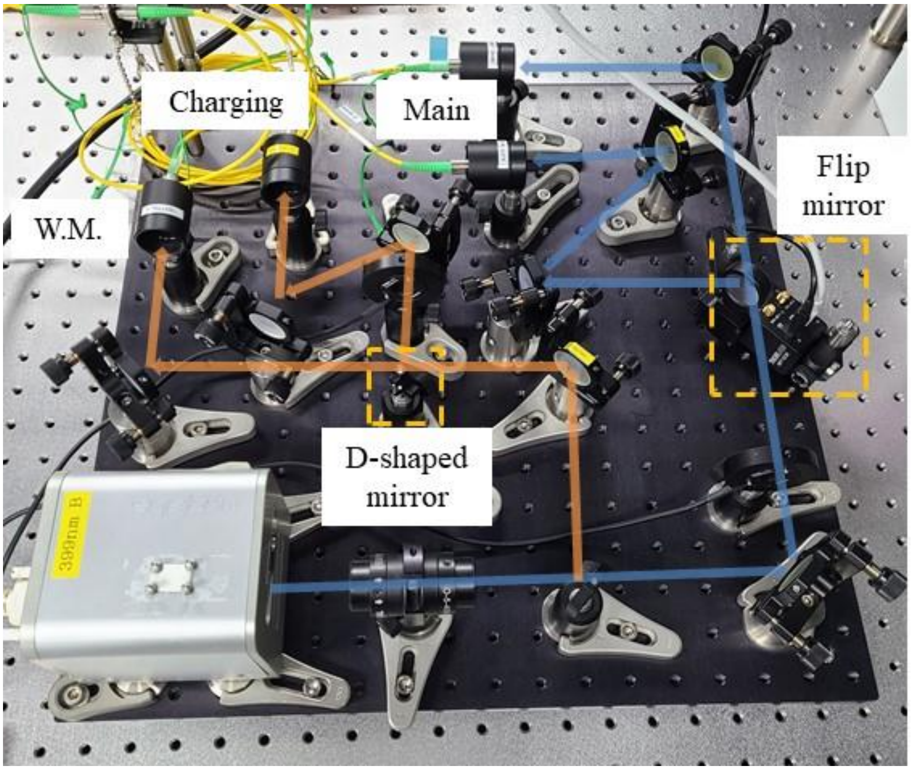

Figure 4-7. A picture of the modularized 398.9-nm laser. The blue and orange line shows the main laser path and the path for measuring the laser frequency.

The 935.2-nm laser module was designed simpler than the 398.9-nm laser module. Since this laser was delivered after passing through the optical isolator inside the laser head, the output laser coming from the laser head was immediately divided into two branches using a beam splitter. One path entered the wavelength meter after fiber coupling, and the other path was delivered to the vacuum chamber. Since the 935.2-nm laser had sufficient power, the frequency was mixed using two EOMs. The 320.57197 THz for $^{174}\mathrm{Yb}^{+}$ and 320.56925 THz for $^{171}\mathrm{Yb}^{+}$ had a difference of 2.72 GHz, an EOM to transmit both frequencies simultaneously, and the other EOM was used as a phase modulator for $^{171}\mathrm{Yb}^{+}$.

4-1-3. Electronics

The resonant frequency of the helical resonator was measured using a spectrum analyzer, as shown in Figure 4-8. When the network analyzer scanned a wide range of frequencies, the resonant of the helical resonator was confirmed to be approximately 32.38 MHz using the S11 measurement that read the reflected waveform. The cavity length with the largest Q factor was found by adjusting the position and rotation of the end cap.

The RF voltage applied to the ion trap was transferred, as shown in Figure 4-9. Two signal generators (SRS SG384) were employed to both apply an RF drive voltage and modulate the amplitude of the RF voltage. A power splitter/combiner was used to combine two RF signals of different frequencies.

The combined RF signal was transferred to an RF amplifier with an amplification ratio of 36 dB. The amplified RF signal arrived at a bi-directional coupler, which could show a reflected RF signal with a reduced ratio of approximately -20 dB. The forward RF signal was transferred to the RF electrode of the surface-electrode ion trap through the helical resonator.

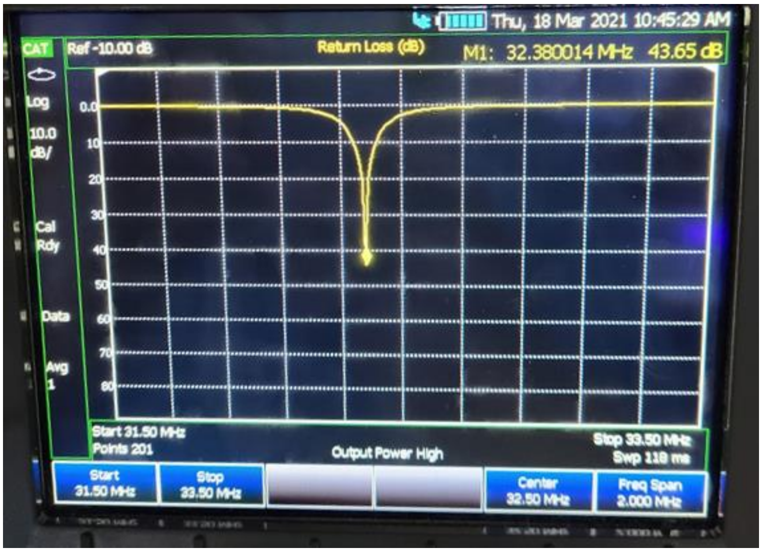

Figure 4-8. The measurement result of the resonant frequency of the helical resonator. The yellow line shows the measurement result, and the downward peak indicates the resonant frequency.

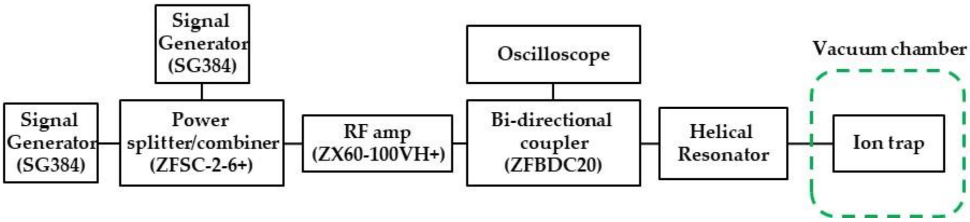

Figure 4-9. A diagram of RF voltage flow from the two signal generators to the ion trap.

One of the methods commonly used to measure the secular frequency of trapped ions is the parametric excitation method [106]. This method involves measuring the secular frequency by amplitude modulation of the drive RF voltage and observing that the secular motion of ions increases when the modulation frequency is equal to the secular frequency. Two RF signals of two different frequencies were combined for amplitude modulation. A similar effect could be achieved by using a frequency mixer to create a sideband, as shown in Figure 4-10. The method of measuring the secular frequency using the amplitude modulation of the RF voltage has the disadvantage that it is difficult to observe the secular frequency in the direction parallel to the RF electrode since an electric field cannot be applied in the direction parallel to the RF electrode.

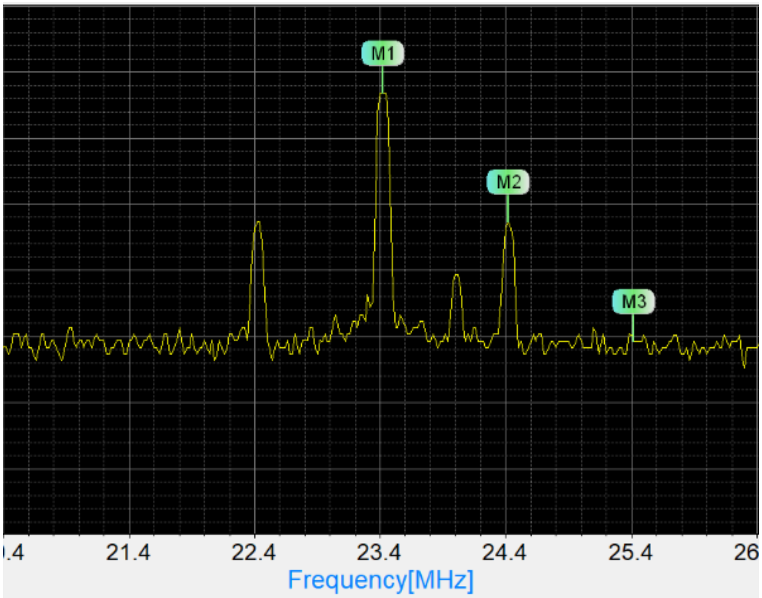

Figure 4-10. The sideband measurement result of the drive RF voltage.

The DC voltages were applied by using a DAC board. By using computer communication, DC voltages in the range of ± 15 V_{DC} could be simultaneously applied to the DC electrodes of the surface trap inside the chamber via four feed-throughs located at the rear of the chamber, as shown in Figure 4-11. In the beginning, a 16-ch DAC was used, but later it was replaced with a 32-ch DAC. When the 16-ch DAC was used, 2 channels were used for inner DCs, and the remaining 14 channels were used for outer DC electrodes. On the other hand, when the 32-ch DAC was used, 2 channels were used for inner DCs, and the remaining 30 channels were used for outer DC electrodes.

One of the outer DC electrodes did not have a filter, and therefore an RF signal could be applied to the outer DC electrode. This made the RF tickle could be performed through the DC electrode. This RF signal could affect the trapped ion in three directions so that the secular frequency could be measured in all directions. However, at the same time, it might distort the trapping potential. Thus, the secular frequency measured through the RF tickle method was a distorted value and varied depending on the magnitude of the applied voltage. When measuring the secular frequency using this RF tickle in our surface-electrode ion trap, a result shifted by approximately 10 kHz compared to the measurement using the parametric excitation method was obtained.

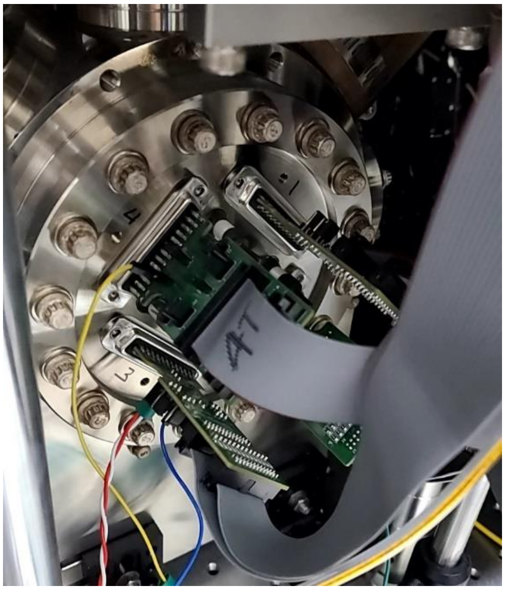

Figure 4-11. A picture of feed-through [105]. Four D-sub cables are connected to the chamber.

4-1-4. Imaging System

To collect photons emitted from trapped ions, an objective lens (imaging lens), a CCD, and a PMT were installed, as shown in Figure 4-12. A commercial lens (Photongears 15470) with a numerical aperture of 0.6 was used as the objective lens, Thorlabs' 1501M was used as the CCD, and H10682-210 manufactured by Hamamatsu was employed as the PMT. Since the focal length of the objective lens was a fixed value, the position of the lens was adjusted using a 3-axis micro-positioner. The laser was intentionally irradiated to the trap surface to cause light scattering on the trap surface, and the lens position was roughly adjusted using the image of the scattered light. Then, the exact position was adjusted in the stage of trapping ions.

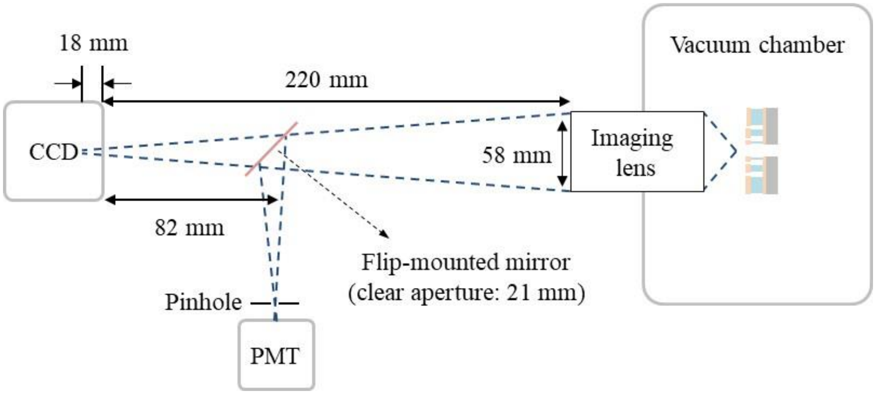

Figure 4-12. A schematic of the imaging system. The blue dash shows the propagation of the fluorescence emitted from trapped ions.

The CCD and PMT were also aligned using 3-axis micro-positioners to adjust their positions. Since the CCD has a photodetector approximately 18 mm inside the camera entrance, the CCD was installed at a distance where the fluorescence emitted from trapped ions forms an image. Since Yb^+ ions were used, a 370 nm band-pass filter (BPF) was installed in front of the CCD. In addition, a 650 nm low-pass filter was also fixed at the entrance of the CCD to block infrared rays delivered from fluorescent lamps. A pinhole was installed in front of the PMT to prevent errors caused by the ambient light. The 370 nm BPF was also installed in front of the PMT in the same regard.

A flip mount and a mirror with a diameter of 1 inch were used to switch the path of the light emitted from trapped ions to either the CCD or the PMT. The clear aperture of the 1-inch mirror was approximately 21.4 mm, and therefore the mirror was aligned approximately 82 mm in front of the CCD so that most light emitted from trapped ions could be reflected from the mirror. A similar effect could be achieved using a dichroic mirror.

4-1-5. Charging Laser System

To implement the charging phenomenon by shining the laser in the direction perpendicular to the surface-electrode ion trap, the fiber-coupled light from the 398.9-nm laser module was transmitted, as shown in Figure 4-

13. The 398.9-nm laser was delivered from a collimator, and a D-shaped mirror was positioned between the objective lens and the CCD to transfer the charging laser into the vacuum chamber. Since the objective lens was adjusted to the light emitted from the ions in the 369.5 nm wavelength, a lens was added between the collimator and the D-shaped mirror so that the 398.9-nm laser could be focused on the trap surface. The size of the laser spot formed on the trap surface was adjusted by changing the lens position in a direction parallel to the laser propagation path. In addition, the lens position was also moved on a plane perpendicular to the laser path to irradiate a desired location on the trap surface with the laser. The CCD image of the trap surface taken under laser irradiation was shown in Figure 4-14.

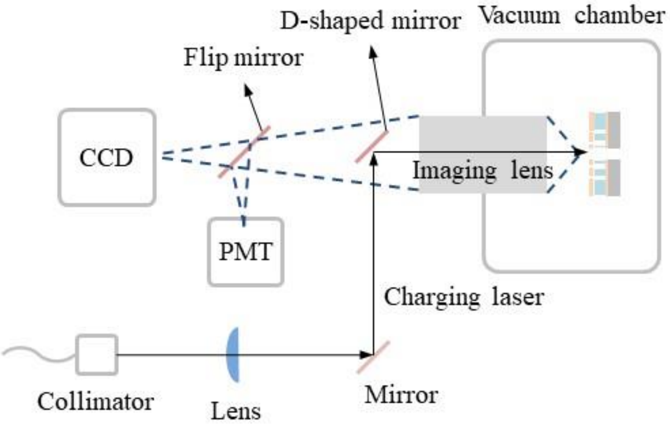

Figure 4-13. A schematic of the charging system. The black arrow shows the path for irradiating the laser onto the surface-electrode ion trap, and the blue dashes indicate the optical paths of the fluorescence emitted from the ion.

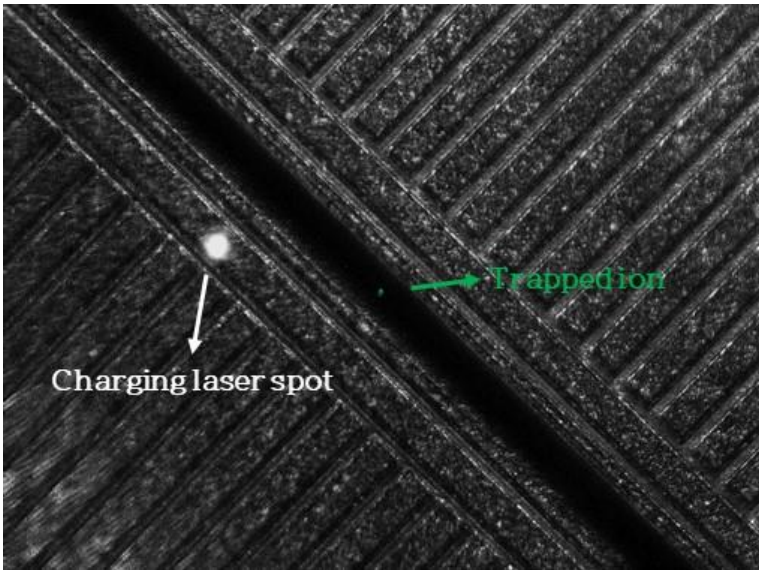

Figure 4-14. A CCD image of the trap surface and the charging laser spot. The green dot indicates a single trapped ion at the trap center.

4-1-6. Trapping Ions

The overall experimental apparatus is shown in Figure 4-15. Laser incident modules were located on both sides of the surface-electrode ion trap mounted in the vacuum chamber, and the 369.5-nm laser and the 398.9/935.2-nm lasers were delivered alternately in opposite directions. The helical resonator was attached to one side of the chamber, and four 25-pin D-sub cables were connected to the rear of the chamber. The objective lens was aligned in front of the vacuum chamber, and the CCD, PMT, and flip mirror were positioned according to the focal length of the lens.

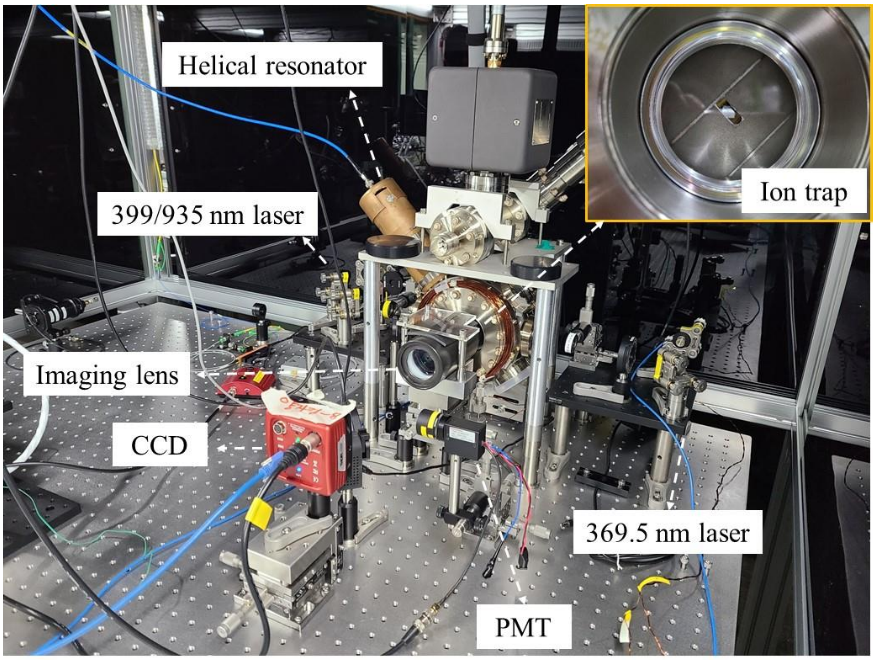

Figure 4-15. A picture of the overall experimental apparatus. Laser incident modules, the helical resonator, and the imaging system are located around the vacuum chamber.

Before trapping Yb$^+$ ions, the fluorescence of Yb neutral atoms was observed using the 398.9-nm laser. The accuracy of the frequency displayed on the wavelength meter was also evaluated with the fluorescence test because the frequency at which Yb atoms are excited is an absolute value. To perform the test, the 370 nm BPF of the CCD was replaced with a 398.9 nm BPF, and the objective lens and CCD were moved in a direction parallel to the optical axis to account for the difference in focal length between 369.5 nm and 398.9 nm. After aligning the delivery path of the 398.9-nm laser parallel to the surface trap, the position of the lens for the incident laser was adjusted so that the laser was delivered to the expected ion position. To prevent optical aberration, the laser was allowed to pass through the center of the plano-convex lens. The frequency of the 398.9-nm laser was set to 751.5265 THz to match the ${}^{1}S_{0}$-${}^{1}P_{1}$ transition of the ^{174}Yb atom, and the mode-hop free range of the 398.9-nm laser was prepared at approximately 5 GHz. A Yb natural oven containing various Yb isotopes was heated by delivering a current of 0.85 A to the tantalum foil surrounding the oven. The 398.9-nm laser frequency was changed by 50 MHz, and the number of photons counted in the CCD was plotted, as shown in Figure 4-16. The range of scanned frequencies was from 751.5255 to 751.5280 THz, and the number of collected photons was normalized based on the maximum value. The fluorescence of Yb neutral atoms is well-known, it was compared with theoretical values.

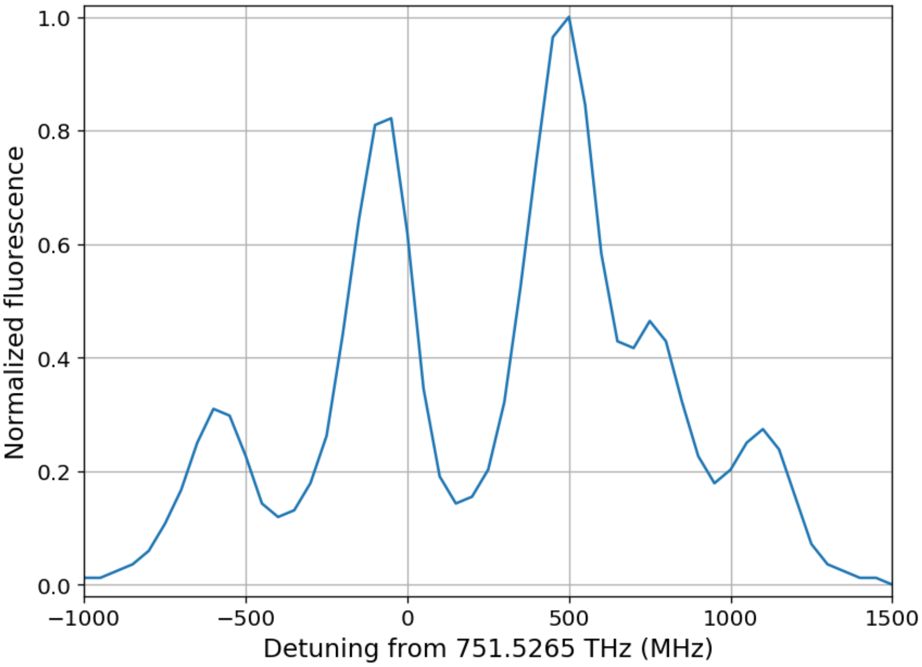

Figure 4-16. The fluorescence of Yb isotopes as a function of the detuning from 751.5265 THz.

The peak observed at the point where the detuning (Δ) was −600 MHz was the peak of ^{176}Yb atoms. On the other hand, the peak observed at the point where $\Delta = -50$ MHz was the peak of ^{174}Yb atoms, and according to this result, the frequency of the 398.9-nm laser for ionizing ^{174}Yb atoms was determined to be 751.52645 THz. Additionally, the peak shown at the point of $\Delta = +500$ MHz was the peak of ^{172}Yb and ^{173}Yb atoms, the peak near $\Delta = +750$ MHz was caused by ^{171}Yb (F=3/2) atoms, and the peak near $\Delta = +1100$ MHz was due to both ^{171}Yb (F=1/2) and ^{170}Yb atoms.

The key step for trapping ions was to precisely align the laser propagation path. To achieve this, the fluorescence of Yb neutral atoms was used to confirm the 398.9-nm laser path, and subsequently, the 935.2-nm laser and 369.5-nm laser paths were adjusted to the 398.9-nm laser path. As the 935.2-nm laser was transmitted alongside the 398.9-nm laser, a temporary mirror was placed in front of the chamber to reflect both lasers. The mirror alignment of the 935.2-nm laser was adjusted so that the two reflected lasers overlapped each other. Similarly, the 369.5-nm laser was adjusted to coincide with the 398.9-nm laser at the two points, in front of the 369.5-nm laser collimator and the 398.9-nm laser collimator, to achieve an overlapping laser path. Since it was unknown whether the alignment was uncertain during the first attempt to trap ions, the laser focus was adjusted to obtain a beam size of approximately 200 μm at the expected trap center. The 369.5-nm and 935.2-nm lasers had frequencies of 811.29140 THz for the 369.5-nm laser and 320.57197 THz, respectively.

Connecting the helical resonator to the trap and connecting other RF equipment could change the impedance, and therefore the cavity length of the helical resonator needed to be slightly adjusted. To this end, while applying a weak RF voltage, the cavity length of the helical resonator was adjusted until the intensity of the reflected RF signal became the smallest as shown in Figure 4-17. In this process, the RF drive frequency was also changed in units of 1 kHz. In our setup, the strength of the reflected RF signal was reduced to the same level as the noise signal of the oscilloscope. To provide sufficient trap depth at the trap center, approximately 180 V_{RF} was applied.

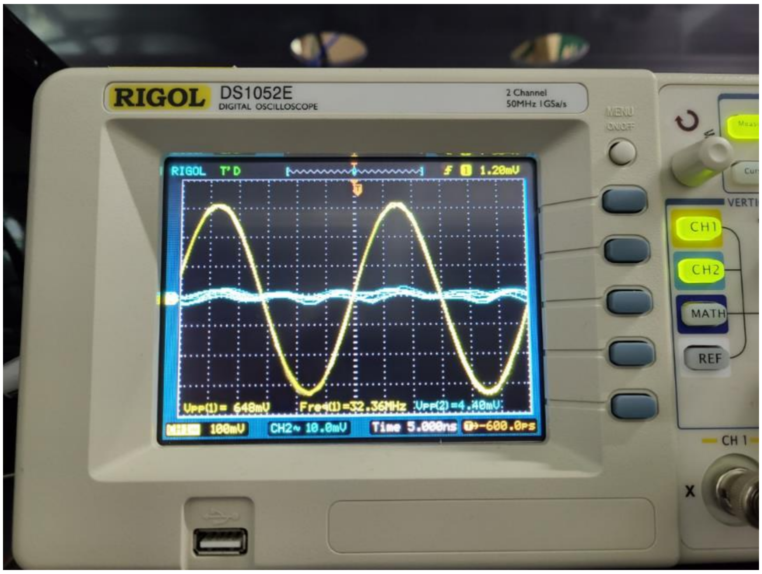

Figure 4-17. The real-time measurement of forward and reflected RF voltages at the bi-directional coupler.

When trapping ions for the first time, a potential well in the axial direction was formed using a pair of inner DC electrodes and 6 pairs of outer DC electrodes. Two outer DCs were bundled and a DC voltage of the same magnitude was applied, and Yb^+ ions were trapped by applying negative voltages to the inner two pairs of DC electrodes and positive voltages to the outer four pairs of DC electrodes.

To monitor the ions, the objective lens and CCD were focused on the trap surface. Then, the objective lens and CCD were moved by the ion height calculated in the simulation (approximately 108 μm). Even when the position of the ion was focused, the light emitted from the ion was weak and the ion might not be visible on the CCD image, therefore the trapping process was carried out with sufficient gain on the CCD.

When trapping ions for the first time, it was important to how much current was applied to the natural Yb oven. When a large current was applied to the oven, too much Yb neutral atomic flux was released, forming an ion cloud at the trap center, and the ion cloud was imaged blurry, making it difficult to identify whether the ion was trapped. Thus, to release the minimum flux of neutral atoms, trapping the ion was attempted in the state of flowing only 0.7 A, lower than the previous oven test. However, the alignment of the imaging system was not perfect, so even if the ion was trapped, it was not recognized. Therefore, as shown in Figure 4-18 (a), a large number of ions were trapped and an ion cloud was monitored. Then, after adjusting the alignment of the imaging system, a single ion was trapped while flowing only 0.68 A into the natural oven, as shown in Figure 4-18 (b).

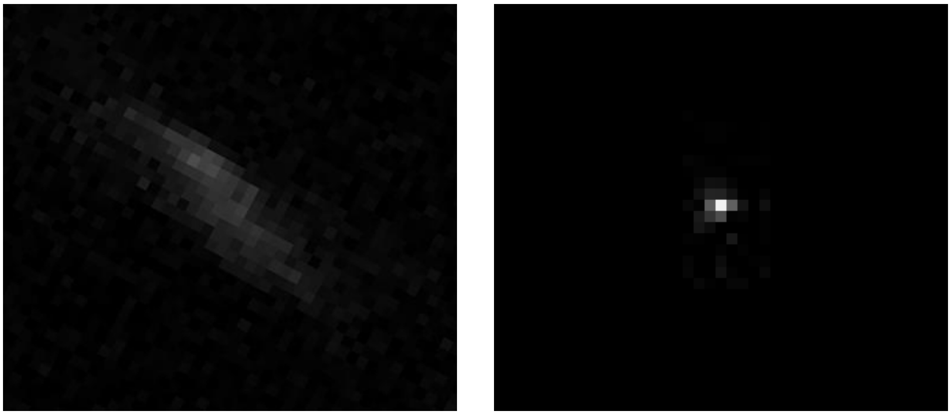

(a) (b)

Figure 4-18. The CCD images of trapped ions. (a) An image of the ion cloud. (b) An image of the single trapped ion.

The PMT alignment was performed with the single trapped $^{174}Yb^{+}$. Before that, the trap surface was first scanned in two dimensions to roughly align the PMT to the trap center. Then, while trapping the single ion, the PMT stage was scanned in 3 axes to find the ion position. In this process, to distinguish the fluorescence of the ion from the incoming light reflected from the trap surface, it was checked whether the signal from the PMT fell when blocking the transmission of the 935.2-nm laser. Note that the number of photons collected by the PMT decreases when the 935.2-nm laser was blocked since the repumping process was not performed. A 500-μm pinhole was used in the beginning, and then the size of the pinhole was reduced to block the background scattering signal. The size of the pinhole was reduced up to 50-µm, however, the alignment of the imaging system was not perfect in the beginning, and the light emitted from trapped ions could not converge at one point, and the image spread. Thus, the PMT alignment was completed using a 100-µm pinhole.

4-1-7. Trap Optimization

For the initial stage to optimize the trapping condition, the focus of incident lasers was optimized. The laser incident module was adjusted so that a beam waist was located at the ion position. If the laser was not focused near the ion position, the laser diverges and then laser scattering could occur on the trap surface, which could cause a charging effect. Thus, conditions were found for a laser path capable of trapping and cooling the ions with low laser power while minimizing the laser's contact with the trap surface.

A high RF voltage can cause the breakdown and kill the ion trap. Thus, a low RF voltage capable of trapping ions and holding the ions was investigated. To this end, the magnitude of the RF drive voltage applied in the state of trapping the ions was lowered by approximately 10 V_{RF}. In this process, the magnitude of the lowest RF voltage at which ions were lost was found. A low RF voltage can prevent the risk of breakdown, however, the ions can easily dissipate. Consequently, approximately 180 V_{RF} was determined as the RF drive voltage.

The aberration caused by the misalignment of the imaging system was corrected. When monitoring the ion image without adjusting the alignment of the imaging system, the ion image was displayed in the form of a long line, as shown in Figure 4-19(a). This was a phenomenon that occurred because the height of the objective lens did not match the ion position [75], and therefore the height of the objective lens was adjusted to make the ion image look circular. In this process, not only the height of the objective lens but also the height control of the CCD was important. Thus, the height of the CCD was also adjusted, and as a result, the ion image was obtained in a circular shape, as shown in Figure 4-19(b). To align in detail, the tilt error of the objective lens and CCD must also be corrected, however, due to the absence of a stage capable of correcting tilt error, aberration correction was performed only with a 3-axis micro-positioner.

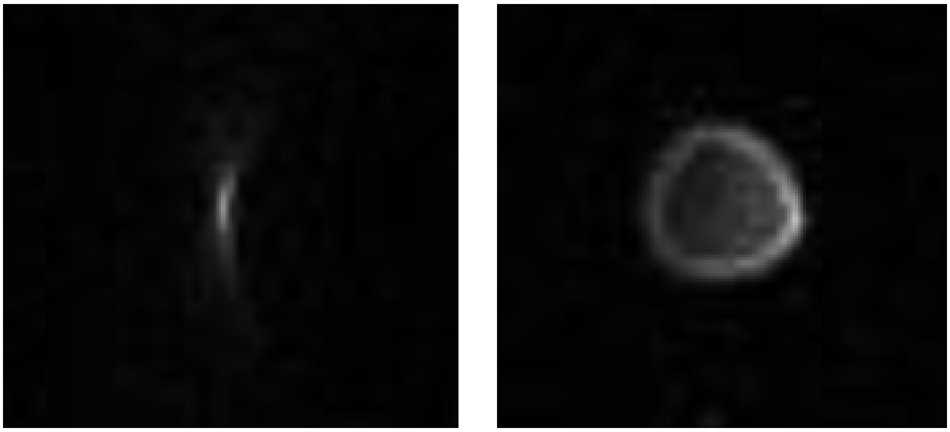

(a) (b)

Figure 4-19. Ion images monitored at CCD. (a) A line-shaped ion image due to height mismatch between the ion position and the objective lens. (b) A circular image monitored after correcting the height error.

The micromotion of ions due to the mismatch between the RF null and DC potential minimum was compensated for. Although the DC voltage set corresponding to the RF null was calculated in the simulation, the micromotion could occur due to simulation errors and microfabrication errors. There are various methods to compensate for the micromotion as follows:

- Lineshape measurement method
- Analysis of ion position change while varying the drive RF voltage
- Photon-RF phase correlation method
- Parametric excitation method

– Sideband spectroscopy method

First of all, the line-shape measurement was performed [107]. The lineshape measurement checks the cooling efficiency of trapped ions as a function of the detuning of the cooling laser. When the micromotion of trapped ions is severe, a broad plot is shown. In our setup, based on the resonant frequency of 811.291520 THz, the number of photons emitted from the trapped ion was counted from −80 MHz detuning. The interval between the detuning was 10 MHz in the range from −80 to −50 MHz and 5 MHz in the range from −50 to −5 MHz. As shown in Figure 4-20, when the detuning was large, the number of collected photons was at the level of 20 kHz. As the detuning decreased, the number of photons counted by the PMT increased, and a Lorentzian lineshape was observed. This indicated that the micromotion of trapped ions in our surface trap was not severe [107].

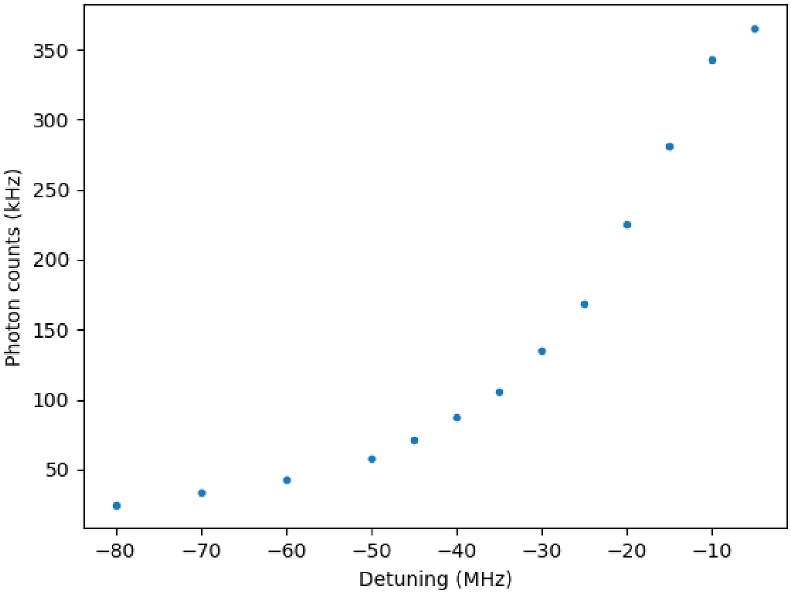

Figure 4-20. A lineshape measurement result. The detuning indicates the difference from the resonant frequency of cooling $^{174}Yb^{+}$ ions.

Next, the agreement between the RF null and the minimum point of the DC potential was investigated while varying the magnitude of the drive RF voltage [108]. When the RF null does not coincide with the DC potential minimum, the ion position changes when the RF voltage is changed. As a result of experimentation in our surface trap, when the RF voltage was adjusted from approximately 130 to 190 V_{RF}, the ion position changed little by little. The DC voltage set was adjusted so that the ion position would not change even if the magnitude of the RF voltage was changed, but it was not possible to establish a condition in which the ion position did not change completely.

The micromotion was also canceled using the photon-RF phase correlation method [109]. This method predicts the size of the micromotion by checking if there is a correlation when comparing one cycle of the RF voltage and the change in the number of photons emitted from trapped ions. When the correlation was first measured, the sinusoidal shape result was observed as shown in Figure 4-21(a). The correlation measurement was repeated by adjusting the DC voltages, and finally, a flat plot result was observed as shown in Figure 4-21(b). The disadvantage of this method is that the micromotion of trapped ions can be analyzed only in the direction in which the laser is delivered. Thus, it is typically difficult to identify the micromotion in the direction perpendicular to the surface trap using the photon-RF phase correlation method.

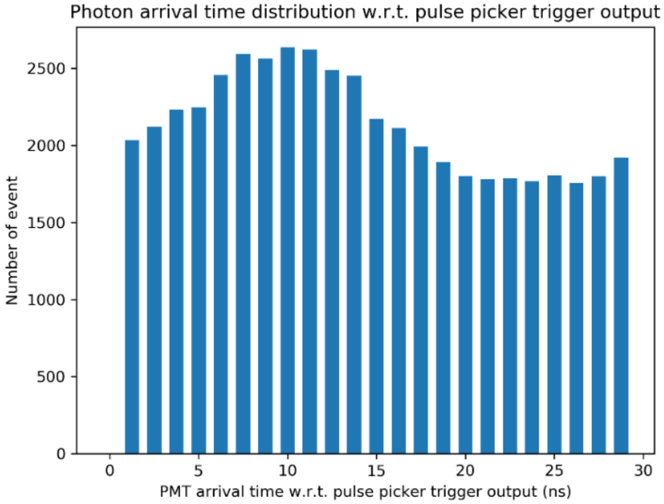

(a)

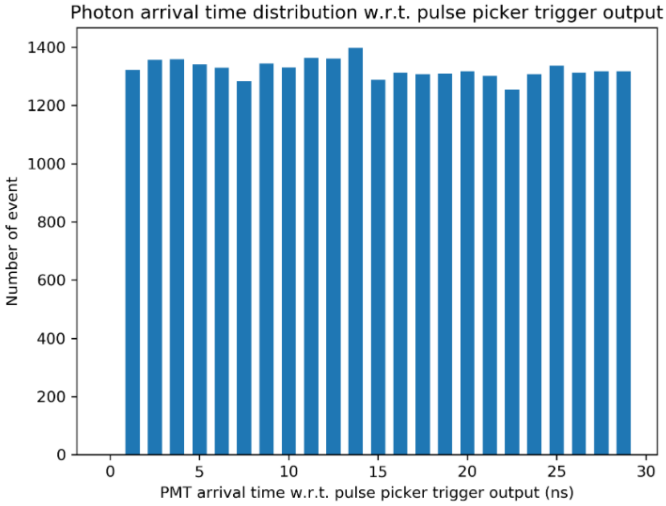

(b)

Figure 4-21. Measurement results of photon-RF phase correlation. (a) The measurement result before adjusting the DC voltages. (b) The measurement result after compensating for the micromotion.

The parametric excitation method is a method of inferring the micromotion of trapped ions through the size of the peak representing the secular frequency. The peak size must be compared while maintaining the magnitude of the modulation signal. It was considered that the micromotion was sufficiently canceled in the previous processes. However, as the magnitude of the modulation signal increased, a peak representing the secular frequency could be observed.

The resolved-sideband spectroscopy method analyzes the secular frequency of trapped ions and the size of micromotion by adjusting the size of the sideband compared to the carrier frequency of the laser [110]. When the micromotion exists, the peak of the micromotion coupled with the secular motion is observed at a frequency other than the secular frequency, and the magnitude of the micromotion can be inferred through the peak size. In my experimental setup, the above method could not proceed due to the absence of experimental apparatus capable of creating sidebands at the level of hundreds of kHz.

4-2. Secular Frequency Measurement

After performing micromotion compensation, the secular frequency was measured using the parametric excitation method. In principle, the secular frequency in the axial direction cannot be observed because it uses the amplitude modulation of the RF voltage. However, in our surface-electrode ion trap, I was able to observe the secular frequency in the axial direction. This may have arisen from the asymmetric geometry of the RF electrode [69] or unexpected coupling between the RF electrode and a segmented DC electrode. Since the DC voltages were applied asymmetrically with respect to the z-axis, the secular frequency in the x' and y' directions was measured in the radial plane. Although two radial secular frequencies were obtained, it was difficult to determine which secular frequency corresponded to each direction. The measured secular frequencies using the parametric excitation were approximately $2\pi \times (820,960,270)$ kHz.

The CCD can also be utilized to observe the secular frequency. When the trapped ion does not experience the signal of both the same frequency as the secular frequency and the same direction of the secular motion, the ion image in the CCD appears as shown in Figure 4-22(a). Conversely, when a signal with a frequency corresponding to the secular frequency is applied in the same direction as the secular motion, the ion motion is enhanced, as shown in Figure 4-22(b). However, since the process of continuously acquiring images of trapped ions using the CCD necessitates a considerable amount of data, the PMT is used to observe the secular frequency in the following experiments.

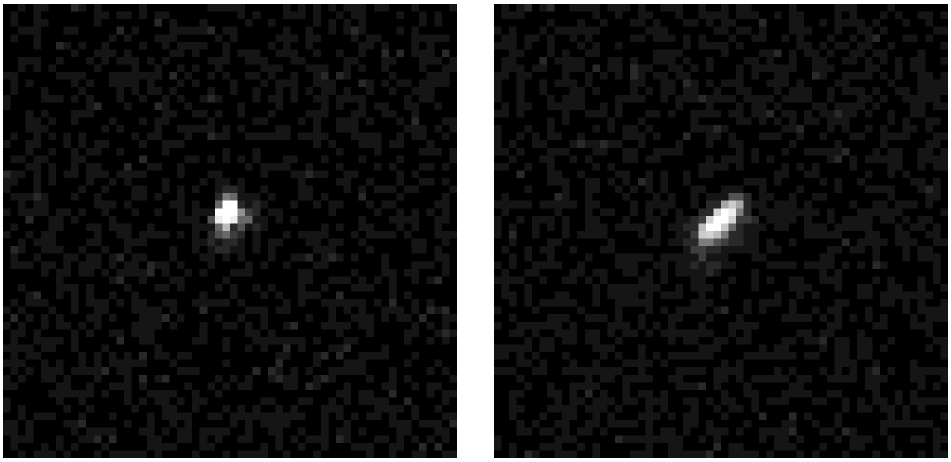

(a) (b)

Figure 4-22. Ion images monitored by the CCD during the secular frequency measurement. (a) The ion image when the ion does not feel the signal of the same frequency as the secular frequency. (b) The ion image when the ion feels the signal of the same frequency and the same direction of the ion's secular motion.

To experimentally determine whether laser-induced stray charges cause $\Delta\omega_z$, the secular frequency is measured before and after irradiating the trap surface with the charging laser. The laser has a beam radius of 2 μm and a power of 20 μW. To measure the secular frequency once per minute, the modulation frequency interval is set to 0.1 kHz, and the scan range is set to 10 kHz. The secular frequency is identified from the downward peak observed in the result of collecting the photons emitted from the trapped ion as a function of the modulation frequency. The blue, orange, and green lines in Figure 4-23 show the measurement results of secular frequency before and after shining the charging laser, and after charge dissipation, respectively. The measured frequencies before and after shining the laser, and after charge dissipation are $2\pi \times (267.88, 273.44, 267.75)$ kHz, respectively. The shift in the secular frequency is approximately $2\pi \times 5.56$ kHz after laser irradiation, indicating a negative sign of Q according to Eq. (2.7).

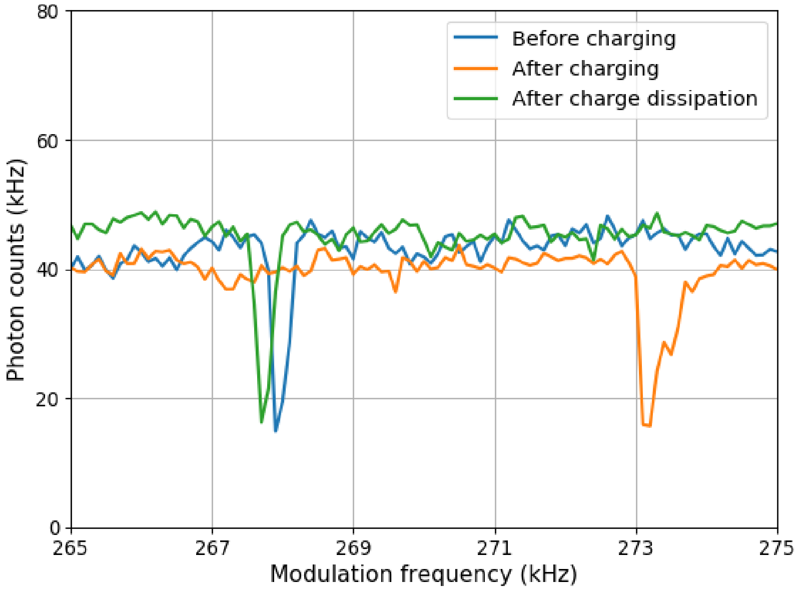

Figure 4-23. Collection results of photons emitted from the trapped ion as a function of the modulation frequency. The blue, orange, and green lines show the results before and after charging, and after charge dissipation, respectively. The downward peaks indicate the secular frequency. The observed frequency before charging is approximately $2\pi \times 267.88$ kHz, whereas the observed frequency after charging is approximately $2\pi \times 273.44$ kHz. The secular frequency returns close to its original value after the charge dissipates, which corresponds to $2\pi \times 267.75$ kHz.

The secular frequency was measured over a 10-minute period, and the results are presented in Figure 4-24. The time axis indicates the time elapsed since the first secular frequency measurement. The measurement procedure involved measuring the secular frequency with the charging laser turned off for the first 2 minutes, followed by observing the secular frequency for the next 5 minutes with the laser turned on. The laser was then turned off to dissipate the existing charge, and the secular frequency was measured again. The difference between the measured secular frequency before and after laser irradiation was used to estimate the effect of laser-induced stray charges, and the errors were calculated based on the standard deviation of the measured secular frequency after shining the laser. As shown in Figure 4-24, the measured secular frequency is uniform before the laser is turned on, indicating that the effects of other factors are negligible. Since the measured secular frequency at 3 minutes is almost uniform until 7 minutes, suggesting that the charge generation reaches saturation within 1 minute. Within 1 minute of blocking the laser irradiation, the secular frequency returns close to its original value. This finding is different from another study that reported time constants of t_1=78 and t_2=650 seconds using aluminum electrodes [88]. The 398.9-nm laser used in this study may have a fast dissipation rate due to its low photon energy, which can lead to the photoelectrons being shallowly trapped in the native oxide layer. Alternatively, the native oxide layer in our surface-electrode ion trap may be thinner than that in the previous study.

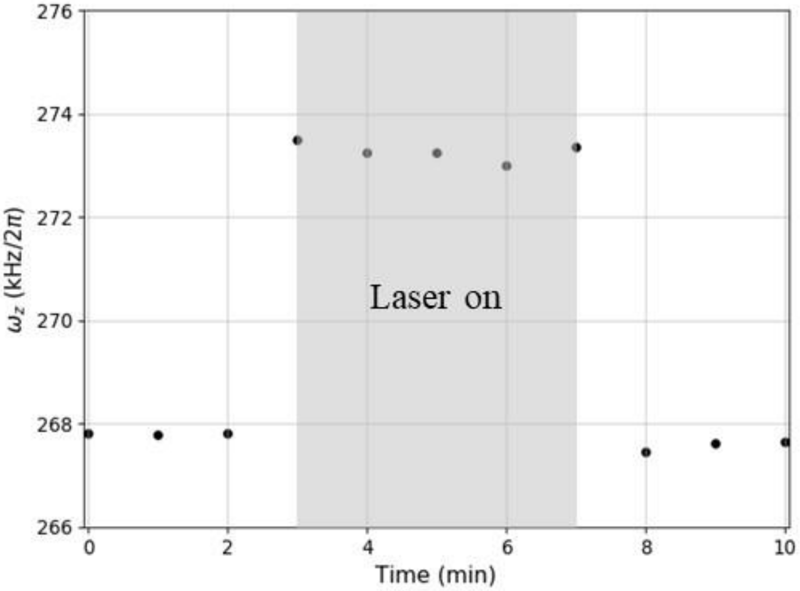

Figure 4-24. The measurement result of secular frequency (ω_z) over time. The gray box indicates the time of irradiating the charging laser. The ω_z is uniform from 0 to 2 minutes and increases in the gray box. Afterward, ω_z returns close to its original value when the laser is turned off again.

4-3. Location Estimation of Laser-Induced Charge

The procedure for obtaining $\Delta\omega_z$ is as follows: z_{ion} is changed by approximately 20 μm, and CCD images are used to estimate the distance over which the ion position changes. For each ion position, the initial secular frequency is measured, followed by shining the charging laser and measuring the secular frequency shift. The measured $\Delta\omega_z$ is shown in Figure 4-25, where the largest value of approximately $2\pi \times 6.52$ kHz is observed near

$z_{ion} = -20$ μm, and the value decreases as z_{ion} moves away from this point. The $\Delta\omega_z$ as a function of z_{ion} is curve-fitted, where only z_{ion} changes, and x_{ion} and y_{ion} are set to zero in Eq. (2.10). To account for the possibility of stray charges occurring at multiple locations, the curve fitting is performed for n from 1 to 3 in Eq. (2.10). The curve fitting results in only one set of $|x_q|$ and z_q, which is uniform regardless of n. However, the estimated amount of charge decreases as n increases, suggesting that the number of charge locations is one. The $|x_q|$ and z_q are estimated to be 47±26 μm and −25±11 μm, and Q is obtained as −277±64e. Notably, analyzing $\Delta\omega_z$ as a function of z_{ion} using Eq. (2.10) can only yield the magnitude of x_q.

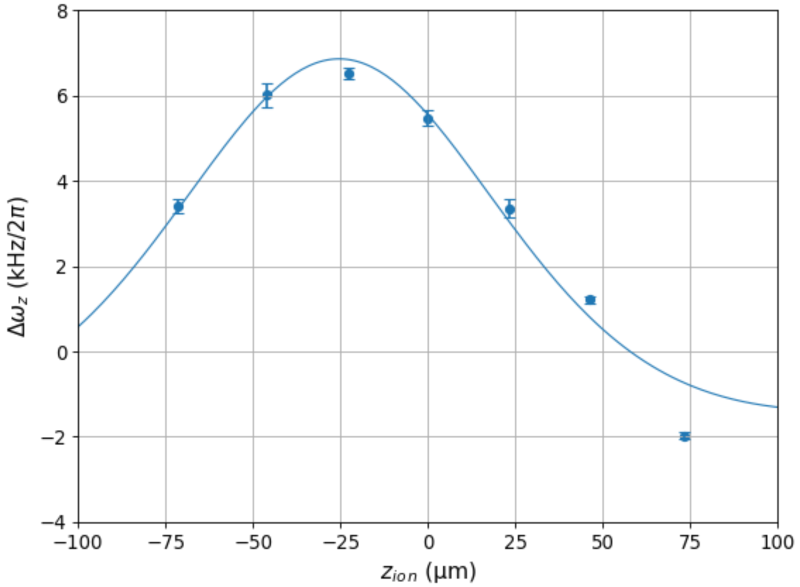

Figure 4-25. The Measurement result of $\Delta\omega_z$ as a function of z_{ion}. Based on the measurement result, the estimated $|x_q|$, z_q, and Q are 47 μm, −25 μm, and $-277e$, respectively.

To determine the sign of x_q, $\Delta\omega_z$ is observed while varying x_{ion} by approximately 1.7 μm within the range from −5 to +5 μm. It must be noted that the micromotion of the trapped ion becomes severe when the ion moves away more than 5 μm in the x-axis, and therefore the change in x_{ion} is limited to within 5 μm. As shown by blue dots in Figure 4-26, the measured $\Delta\omega_z$ is the largest near $x_{ion} = -5$ μm, and gradually decreases along x_{ion} moves away from −5 μm. The orange line in Figure 4-26 represents the calculation result using Eq. (2.10), where y_{ion} and z_{ion} are set to zero, and the value of x_q, z_q, and Q are assumed to be −47 μm, −25 μm, and $-277e$, respectively, based on the estimated results of $\Delta\omega_z$ as a function of z_{ion}. The sign of x_q is inferred to be negative (−) because the measured $\Delta\omega_z$ decreases as x_{ion} increases, and the plot of measured $\Delta\omega_z$ is similar to the calculated $\Delta\omega_z$. It must be noted that if the sign of x_q is opposite, the plot will be flipped over the y-axis.

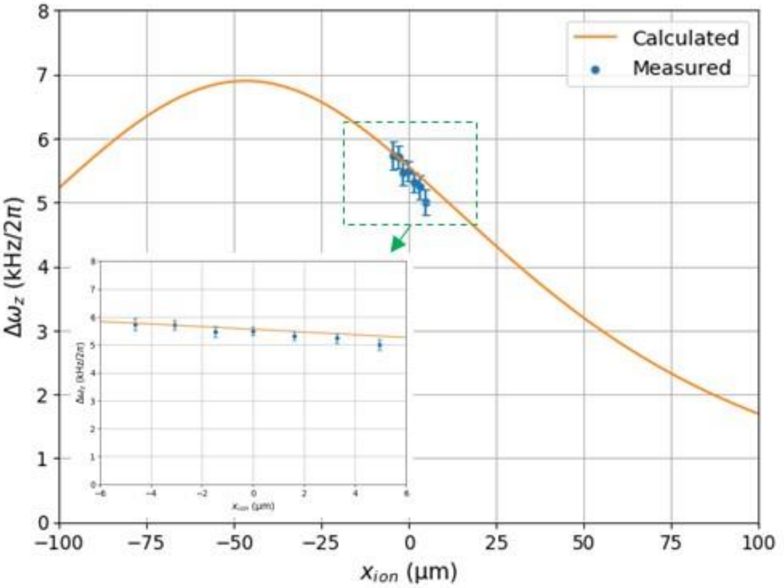

Figure 4-26. Measurement and calculation results of $\Delta\omega_z$ as a function of x_{ion}. The blue dots and the orange line show the measured result and the calculated result of Eq. (2.10), respectively. The interval between blue dots is approximately 1.7 μm, and the measurement is performed in the range from −5 to +5 μm in the x-axis. The orange line is drawn using the $|x_q|$, z_q, and Q estimated at (a). Since the measured $\Delta\omega_z$ decreases along x_{ion}, the sign of x_q is inferred to $(-)$. The inset shows the magnified plot in the range from −6 to +6 μm. Error bars indicate standard deviations.

4-4. Location Analyses of Laser-Induced Charges

The estimated location of the produced charge is compared to the region where the laser is irradiating. Figure 4-27 shows a CCD image of the surface-electrode ion trap and laser irradiation regions. The laser irradiation regions are identified from the laser spot that appears on the trap surface when the charging laser is blocked or not. Marks 1, 2, and 3 indicate the regions where the laser spot is observed. Among the marks, Mark 1 is the region where the above experiment is performed, and the coordinates are $x = -51 \pm 6$ μm and $z = -23 \pm 5$ μm compared to the initial ion position indicated by the green dot in Figure 4-27. The uncertainty represents the covariance of the laser spot image in the Gaussian fitting. The result shows that the estimated coordinates of the produced charge are consistent with the coordinates of the laser irradiation region within the margin of error. The same experiments are repeated twice more by changing the laser irradiation region. The investigation is repeated while shining the charging laser on Marks 2 and 3 in Figure 4-27, and the corresponding results are summarized as Cases 2 and 3 in Table 4-1. The sign of z_q in Case 2 and x_q in Case 3 is intentionally set to be opposite compared with Case 1 to validate that the sign of coordinates can be correctly identified. When Case 1 and Case 2 are compared, the sign can be distinguished even when the sign of z_q is opposite, and the magnitude of z_q can also be correctly estimated within the margin of error. Comparing Case 1 and Case 3, it is correctly distinguished that the sign of x_q is opposite.

The magnitude of x_q is also correctly estimated within the margin of error. Note that the accuracy of estimated amounts cannot be analyzed, since theoretical indicators that can compare the amount of produced charges do not exist.

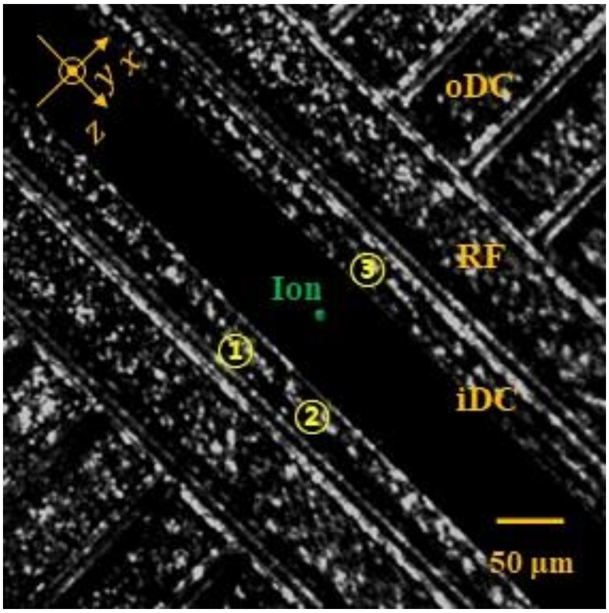

Figure 4-27. A CCD image of the surface-electrode ion trap in the vicinity of the trapped ion. The green dot indicates the initial ion position, and Marks 1, 2, and 3 show laser irradiation regions.

Table 4-1. Estimated values from the measured $\Delta\omega_z$ and the coordinates of laser irradiation regions. Cases 1, 2, and 3 indicate the results when the laser irradiates Marks 1, 2, and 3 in Figure 4-27, respectively. Estimated values indicate the estimated results in the curve fitting, and the actual values mean the identified coordinates of laser irradiation regions. The actual amount of produced charges cannot be obtained, and therefore the actual Q are presented as (–). The unit of x_q and z_q is μm, and the unit of Q is e.

	Estimated values			Actual values		
	x_q	z_q	Q	x_q	z_q	Q
Case 1	−47±26	−25±11	−277±64	−51±6	−23±5	–
Case 2	−66±31	47±18	−489±78	−54±3	49±3	–
Case 3	51±14	−4±9	−86±2	59±3	−5±3	–

The above experiment was performed only for the situation where the laser was irradiated at a single point. I attempted to perform experiments by shining the laser at multiple points simultaneously. However, it was challenging to generate charges at multiple locations at the measurable level to the trapped ion. For example, to simultaneously irradiate two points of the trap surface with the laser, one laser source may be divided into two branches and the two laser paths may be delivered individually. To divide one laser source into two paths, there is a method using an AR-uncoated window and a method using a beam splitter. A schematic of the laser path into two branches using a window is shown in Figure 4-28(a). A plano-convex lens was aligned on the laser path so that the laser from the collimator was focused on the trap surface. Then, using a 5-mm thick AR uncoated window, the laser was reflected once from the front and back sides of the window. Since the laser reflected from the front and back sides of the window naturally became two parallel beams, it was possible to irradiate two points of the trap surface with the laser at the same time, as shown in Figure 4-28(b). However, the distance between the two points was as far as approximately 500 μm and the power loss was severe, therefore the secular frequency shift due to the two charges was not observable. A thin window could be used to narrow the distance between the two points; however, there was a problem that the divided lasers interfered with each other.

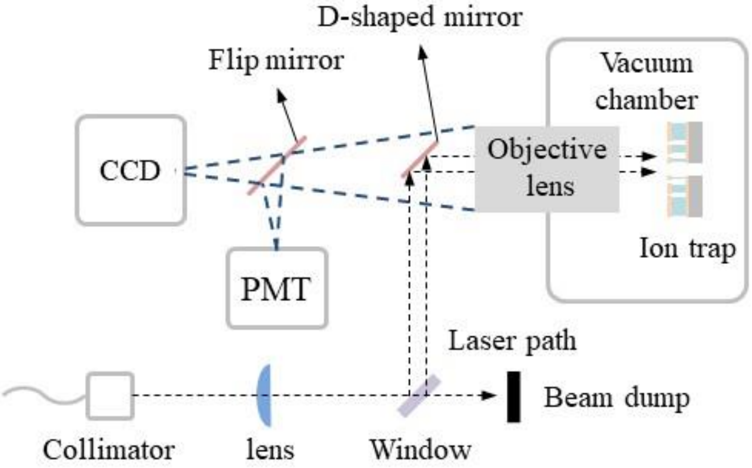

(a)

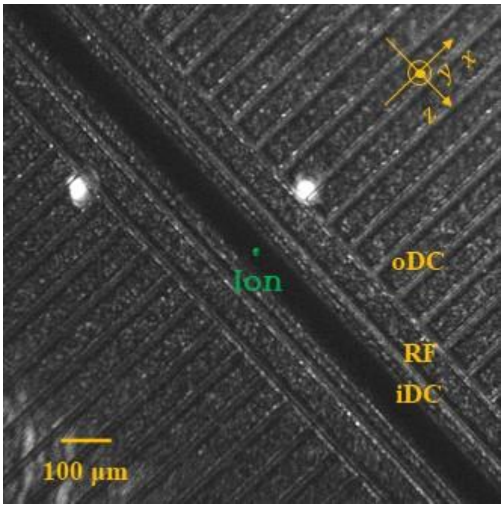

(b)

Figure 4-28. Schematic and CCD image of two laser paths by a single laser source. (a) The schematic of the optical setup using an AR-uncoated window to split the incident laser into two paths. (b) The CCD image of the trap surface and the two laser spots.

As another method, as shown in Figure 4-29, the beam splitter (BS) was used to divide the single laser source into two paths. The transmitted light from the beam splitter was reflected at a mirror and delivered to the trap surface. Although it was possible to prevent the loss of incident laser power, the length of one side of the beam splitter reached approximately 1.3 cm. In addition, when the mirror was arranged to create two parallel beams, an optical path difference was at least 1.2 cm, resulting in a difference of more than 1 mm between the two spots on the trap surface.

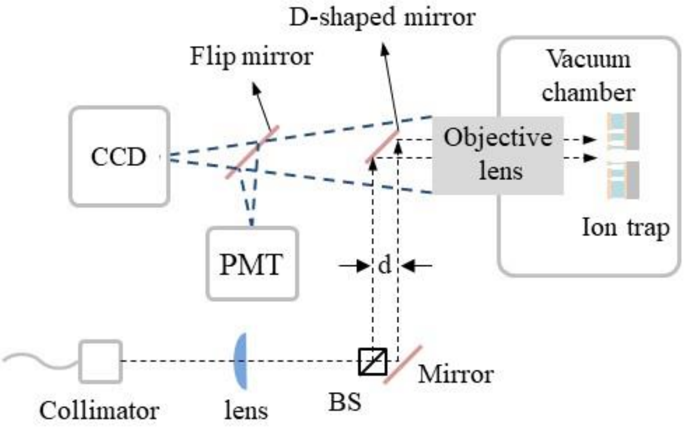

Figure 4-29. A schematic of an optical setup to make two laser propagation paths by a single laser source using a beam splitter. The transmitted laser from the BS is reflected at the mirror and delivered parallel in the direction of the reflected laser path in the BS. The d means the optical path difference between the two laser paths, and both laser paths are reflected in the D-shaped mirror.

When two laser sources were used, two individual laser paths could be created, as shown in Figure 4-30(a). Also, the laser irradiation positions on the trap surface might be precisely controlled. To this end, two collimators were used to deliver two laser beams, and the two laser propagation paths could be adjusted by each lens and mirror individually. However, since a mirror must be located between the objective lens and the CCD to inject the laser in the direction perpendicular to the surface-electrode ion trap, loss inevitably occurred in the process of collecting the light emitted from the trapped ion by the CCD and PMT. There was approximately 50% loss when using one D-shaped mirror. Two D-shaped mirrors were needed to deliver two individual laser paths to the surface-electrode ion trap, respectively. However, the two D-shaped mirrors installed alternately blocked all the light emitted from the trapped ion as shown in Figure 4-30(b), making it impossible to monitor the ion image on the CCD. Thus, it may be possible to create charges at two locations simultaneously on the trap surface using two laser sources. However, there is a problem in that the fluorescence of the trapped ion cannot be detected on the CCD and PMT, and therefore the experiment to measure the secular frequency shift by producing charges at multiple locations was not performed.

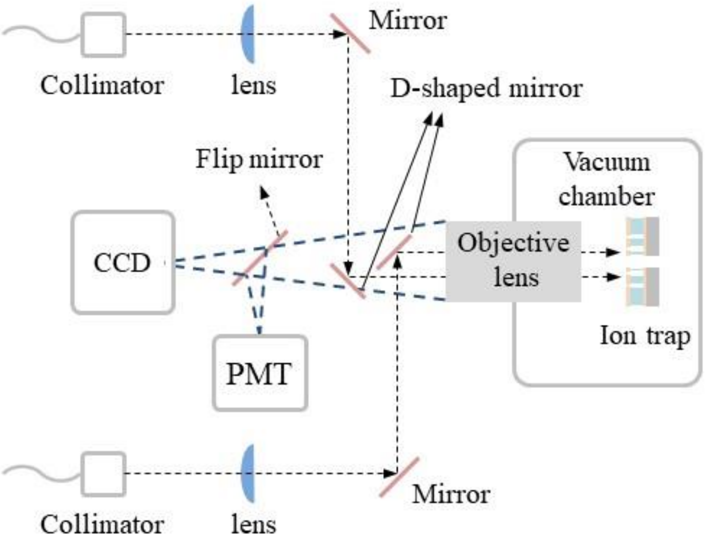

(a)

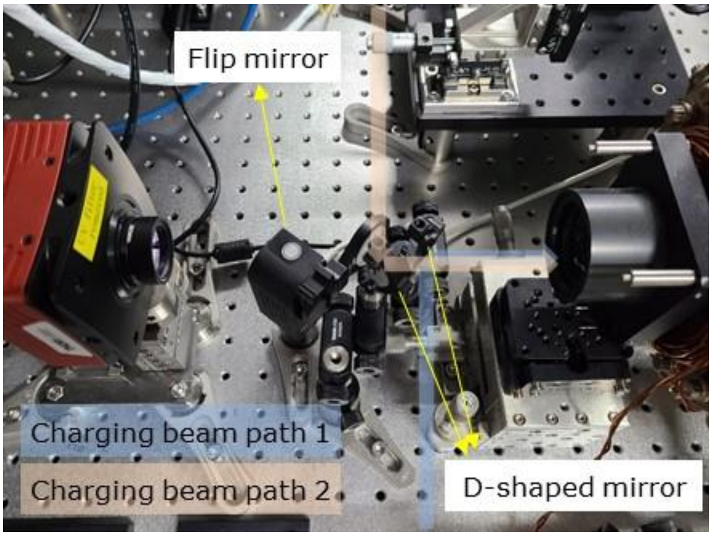

(b)

Figure 4-30. A schematic and picture of two laser paths using two laser sources. (a) The schematic of two individual laser paths using two D-shaped mirrors. (b) The picture of the optical setup using two D-shaped mirrors.

The following guidelines and tips are recommended for estimating the locations of laser-induced stray charges. First, it is suggested to measure the secular frequency shift by uniformly moving the ion along the z-axis until the spacing between the ion and the nearest electrode is reached. If the frequency shift approaches zero near $z_{ion} \cong$ ion-electrode spacing and a peak in the plot of secular frequency shift is observed, and curve fitting can be performed. However, if the frequency shift does not approach zero, additional measurements may be required by moving the ion further along the z-axis. To perform the curve fitting, it is necessary to obtain measurement results at different ion positions at least three times more than the expected number of stray charge locations.

In the process of estimating the fitting parameters, the margin of error for x_q is the largest among the fitting parameters. According to Eq. (2.10), since the calculation of x_q is carried out in the form of a square, the margin of error for x_q may be larger than that of z_q. The margin of error for z_q is less; however, the estimated margin of error is 10~20 μm. Additionally, the margin of error for Q is calculated to be a level of several to tens of electrons. The margin of error can be reduced by compensating for $\omega_{z0}(z_{ion})$. The DC voltages were simulated and applied, and the residual micromotion was then canceled by slightly adjusting the DC voltages. However, the ion position could be shifted in this process, and $\omega_{z0}(z_{ion})$ could also be distorted. In the experiment, when the ion was located at the farthest point from $z_{ion} = 0$, ω_{z0} decreased by approximately 22% compared with that of $z_{ion} = 0$. By compensating for $\omega_{z0}(z_{ion})$ at each ion position, the estimated margins of error for x_q, z_q, and Q in Case 1 were reduced to 11 μm, 5 μm, and $31e$, respectively. The corrected margin of error was approximately half of what it was before the compensation. Also, the margin of error can be reduced if the measurement of secular frequency is more accurate. In the experiment, the margin of error for the secular frequency measurement was approximately 0.2 kHz, corresponding to 1.48 V/m of electric field and 0.35 μm of ion displacement in the surface-electrode ion trap. This measurement accuracy is comparable to the micromotion compensation techniques, which can detect 1−5 V/m of electric fields [50, 95]. Instead of the parametric excitation method that can accompany electrical noises, other ways, such as the resolved sideband method, may reduce the measurement error.

To evaluate the sensitivity of the proposed method for estimating the locations of stray charges, the relationship between the charge amount and the ion-stray charge distance is investigated while varying the accuracy of secular frequency measurement. The sensitivity depends on several factors, including the initial secular frequency, the ion-stray charge distance, the charge amount, and the accuracy of secular frequency measurement, as described by Eq. (2.10). In my investigation, I assume the initial secular frequency to be $2\pi \times 250$ kHz, which is the value used in the experiment, and vary the accuracy of secular frequency measurement as $2\pi \times (0.1, 0.2, 0.5)$ kHz. The results are plotted in Figure 4-31, where the x-axis represents the distance between the ion and the stray charge ranging from 0 to 500 μm, and the y-axis represents the absolute amount of charge ranging from 0 to $500e$. The lines on the graph indicate the minimum amount of charge that can be detected by the secular frequency shift under the corresponding distance and frequency measurement accuracy. For example, based on my experimental results with a 0.2 kHz accuracy, a stray charge as low as approximately $10e$ can be detected when the ion-stray charge distance is approximately 115 μm, which corresponds to the distance between the ion and the nearest electrode in our surface-electrode ion trap. On the other hand, when the charge amount is $100e$, the stray charge up to approximately 350 μm away from the ion can be observed with an accuracy of 0.2 kHz.

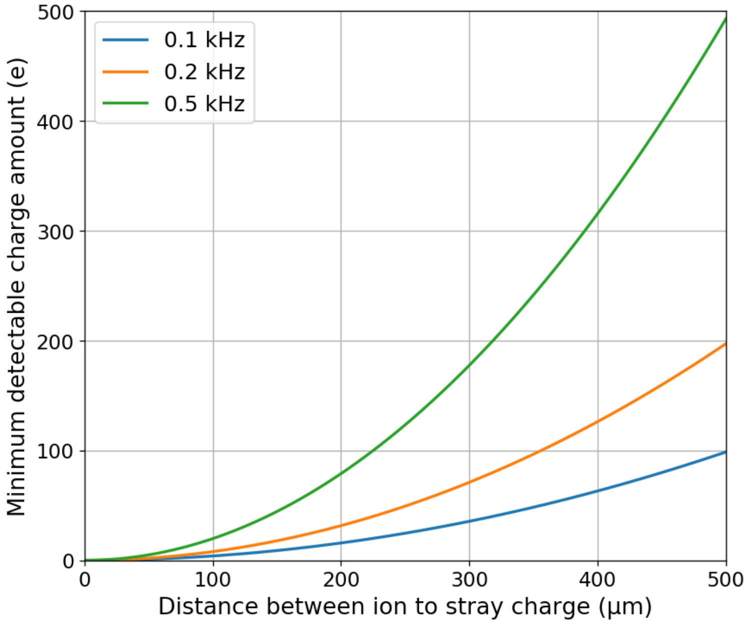

Figure 4-31. Relationship between the minimum detectable charge amount as a function of the distance between the ion and the stray charge, represented as the absolute value. The minimum detectable charge amount is plotted against the accuracy of the secular frequency measurement, indicated by the blue, orange, and green lines for accuracies of 0.1, 0.2, and 0.5 kHz, respectively.

This study assumed point charges for the simplicity of the model. However, when stray charges are induced by a laser, they can occur over an area with relatively large dimensions compared to the distance to the ion position. Also, when it is generated on top of the thin native oxide layer of the electrode material, the additional potential generated by the stray charge might behave close to that of the dipole moment rather than a point charge depending on the geometry. I confirmed that the developed method still can predict the center position of the charged area under different scenarios, even though the estimated amount of charge can vary by more than an order of magnitude. Additional details regarding this topic can be found in Appendix D.

A major disadvantage of the developed method is its relatively slow speed compared to the micromotion compensation techniques, as it involves scanning the frequency. In particular, the measurement speed is determined by the precision of the secular frequency measurement. However, this technique is still a useful tool to identify the locations of laser-induced stray charges, which can allow us to efficiently optimize the laser propagation paths to reduce the occurrence of stray charges in surface-electrode ion traps.

Chapter 5

Conclusion

In summary, this dissertation developed a method for estimating the locations of laser-induced stray charges in surface-electrode ion traps. In Chapter 2, the variation in the electric potential at the trapped ion location was modeled in the presence of a laser-induced stray charge, and the magnitude of the shift in the secular frequency of the trapped ion was derived from the model. Then, constraints were assumed to uniquely determine the location of stray charge from the secular frequency shift. In detail, it was assumed that the secular frequency could be measured at multiple ion positions in surface-electrode ion traps, and therefore the required number of secular frequency shift measurements could be performed to determine the stray charge locations uniquely. The model was then extended to the cases where stray charges occurred at multiple locations. Numerous test data were generated with the assumption of multiple stray charges at random locations, and the locations of multiple stray charges were estimated from the secular frequency shift observed in the test data. The estimated locations were then compared with the actual locations used to generate the test data. The number of stray charge locations that could be distinguished using the developed method was also analyzed in this process. When different stray charges were sufficiently far apart enough to show different secular frequency shift peaks, locations of different stray charges could be easily estimated. However, when different stray charges were located close to each other and showed a single peak, up to three charge locations could be identified. The effectiveness of the developed method was supported by simulating the effect of stray charges and by analyzing the resulting secular frequency shift in Chapter 3. The locations of multiple stray charges were estimated from the secular frequency shift observed at multiple ion positions in the simulation. Also, in Chapter 4, experiments were performed to evaluate the developed method by intentionally producing electric charges at a single location by irradiating the laser onto that spot. The resulting secular frequency shift of the trapped ion was measured at multiple ion positions, and the location of produced charges was estimated from the measurement result. The estimated location of the produced charges agreed with where the laser was irradiating within the margin of error. The developed method can be used to characterize laser-induced stray charges when trapped ions detect stray electric fields. This can be extended to designing experiments to avoid or reduce the occurrence of stray charges efficiently.

Appendix A

State Space Analysis

The developed model in Chapter 2 was also analyzed in the state space. The relationship among the secular frequency shift, laser-induced stray charges, and incident lasers is considered as an n-dimensional p-input q-output state space. The parameters can be written as

Input ($u(t)$): Lasers ($u(t) \in R^p$)

State ($x(t)$): Laser-induced stray charges ($x(t) \in R^n$)

Output ($y(t)$): Secular frequency shift ($y(t) \in R^q$)

The relationship between input, state, and output in the state space can be expressed as the following equation:

$$\dot{x}(t) = Ax(t) + Bu(t)$$

$$y(t) = Cx(t) + Du(t). \tag{A.1}$$

Assume that the stray charges at different locations are decoupled from each other, and the equation for the laser-induced charge can then be written in the form of a rate equation. The A matrix for the situation where stray charges occur at three locations can be expressed as follows:

$$A = \begin{bmatrix} -(\delta_1 + \gamma_1) & 0 & 0 \\ 0 & -(\delta_2 + \gamma_2) & 0 \\ 0 & 0 & -(\delta_3 + \gamma_3) \end{bmatrix}, \tag{A.2}$$

where δ_k and γ_k indicate δ and γ of k-th stray charge ($k = 1{,}2{,}3$). The rate of charge accumulation induced by the laser is determined by the frequency and intensity of the incident laser. According to S. X. Wang *et al.* [97], the accumulation rate is proportional to the laser frequency. Thus, the accumulation rate can be decomposed into a constant term, b, which represents the rate dependent on the laser frequency, as well as the laser intensity. Assuming a situation in which three different lasers are delivered, B matrix is expressed as follows:

$$B = \begin{bmatrix} b_{11} & b_{12} & b_{13} \\ b_{21} & b_{22} & b_{23} \\ b_{31} & b_{32} & b_{33} \end{bmatrix}. \tag{A.3}$$

Elements of C matrix are composed of polynomials for coordinates of the trapped ion and stray charges, and since x_q and z_q are free variables, the elements of C matrix are also variables. Assuming the case where three secular frequency shifts are measured, the C matrix is expressed as follows:

$$C = \begin{bmatrix} c_{11} & c_{12} & c_{13} \\ c_{21} & c_{22} & c_{23} \\ c_{31} & c_{32} & c_{33} \end{bmatrix}, \tag{A.4}$$

where $c_{ij}(i,j = 1,2,3)$ is as follows:

$$c_{ij} = \frac{K\left[\left(x_i - x_j\right)^2 + \left(y_i - y_j\right)^2 - 2\left(z_i - z_j\right)^2\right]}{\omega_{z0}(z_i)\left[\left(x_i - x_j\right)^2 + \left(y_i - y_j\right)^2 + \left(z_i - z_j\right)^2\right]^{5/2}}. \tag{A.5}$$

Considering the equation for the secular frequency shift, it is not directly affected by the laser. Thus, the D matrix can be considered a zero matrix.

The observability analysis was carried out to mathematically investigate whether different states can be distinguished. The observability matrix (Q_o) is as follows:

$$Q_o = [C^T \quad A^T C^T \quad \cdots \quad (A^T)^{n-1} C^T]. \tag{A.6}$$

When Q_o is full-rank, $|Q_o| \neq 0$, and the system is observable. Since the elements in the C matrix are different, $|Q_o| \neq 0$ and the system is observable. In other words, when the accumulation rates of separate charges are different, different amounts of charges can be distinguished through changes in the shape of the secular frequency shift peaks observed at different times, as shown in Figure A-1. However in most cases, since the measurement of secular frequency is relatively slow compared to the rate of charge accumulation, it may be challenging to distinguish different amounts of charges using the change in the shape of the secular frequency shift peak.

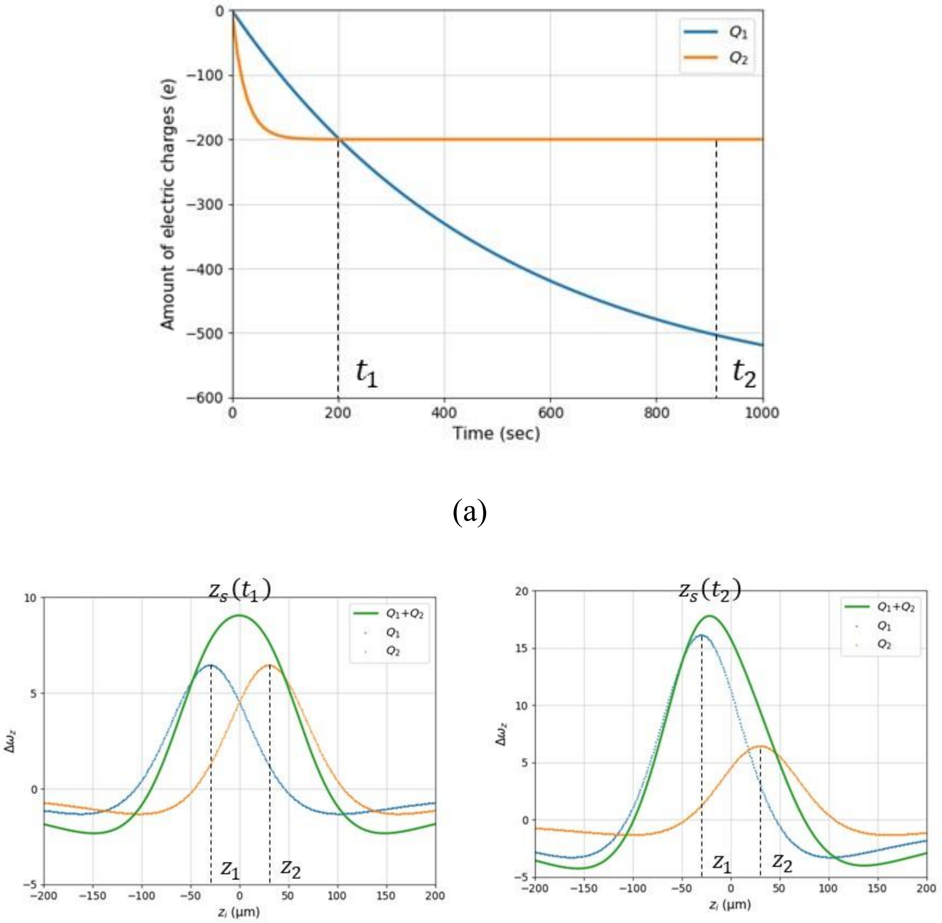

(a)

(b)

(c)

Figure A-1. The analysis result of the case when separate charges have different charging rates. (a) The plot of the charge amount as a function of time for two separate charges with different charging rates. (b) The plot of $\Delta\omega_z$ as a function of z_{ion} at t_1. The z_1, z_2, and z_s indicate the position of $\Delta\omega_z$ peak. (c) The plot of $\Delta\omega_z$ as a function of z_{ion} at t_2.

The charge amount was quantitatively calculated using the output equation. In the scenario where three charges exist and three secular frequency shifts are measured, taking the inverse matrix to calculate the charge amount could be rearranged as follows:

$$\begin{bmatrix} Q_1 \\ Q_2 \\ Q_3 \end{bmatrix} = \frac{C_s}{|C|} \begin{bmatrix} \Delta\omega_z(z_1) \\ \Delta\omega_z(z_2) \\ \Delta\omega_z(z_3) \end{bmatrix}, \tag{A.7}$$

where $\mathrm{C_s}$ and $|C|$ are

$$C_s = \begin{bmatrix} c_{22}c_{33} - c_{23}c_{32} & c_{13}c_{32} - c_{12}c_{33} & c_{12}c_{23} - c_{13}c_{22} \\ c_{23}c_{31} - c_{21}c_{33} & c_{11}c_{33} - c_{13}c_{31} & c_{13}c_{21} - c_{11}c_{23} \\ c_{21}c_{32} - c_{22}c_{31} & c_{12}c_{31} - c_{11}c_{32} & c_{11}c_{22} - c_{12}c_{21} \end{bmatrix}, \tag{A.8}$$

and

$$\begin{aligned} |C| = {} & c_{11}c_{22}c_{33} - c_{11}c_{23}c_{32} + c_{12}c_{21}c_{33} - c_{12}c_{23}c_{31} \\ & + c_{13}c_{21}c_{32} - c_{13}c_{22}c_{31}. \end{aligned} \tag{A.9}$$

For instance, the calculation result for Q_1 can be summarized as follows:

$$\begin{aligned} Q_1 = \frac{1}{|C|} [& (c_{22}c_{33} - c_{23}c_{32})\Delta\omega_z(z_1) \\ & + (c_{13}c_{32} - c_{12}c_{33})\Delta\omega_z(z_2) \\ & + (c_{12}c_{23} - c_{13}c_{22})\Delta\omega_z(z_3)]. \end{aligned} \tag{A.10}$$

The c_{ij} was variable, and therefore it was challenging to analytically find the solution using Eq. (A.7). Thus, the least square method (curve fitting) was used to estimate x_q and z_q in Chapter 4, the location of charges, including the amount of charges.

Appendix B

Analysis of Charge Dissipation Rate

In the process of measuring the secular frequency shift caused by the 398.9-nm laser, the secular frequency returned to its initial value (ω_{z0}) within 1 minute when the injection of the 398.9-nm laser was blocked, as shown in Figure 4-24. However, when the charge was induced using a 369.5-nm laser, the secular frequency did not return to ω_{z0} for more than 20 minutes after blocking the laser irradiation, as shown in Figure B-1. The fluorescence of the trapped ion could not be distinguished from the reflected light while shining the 369.5-nm laser on the trap surface, and therefore the secular frequency could not be measured in the gray box.

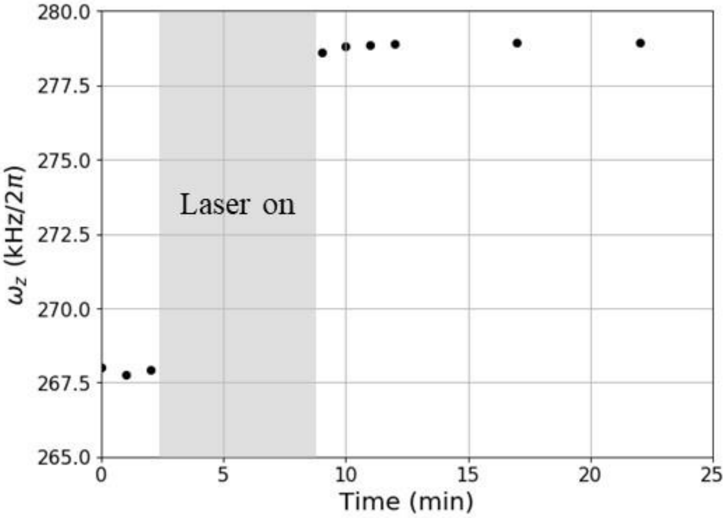

Figure B-1. The measurement result of secular frequency with the 369.5-nm laser. The gray box indicates the time while irradiating the electrode surface with the laser. Due to the reflected light from the electrode surface, the secular frequency cannot be obtained in the gray box.

When irradiating the trap surface with the 398.9-nm laser, photoelectrons emitted from the interface between the metal and oxide layers seemed to be trapped close to the oxide interface, and therefore when the laser irradiation was blocked, accumulated charges appear to be rapidly dissipated along the metal and oxide interface. However, when the 369.5-nm laser was irradiating, the kinetic energy of photoelectrons may have been higher than that of the 398.9-nm laser (the energy of 369.5 nm is approximately 3.36 eV, whereas that of 398.9 nm is approximately 3.11 eV), and therefore they seemed to be trapped deep inside the native oxide layer, resulting in a low dissipation rate. Thus, it could be concluded that the dissipation rate was also affected by the incident laser frequency.

Appendix C

Ion Position Changes

The DC voltages were numerically simulated in which the initial secular frequency (ω_{z0}) and ion height were uniform even when the ion moved along the z-axis using Eqs. (3.2) and (3.3). A total of eight pairs of DC electrodes were used in the process of changing the ion position, and as a result, the DC voltage that could change the ion position by approximately 39 μm while the ion height changed by less than 70 nm was derived. The change in ω_{z0} was within 3.5% considering all of the x', y', and z axes.

The z_{ion} was varied by applying the calculated DC voltage set. Figure C-1(a) shows the measurement result of ion position changes in the range from −117 to +117 μm by approximately 39 μm along the z-direction. The expected z_{ion} indicates the position where the trapped ion is expected to be located based on the calculation result, and measured z_{ion} is the estimated value that trapped the ion is positioned with respect to the initial ion position in the CCD. As shown in Figure C-1(a), z_{ion} was changed by approximately 20 μm. The RF voltage may be coupled to a DC electrode, and then induce a stray electric field in the z-direction. As a first proof, in principle, the surface-electrode ion trap used in the experiment cannot hold charged particles only using the RF voltage, since it cannot build a potential well in the z-axis unless DC voltages are applied. However, it was possible to confine ions by only applying the RF voltage. In addition, there was a difference of approximately 20.4(3) μm between the ion position without applying DC voltages and the position where the ion was confined when DC voltages were applied symmetrically. Therefore, it could be concluded that the change of z_{ion} was different from the calculation results, due to the presence of an RF stray field in the z-axis.

Figure C-1(b) shows the measurement result of the initial secular frequency at each z_{ion}. The initial secular frequency was different between the measurement result and the calculated value, probably due to the effect of the RF stray field. The blue dot indicates the measurement result, and the orange dot represents the calculation result. When z_{ion} was in the range from −20 to +20 μm, $\omega_{z0}(z_{ion})$ was measured to be the largest at approximately $2\pi \times 340$ kHz, and $\omega_{z0}(z_{ion})$ decreased as the ion moved away from the initial ion position. For this reason, it was considered that an error occurred in the process of estimating the location of the stray charge using the secular frequency shift at multiple ion positions, as mentioned in Section 4-4.

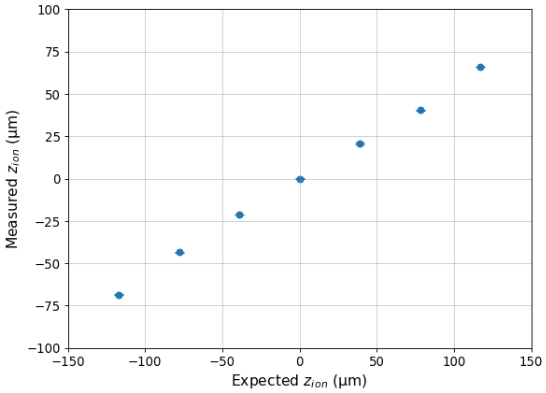

(a)

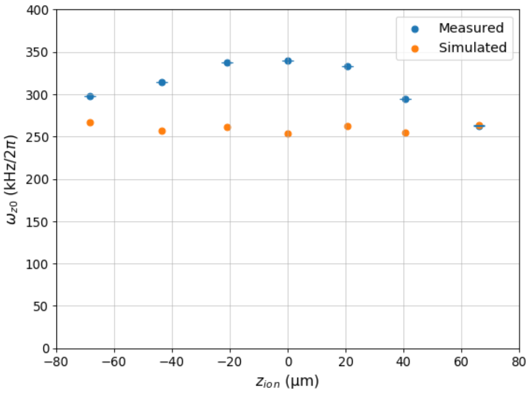

(b)

Figure C-1. Actual ion positions and initial secular frequency at different z_{ion}. (a) Actual ion positions with respect to the expected ion positions. The expected ion positions are the simulation results. (b) The measurement result of initial secular frequency at each ion position.

Appendix D

Dipole Model

When establishing the theoretical model, it was assumed that there is a point charge in free space, as was discussed at the end of Section IV. C. However, to demonstrate the practicality of the developed model even under other scenarios, a uniform charge density was assigned to an area of 10 μm × 10 μm in the simulation, and the secular frequency shift in the simulation and the charge amount estimated from the theoretical model were then analyzed. Similar to the simulation condition in Figure D-1(a), a surface charge density of $-10e/\mu\mathrm{m}^2$ was applied to create a total charge of $-1000e$, and the center position of the charged area was assumed to be (55, −108, 0) μm. The material beneath the induced charging area was assumed to be alumina (Al_2O_3), a native oxide film on an aluminum electrode, while the electrode itself was assumed to be grounded. The secular frequency shift was estimated by varying the distance between the ion and the charged region at intervals of 40 μm in the range of −240~+240 μm in the z-axis. As shown in Figure D-1(a), the magnitude of the secular frequency shift decreased by approximately 35 times, and the estimated charge amount obtained through curve fitting also decreased by approximately 36 times resulting in a value of $-27e$. However, the estimated charge location was $(x_q, z_q) = (60, 0)$ μm, which is comparable to the result obtained using a point charge within a 7% error.

As depicted in Figure D-1(b) and (c), similar simulations were conducted by changing the area and the material underneath the induced surface charge density. The total amount of charge was set to be $-1000e$ for all cases, and the corresponding results were summarized in Table D-1. Although the area and the material were different, a similar shape of the plot was observed, and then all the estimated location of stray charge was comparable. However, the estimated total charge amount had a large discrepancy depending on the area and the material. Different dielectric constants might lead to different magnitudes of the electric field inside the insulating film, resulting in different electric field gradients at the ion position. Also, a larger area resulted in a less electric field gradient at the ion position, leading to a less secular frequency shift, when the total charge amount was constant. Note that the main purpose of this study is to identify the location of the stray charges, and to extend this approach to estimate the relatively accurate amount of stray charges as well, more elaborate model and information about the layer structure will be required.

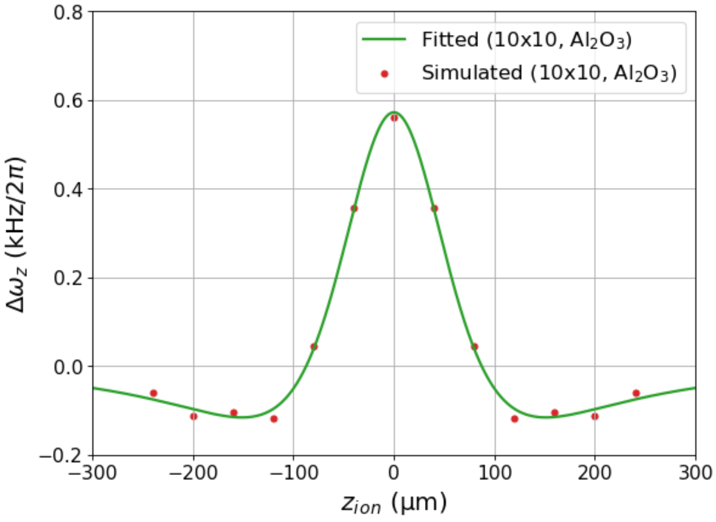

(a)

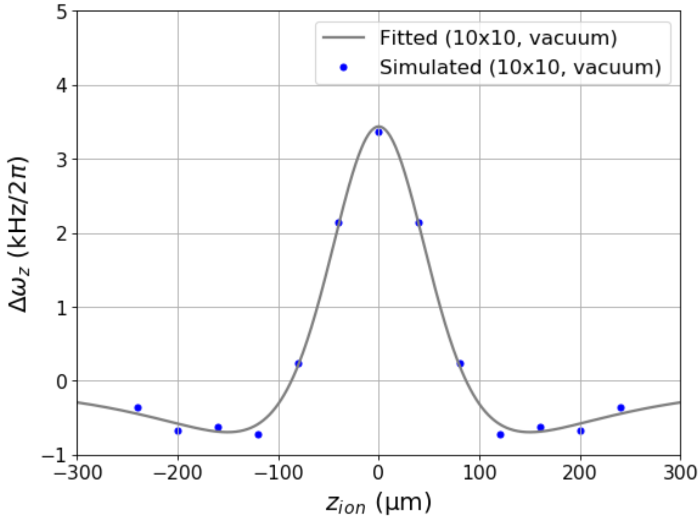

(b)

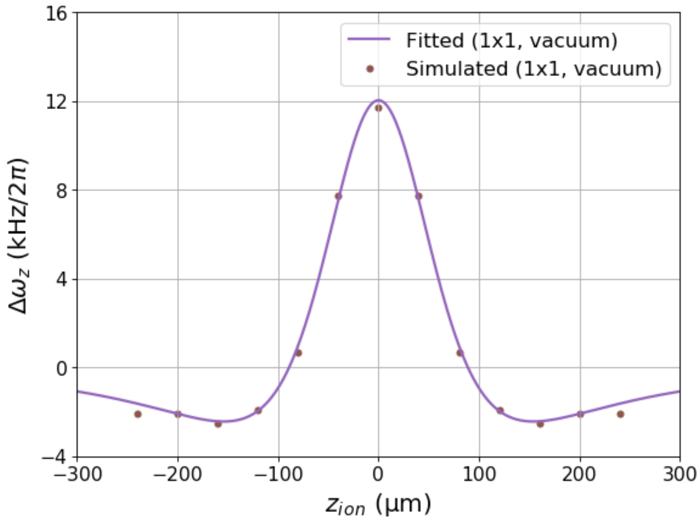

(c)

Figure D-1. Curve fitting and simulation results of $\Delta\omega_z$ as a function of z_{ion}. (a) A surface charge density of $-10e$/μm^2 on an alumina area of 10 μm × 10 μm. (b) A charge density of $-10e$/μm^2 on an area of 10 μm × 10 μm in a vacuum. (c) A charge density of $-1000e$/μm^2 on an area of 1 μm × 1 μm in a vacuum. The corresponding fitting results are summarized in Table D-1.

Table D-1. Summary of curve fitting results, shown in Figure D-1. The 10×10 and 1×1 indicate the sizes of charged regions in μm^2, and the point represents a point charge. The surface charge density (ρ_s) denotes the magnitude of assigned charge density at the charged regions. The estimated location of the charge is indicated by (x_q, z_q), and the estimated amount of charge is represented by Q. For all simulation results, the total charge amount is assumed to be $-1000e$, and y_q is assumed to be −108 μm.

Simulation condition	ρ_s (e/μm^2)	(x_q, z_q) (μm)	Q (e)
10×10 (Al_2O_3)	−10	(60, 0)	−27
10×10 (vacuum)	−10	(58, 0)	−159
1×1 (vacuum)	−1000	(63, 0)	−583
Point (vacuum)	–	(64, 0)	−653

References

[1] D. P. DiVincenzo, “The physical implementation of quantum computation,” *Fortschritte der Physik: Progress of Physics*, vol. 48, no. 9, pp. 771-783 (2000).

[2] S. Paesani, J. F. F. Bulmer, A. E. Jones, R. Santagati, and A. Laing, “Scheme for universal high-dimensional quantum computation with linear optics,” *Physical Review Letters*, vol. 126, no. 23, pp. 230504 (2021).

[3] L. Childress and R. Hanson, “Diamond NV centers for quantum computing and quantum networks,” *MRS Bulletin*, vol. 38, no. 2, pp. 134-138 (2013).

[4] J. M. Gambetta, J. M. Chow, and M. Steffen, “Building logical qubits in a superconducting quantum computing system,” *npj Quantum Information*, vol. 3, no. 1, pp. 1-7 (2017).

[5] L. Henriet, L. Beguin, A. Signoles, T. Lahaye, A. Browaeys, G. O. Reymond, and C. Jurczak, “Quantum computing with neutral atoms,” *Quantum*, vol. 4, pp. 327 (2020).

[6] C. D. Bruzewicz, J. Chiaverini, R. McConnell, and J. M. Sage, “Trapped-ion quantum computing: Progress and challenges,” *Applied*

Physics Reviews, vol. 6, no. 2, pp. 021314 (2019).

[7] H. C. Nagerl, D. Leibfried, H. Rohde, G. Thalhammer, J. Eschner, F. Schmidt-Kaler, and R. Blatt, "Laser addressing of individual ions in a linear ion trap," *Physical Review A*, vol. 60, no. 1, pp. 145 (1999).

[8] U. Warring, C. Ospelkaus, Y. Colombe, R. Jordens, D. Leibfried, and D. J. Wineland, "Individual-ion addressing with microwave field gradients," *Physical Review Letters*, vol. 110, no. 17, pp. 173002 (2013).

[9] Y. Wang, M. Um, J. Zhang, S. An, M. Lyu, J. N. Zhang, L. M. Duan, D. Yum, and K. Kim, "Single-qubit quantum memory exceeding ten-minute coherence time," *Nature Photonics*, vol. 11, no. 10, pp. 646-650 (2017).

[10] N. Grzesiak, R. Blumel, K. Wright, K. M. Beck, N. C. Pisenti, M. Li, V. Chaplin, J. M. Amini, S. Debnath, J. S. Chen, and Y. Nam, "Efficient arbitrary simultaneously entangling gates on a trapped-ion quantum computer," *Nature Communications*, vol. 11, no. 1, pp. 2963 (2020).

[11] R. E. March, "An introduction to quadrupole ion trap mass spectrometry," *Journal of Mass Spectrometry*, vol. 32, no. 4, pp. 351-369 (1997).

[12] H. Haffner, C. F. Roos, and R. Blatt, "Quantum computing with trapped

ions," *Physics Reports*, vol. 469, no. 4, pp. 155-203 (2008).

[13] R. Blatt and C. F. Roos, "Quantum simulations with trapped ions," *Nature Physics*, vol. 8, no. 4, pp. 277-284 (2012).

[14] Y. H. Teoh, M. Drygala, R. G. Melko, and R. Islam, "Machine learning design of a trapped-ion quantum spin simulator," *Quantum Science and Technology*, vol. 5, no. 2, pp. 024001 (2020).

[15] W. Paul, "Electromagnetic traps for charged and neutral particles," *Review of Modern Physics*, vol. 62, no. 3, pp. 531 (1990).

[16] H. Dehmelt, "A single atomic particle forever floating at rest in free space: New value for electron radius," *Physica Scripta*, vol. 1988, no. T22, pp. 102-110 (1988).

[17] K. Wright, *et al.*, "Benchmarking an 11-qubit quantum computer," *Nature Communications*, vol. 10, no. 1, pp. 5464 (2019).

[18] S. Jain, J. Alonso, M. Grau, and J. P. Home, "Scalable arrays of micro-penning traps for quantum computing and simulation," *Physical Review X*, vol. 10, no. 3, pp. 031027 (2020).

[19] T. Monz, P. Schindler, J. T. Barreiro, M. Chwalla, D. Nigg, W. A. Coish, M. Harlander, W. Hansel, M. Hennrich, and R. Blatt, "14-qubit entanglement: Creation and coherence," *Physical Review Letters*, vol.

106, no. 13, pp. 130506 (2011).

[20] D. R. Leibrandt, R. J. Clark, J. Labaziewicz, P. Antohi, W. Bakr, K. R. Brown, and I. L. Chuang, “Laser ablation loading of a surface-electrode ion trap,” *Physical Review A*, vol. 76, no. 5, pp. 055403 (2007).

[21] C. Chen and K. Gao, “A scheme for physical implementation of a ququadrit quantum computation with cooled-trapped ions,” *International Journal of Theoretical Physics*, vol. 44, no. 8, pp. 1177-1191 (2005).

[22] B. Hemmerling, F. Gebert, Y. Wan, D. Nigg, I. V. Sherstov, and P. O. Schmidt, “A single laser system for ground-state cooling of $^{25}\mathrm{Mg}^{+}$,” *Applied Physics B*, vol. 104, no. 3, pp. 583-590 (2011).

[23] G. Kirchmair, J. Benhelm, F. Zahringer, R. Gerritsma, C. F. Roos, and R. Blatt, “High-fidelity entanglement of $^{43}\mathrm{Ca}^{+}$ hyperfine clock states,” *Physical Review A*, vol. 79, no. 2, pp. 020304 (2009).

[24] P. J. Low, B. M. White, A. A. Cox, M. L. Day, and C. Senko, “Practical trapped-ion protocols for universal qudit-based quantum computing,” *Physical Review Research*, vol. 2, no. 3, pp. 033128 (2020).

[25] S. Olmschenk, K. C. Younge, D. L. Moehring, D. N. Matsukevich, P. Maunz, and C. Monroe, “Manipulation and detection of a trapped Yb^{+}

hyperfine qubit," *Physical Review A*, vol. 76, no. 5, pp. 052314 (2007).

[26] P. Wang, C. Y. Luan, M. Qiao, M. Um, J. Zhang, Y. Wang, X. Yuan, M. Gu, J. Zhang, and K. Kim, "Single ion qubit with estimated coherence time exceeding one hour," *Nature Communications*, vol. 12, no. 1, pp. 233 (2021).

[27] D. Cho, S. Hong, M. Lee, and T. Kim, "A review of silicon microfabricated ion traps for quantum information processing," *Micro and Nano Systems Letters*, vol. 3, no. 2, pp. 1-12 (2015).

[28] J. N. Louris, R. G. Cooks, J. E. P. Syka, P. E. Kelly, G. C. Stafford Jr, and J. F. J. Todd, "Instrumentation, applications, and energy deposition in quadrupole ion-trap tandem mass spectrometry," *Analytical Chemistry*, vol. 59, no. 13, pp. 1677-1685 (1987).

[29] R. E. Kaiser Jr, R. G. Cooks, G. C. Stafford Jr, J. E. P. Syka, and P. H. Hemberger, "Operation of a quadrupole ion trap mas spectrometer to achieve high mass/charge ratios," *International Journal of Mass Spectrometry and Ion Processes*, vol. 106, pp. 79-115 (1991).

[30] J. D. Prestage, G. J. Dick, and L. Maleki, "New ion trap for frequency standard applications," *Journal of Applied Physics*, vol. 66, no. 3, pp. 1013-1017 (1989).

[31] M. G. Raizen, J. M. Gilligan, J. C. Bergquist, W. M. Itano, and D. J. Wineland, “Ionic crystals in a linear Paul trap,” *Physical Review A*, vol. 45, no. 9, pp. 6493 (1992).

[32] Webpage of Institut für Quantenoptik und Quanteninformation at Innsbruck [http://heart-c704.uibk.ac.at/index.php/en/research/lintrap]

[33] M. E. Poitzsch, J. C. Bergquist, W. M. Itano, and D. J. Wineland, “Cryogenic linear ion trap for accurate spectroscopy,” *Review of Scientific Instruments*, vol. 67, no. 1, pp. 129-134 (1996).

[34] G. Huber, T. Deuschle, W. Schnitzler, R. Reichle, K. Singer, and F. Schmidt-Kaler, “Transport of ions in a segmented linear Paul trap in printed-circuit-board technology,” *New Journal of Physics*, vol. 10, no. 1, pp. 013004 (2008).

[35] E. Brama, A. Mortensen, M. Keller, and W. Lange, “Heating rates in a thin ion trap for microcavity experiments,” *Applied Physics B*, vol. 107, no. 7, pp. 945-954 (2012).

[36] J. I. Cirac and P. Zoller, “A scalable quantum computer with ions an array of microtraps,” *Nature*, vol. 404, no. 6778, pp. 579-581 (2000).

[37] D. Kielpinski, C. Monroe, and D. J. Wineland, “Architecture for a large-scale ion-trap quantum computer,” *Nature*, vol. 417, no. 6890, pp. 709-

711 (2002).

[38] S. Hong, M. Lee, H. Cheon, T. Kim, and D. Cho, “Guidelines for designing surface ion traps using the boundary element method,” *Sensors*, vol. 16, no. 5, pp. 616 (2016).

[39] P. L. W. Maunz, “High optical access trap 2.0,” Report SAND2016-0796R (Sandia National Laboratories, 2016).

[40] S. Auchter, *et al.*, “Industrially microfabricated ion trap with 1 eV trap depth,” *Quantum Science and Technology*, vol. 7, no. 3, pp. 035015 (2022).

[41] S. Debnath, N. M. Linke, C. Figgatt, K. A. Landsman, K. Wright, and C. Monroe, “Demonstration of a small programmable quantum computer with atomic qubits,” *Nature*, vol. 536, no. 7614, pp. 63-66 (2016).

[42] N. H. Nguyen, M. Li, A. M. Green, C. H. Alderete, Y. Zhu, D. Zhu, K. R. Brown, and N. M. Linke, “Demonstration of Shor encoding on a trapped-ion quantum computer,” *Physical Review Applied*, vol. 16, no. 2, pp. 024057 (2021).

[43] R. B. Blakestad, C. Ospelkaus, A. P. VanDevender, J. M. Amini, J. Britton, D. Leibfried, and D. J. Wineland, “High-fidelity transport of

trapped-ion qubits through an X-junction trap array," *Physical Review Letters*, vol. 102, no. 15, pp. 153002 (2009).

[44] B. Lekitsch, S. Weidt, A. G. Fowler, K. Molmer, S. J. Devitt, C. Wunderlich, and W. K. Hensinger, "Blueprint for a microwave trapped ion quantum computer," *Science Advances*, vol. 3, no. 2, e1601540 (2017).

[45] A. Bautista-Salvador, G. Zarantonello, H. Hahn, A. Preciado-Grijalva, J. Morgner, M. Wahnschaffe, and C. Ospelkaus, "Multilayer ion trap technology for scalable quantum computing and quantum simulation," *New Journal of Physics*, vol. 21, no. 4, pp. 043001 (2019).

[46] M. Niedermayr, K. Lakhmanskiy, M. Kumph, S. Partel, J. Edlinger, M. Brownnutt, and R. Blatt, "Cryogenic surface ion trap based on intrinsic silicon," *New Journal of Physics*, vol. 16, no. 11, pp. 113068 (2014).

[47] N. D. Guise, *et al.*, "Ball-grid array architecture for microfabricated ion traps," *Journal of Applied Physics*, vol. 117, no. 17, pp. 174901 (2015).

[48] M. C. Revelle, "Phoenix and Peregrine ion traps," *arXiv preprint arXiv: 2009.02398* (2020).

[49] D. Stick, W. K. Hensinger, S. Olmschenk, M. J. Madsen, K. Schwab, and C. Monroe, "Ion trap in a semiconductor chip," *Nature Physics*, vol.

2, no. 1, pp. 36-39 (2006).

[50] D. T. C. Allcock, J. A. Sherman, D. N. Stacey, A. H. Burrell, M. J. Curtis, G. Imreh, N. M. Linke, D. J. Szwer, S. C. Webster, A. M. Steane, and D. M. Lucas, "Implementation of a symmetric surface-electrode ion trap with field compensation using a modulated Raman effect," *New Journal of Physics*, vol. 12, no. 5, pp. 053026 (2010).

[51] A. V. Rynbah, P. Maunz, and J. Kim, "An integrated mirror and surface-electrode ion trap with a tunable trap location," *Applied Physics Letters*, vol. 109, no. 22, pp. 221108 (2016).

[52] U. Tanaka, K. Suzuki, Y. Ibaraki, and S. Urabe, "Design of a surface electrode trap for parallel ion strings," *Journal of Physics B: Atomic, Molecular and Optical Physics*, vol. 47, no. 3, pp. 035301 (2014).

[53] J. A. Sedlacek, A. Greene, J. Stuart, R. McConnell, C. D. Bruzewicz, J. M. Sage, and J. Chiaverini, "Distance scaling of electric-field noise in a surface-electrode ion trap," *Physical Review A*, vol. 97, no. 2, pp. 020302 (2018).

[54] W. K. Hensinger, S. Olmschenk, D. Stick, D. Hucul, M. Yeo, M. Acton, L. Deslauriers, and C. Monroe, "T-junction ion trap array for two-dimensional ion shuttling, storage, and manipulation," *Applied Physics*

Letters, vol. 88, no. 3, pp. 034101 (2006).

[55] G. Huber, T. Deuschle, W. Schnitzler, R. Reichle, K. Singer, and F. Schmidt-Kaler, "Transport of ions in a segmented linear Paul trap in printed-circuit-board technology," *New Journal of Physics*, vol. 10, no. 1, pp. 013004 (2008).

[56] V. Kaushal, B. Lekitsch, A. Stahl, J. Hilder, D. Pijn, C. Schmiegelow, A. Bermudez, M. Muller, F. Schmidt-Kaler, and U. Poschinger, "Shuttling-based trapped-ion quantum information processing," *AVS Quantum Science*, vol. 2, no. 1, pp. 014101 (2020).

[57] M. Lee, J. Jeong, Y. Park, C. Jung, T. Kim, and D. Cho, "Ion shuttling method for long-range shuttling of trapped ions in MEMS-fabricated ion traps," *Japanese Journal of Applied Physics*, vol. 60, no. 2, pp. 027004 (2021).

[58] L. Deslauriers, S. Olmschenk, D. Stick, W. K. Hensinger, J. Sterk, and C. Monroe, "Scaling and suppression of anomalous heating in ion traps," *Physical Review Letters*, vol. 97, no. 10, pp. 103007 (2006).

[59] I. A. Boldin, A. Kraft, and C. Wunderlich, "Measuring anomalous heating in a planar ion trap with variable ion-surface separation," *Physical Review Letters*, vol. 120, no. 2, pp. 023201 (2018).

[60] M. Teller, D. A. Fioretto, P. C. Holz, P. Schindler, V. Messerer, K. Schuppert, Y. Zou, R. Blatt, J. Chiaverini, J. Sage, and T. E. Northup, “Heating of a trapped ion induced by dielectric materials,” *Physical Review Letters*, vol. 126, no. 23, pp. 230505 (2021).

[61] M. Brownnutt, M. Kumph, P. Rabl, and R. Blatt, “Ion-trap measurements of electric-field noise near surfaces,” *Reviews of Modern Physics*, vol. 87, no. 4, pp. 1419 (2015).

[62] M. Harlander, M. Brownnutt, W. Hansel, and R. Blatt, “Trapped-ion probing of light-induced charging effects on dielectrics,” *New Journal of Physics*, vol. 12, no. 9, pp. 093035 (2010).

[63] S. Seidelin, *et al.*, “Microfabricated surface-electrode ion trap for scalable quantum information processing,” *Physical Review Letters*, vol. 96, no. 25, pp. 253003 (2006).

[64] J. H. Wesenberg, “Electrostatics of surface-electrode ion traps,” *Physical Review A*, vol. 78, no. 6, pp. 063410 (2008).

[65] R. C. Sterling, M. D. Hughes, C. J. Mellor, and W. K. Hensinger, “Increased surface flashover voltage in microfabricated devices,” *Applied Physics Letters*, vol. 103, no. 14, pp. 143504 (2013).

[66] R. C. Sterling, H. Rattanasonti, S. Weidt, K. Lake, P. Srinivasan, S. C.

Webster, M. Kraft, and W. K. Hensinger, “Fabrication and operation of a two-dimensional ion-trap lattice on a high-voltage microchip,” *Nature Communications*, vol. 5, no. 1, pp. 3637 (2014).

[67] D. Stick, K. M. Fortier, R. Haltli, C. Highstrete, D. L. Moehring, C. Tigges, and M. G. Blain, “Demonstration of a microfabricated surface electrode ion trap,” *arXiv preprint arXiv: 1008.0990* (2010).

[68] S. Hong, Y. Kwon, C. Jung, M. Lee, T. Kim, and D. Cho, “A new microfabrication method for ion-trap chips to reduce exposed dielectric surfaces from trapped ions,” *IEEE Journal of Microelectromechanical Systems*, vol. 27, no. 1, pp. 28-30 (2018).

[69] C. Jung, W. Lee, J. Jeong, M. Lee, Y. Park, T. Kim, and D. Cho, “A microfabricated ion trap chip with a sloped loading slot to minimize exposing trapped ions to stray charges,” *Quantum Science and Technology*, vol. 6, no. 4, pp. 044004 (2021).

[70] 이민재,"확장 가능한 평면 이온트랩 어레이 구현을 위한 설계 및 셔틀링 기술," *Ph.D. dissertation, Seoul National University* (2021).

[71] P. C. Holz, S. Auchter, G. Stocker, M. Valentini, K. Lakhmanskiy, C.

Rossler, P. Stampfer, S. Sgouridis, E. Aschauer, Y. Colombe, and R. Blatt, “2D linear trap array for quantum information processing,” *Advanced Quantum Technologies*, vol. 3, no. 11, pp. 2000031 (2020).

[72] J. M. Pino, *et al.*, “Demonstration of the QCCD trapped-ion quantum computer architecture,” *Nature*, vol. 592, no. 7853, pp. 209-213 (2021).

[73] C. Monroe, R. Raussendorf, A. Ruthven, K. R. Brown, P. Maunz, L. -M. Duan, and J. Kim, “Large-scale modular quantum-computer architecture with atomic memory and photonic interconnects,” *Physical Review A*, vol. 89, no. 2, pp. 022317 (2014).

[74] D. Hucul, I. V. Inlek, G. Vittorini, C. Crocker, S. Debnath, S. M. Clark, and C. Monroe, “Modular entanglement of atomic qubits using photons and phonons,” *Nature Physics*, vol. 11, no. 1, pp. 37-42 (2015).

[75] J. Kim, J. Jeong, C. Jung, M. Lee, Y. Park, D. Cho, and T. Kim, “Observation of Hong-Ou-Mandel interference with scalable Yb^+-photon interfaces,” *Optics Express*, vol. 28, no. 26, pp. 39727-39738 (2020).

[76] Z. D. Romaszko, S. Hong, M. Siegele, R. K. Puddy, F. R. Lebrun-Gallagher, S. Weidt, and W. K. Hensinger, “Engineering of microfabricated ion traps and integration of advanced on-chip features,”

Nature Reviews Physics, vol. 2, no. 6, pp. 285-299 (2020).

[77] M. Johnning, A. Braun, N. Timoney, V. Elman, W. Neuhauser, and C. Wunderlich, “Individual addressing of trapped ions and coupling of motional and spin states using rf radiation,” *Physical Review Letters*, vol. 102, no. 7, pp. 073004 (2009).

[78] J. Pachos and H. Walther, “Quantum computation with trapped ions in an optical cavity,” *Physical Review Letters*, vol. 89, no. 18, pp. 187903 (2002).

[79] J. D. Sterk, L. Luo, T. A. Manning, P. Maunz, and C. Monroe, “Photon collection from a trapped ion-cavity system,” *Physical Review A*, vol. 85, no. 6, pp. 062308 (2012).

[80] M. Lee, M. Lee, S. Hong, K. Schuppert, Y. Kwon, T. Kim, Y. Colombe, T. E. Northup, D. Cho, and R. Blatt, “Microelectromechanical-system-based design of a high-finesse fiber cavity integrated with an ion trap,” *Physical Review Applied*, vol. 12, no. 4, pp. 044052 (2019).

[81] F. R. Ong, *et al.*, “Probing surface charge density on optical fibers with a trapped ion,” *New Journal of Physics*, vol. 22, no. 6, pp. 063018 (2020).

[82] A. P. VanDevender, Y. Colombe, Y. Amini, D. Leibfried, and D. J.

Wineland, “Efficient fiber optic detection of trapped ion fluorescence,” *Physical Review Letters*, vol. 105, no. 2, pp. 023001 (2010).

[83] T. H. Kim, P. F. Herskind, and I. L. Chuang, “Surface-electrode ion trap with integrated light source,” *Applied Physics Letters*, vol. 98, no. 21, pp. 214103 (2011).

[84] G. R. Brady, *et al.*, “Integration of fluorescence collection optics with a microfabricated surface electrode ion trap,” *Applied Physics B*, vol. 103, no. 7, pp. 801-808 (2011).

[85] K. K. Mehta, C. D. Bruzewicz, R. McConnell, R. J. Ram, J. M. Sage, and J. Chiaverini, “Integrated optical addressing of an ion qubit,” *Nature Nanotechnology*, vol. 11, no. 12, pp. 1066-1070 (2016).

[86] K. K. Mehta and R. J. Ram, “Precise and diffraction-limited waveguide-to-free-space focusing gratings,” *Scientific Reports*, vol. 7, no. 1, pp. 2019 (2017).

[87] K. K. Mehta, C. Zhang, M. Malinowski, T. L. Nguyen, M. Stadler, and J. P. Home, “Integrated optical multi-ion quantum logic,” *Nature*, vol. 586, no. 7830, pp. 533-537 (2020).

[88] D. T. C. Allcock, *et al.*, “Heating rate and electrode charging measurements in a scalable, microfabricated, surface-electrode ion trap,”

Applied Physics B, vol. 107, no. 12, pp. 913-919 (2012).

[89] Y. Kawai, K. Shimizu, A. Noguchi, S. Urabe, and U. Tanaka, "Surface-electrode trap with an integrated permanent magnet for generating a magnetic-field gradient at trapped ions," *Journal of Physics B: Atomic, Molecular, and Optical Physics*, vol. 50, no. 2, pp. 025501 (2016).

[90] M. Carsjens, M. Kohnen, T. Dubielzig, and C. Ospelkaus, "Surface-electrode Paul trap with optimized near-field microwave control," *Applied Physics B*, vol. 114, no. 12, pp. 243-250 (2014).

[91] R. Srinivas, S. C. Burd, R. T. Sutherland, A. C. Wilson, D. J. Wineland, D. Leibfried, D. T. C. Allcock, and D. H. Slichter, "Trapped-ion spin-motion coupling with microwaves and a near-motional oscillating magnetic field gradient," *Physical Review Letters*, vol. 122, no. 16, pp. 163201 (2019).

[92] J. Welzel, F. Stopp, and F. Schmidt-Kaler, "Spin and motion dynamics with zigzag ion crystals in transverse magnetic gradients," *Journal of Physics B: Atomic, Molecular, and Optical Physics*, vol. 52, no. 2, pp. 025301 (2019).

[93] M. Siegele-Brown, S. Hong, F. R. Lebrun-Gallagher, S. J. Hile, S. Weidt, and W. K. Hensinger, "Fabrication of surface ion traps with integrated

current carrying wires enabling high magnetic field gradients," *Quantum Science and Technology*, vol. 7, no. 3, pp. 034003 (2022).

[94] C. Decaroli, R. Matt, R. Oswald, C. Axline, M. Ernzer, J. Flannery, S. Ragg, and J. P. Home, "Design, fabrication and characterization of a micro-fabricated stacked-wafer segmented ion trap with two X-junctions," *Quantum Science and Technology*, vol. 6, no. 4, pp. 044001 (2021).

[95] S. Narayanan, N. Daniilidis, S. A. Moller, R. Clark, F. Ziesel, K. Singer, F. Schimidt-Kaler, and H. Haffner, "Electric field compensation and sensing with a single ion in a planar trap," *Journal of Applied Physics*, vol. 110, no. 11, pp. 114909 (2011).

[96] S. C. Doret, J. M. Amini, K. Wright, C. Volin, T. Killian, A. Ozakin, D. Denson, H. Hayden, C-S. Pai, R. E. Slusher, and A. W. Harter, "Controlling trapping potentials and stray electric fields in a microfabricated ion trap through design and compensation," *New Journal of Physics*, vol. 14, no. 7, pp. 073012 (2012).

[97] S. X. Wang, G. H. Low, N. S. Lachenmyer, Y. Ge, P. F. Herskind, and I. L. Chuang, "Laser-induced charging of microfabricated ion traps," *Journal of Applied Physics*, vol. 110, no. 10, pp. 104901 (2011).

[98] A. Harter, A. Krukow, A. Brunner, and J. H. Denschlag, "Long-term drifts of stray electric fields in a Paul trap," *Applied Physics B*, vol. 114, no. 12, pp. 275-281 (2014).

[99] N. P. de Leon, K. M. Itoh, D. Kim, K. K. Mehta, T. E. Northup, H. Paik, B. S. Palmer, N. Samarth, S. Sangtawesin, and D. W. Steuerman, "Materials challenges and opportunities for quantum computing hardware," *Science*, vol. 372, no. 6539, pp. eabb2823 (2021).

[100] S. Hong, M. Lee, Y. Kwon, D. Cho, and T. Kim, "Experimental methods for trapping ions using microfabricated surface ion traps," *Journal of Visualized Experiments*, vol. 126, pp. e56060 (2017).

[101] C. Jung, J. Jeong, S. Yoo, T. Kim, and D. Cho, "Method for estimating locations of laser-induced stray charges on surface-electrode ion traps using secular frequency shift at multiple ion positions," *Physical Review Applied*, vol. 20, no. 1, pp. 014032 (2023).

[102] D. Leibfried, R. Blatt, C. Monroe, and D. J. Wineland, "Quantum dynamics of single trapped ions," *Reviews of Modern Physics*, vol. 75, no. 1, pp. 281-323 (2003).

[103] P. Virtanen, *et al.*, "SciPy 1.0: fundamental algorithms for scientific computing in Python," *Nature Methods*, vol. 17, no. 3, pp. 261-272

(2020).

[104] S. Hong, "A silicon surface ion-trap chip with dielectric sidewalls shielded by metal films," *Ph.D. dissertation, Seoul National University* (2017).

[105] 박윤재, "이온 트랩의 RF 전압 조정을 위한 FPGA 기반의 피드백 컨트롤러 및 모듈화된 전압 분배기", *Ph.D. disseration, Seoul National Univerisity* (2021).

[106] Y. Ibaraki, U. Tanaka, and S. Urabe, "Detection of parametric resonance of trapped ions for micromotion compensation," *Applied Physics B*, vol. 105, no. 4, pp. 219-223 (2011).

[107] R. Noek, T. Kim, E. Mount, S. Y. Baek, P. Maunz, and J. Kim, "Trapping and cooling of ^{174}Yb^{+} ions in a microfabricated surface trap," *Journal of Korean Physical Society*, vol. 63, no. 4, pp. 907-913 (2013).

[108] R. Saito, K. Saito, and T. Mukaiyama, "Measurement of ion displacement via RF power variation for excess micromotion compensation," *Journal of Applied Physics*, vol. 129, no. 12, pp. 124302 (2021).

[109] D. J. Berkeland, J. D. Miller, J. C. Bergquist, W. M. Itano, and D. J.

Wineland, “Minimization of ion micromotion in a Paul trap,” *Journal of Applied Physics*, vol. 83, no. 10, pp. 5025-5033 (1998).

[110] C. Monroe, D. M. Meekhof, B. E. King, S. R. Jefferts, W. M. Itano, D. J. Wineland, and P. Gould, “Resolved-sideband Raman cooling of a bound atom to the 3D zero-point energy,” *Physical Review Letters*, vol. 75, no. 22, pp. 4011 (1995).

Abstract (in Korean)

최근 평면 이온 트랩을 기반으로 한 양자 컴퓨터의 개발은 평면 이온 트랩의 확장성과 재현성, 광학 및 전자 부품의 집적 가능성 덕분에 많은 관심을 받고 있다. 하지만, 평면 이온 트랩에 포획된 이온은 주변 전극과 가깝기 때문에, 주변 전기장의 변화에 매우 취약하다는 문제가 있다. 특히, 이온 트랩 표면에서 유도되는 표유 전기장은 포획된 이온의 원하지 않는 미세 진동을 유발하여, 이온을 이용한 양자 게이트 동작의 신뢰도에 악영향을 미칠 수 있다.

레이저로 인해 유도된 표유 전하는 이온의 위치에 표유 전기장을 가하는 원인 중 하나다. 레이저로 인해 유도된 표유 전하는 일반적으로 전극 표면에서 방출된 광전자가 주변 절연층에 축적되며 발생한다. 레이저로 인해 유도된 표유 전하가 발생하는 양은 시간에 따라 변하기 때문에, 관측된 표유 전기장을 한 차례 상쇄하는 것만으로는 오랜 시간 동안 포획된 이온을 안정적으로 유지하기 어려워, 주기적으로 표유 전기장을 보상해야 한다. 또한, 이온 트랩은 일반적으로 고주파 레이저를 사용하기 때문에, 항상 레이저로 인해 표유 전하가 발생할 가능성이 존재한다. 현재는 레이저로 인해 유도된 표유 전하가 의심되는 경우, 표유 전하의 위치를 알 수 없기 때문에, 비효율적으로 시행 착오를 거쳐 이온의 위치나 레이저 경로를 조절함으로써 표유 전하의 발생을 억제하고 있다.

본 학위 논문에서는 평면 이온 트랩에 레이저로 인해 유도된 전하의 위치를 추정하는 방법을 제안하였다. 이를 위해, 표유 전하가 발생했을 때 트랩 전위가 어떻게 변하는 지 이론적인 모델을 세운 후, 이론 모델로부터 이온의 주파수가 어떻게 변하는 지 도출하였다. 이 모델을 특정 조건 하에 역으로 이용하여, 관측된 주파수의 변화로부터 표유 전하의 위치를 추정할 수 있다. 구체적으로, 평면 이온 트랩에서는 여러 이온의 위치에서 주파수의 변화를 측정할 수 있기 때문에, 표유 전하의 위치를 유일하게 결정하기 위해 필요한 횟수만큼 주파수 변화 측정 결과를 확보할 수 있다고 가정하였다. 제안하는 방법의 실효성을 검증하기 위해, 표유 전하가 다양한 위치에서 발생한 상황에 대하여 시뮬레이션을 진행한 후, 여러 이온의 위치에서 주파수의 변화를 관측하였다. 표유 전하의 위치는 시뮬레이션 결과에서 관측된 주파수로부터 추정한 후, 이론 모델을 통해 계산한 결과와 비교하였다. 실험적으로도 개발한 방법의 효용성을 검증하기 위해, 레이저를 이용하여 의도적으로 전하를 생성한 후, 이온의 위치를 옮겨가며 주파수의 변화를 측정하였다. 측정 결과로부터 생성된 전하의 위치를 추정하였고, 추정된 전하의 위치는 카메라를 통해 확인할 수 있는 레이저를 조사한 위치와 오차 범위 이내로 일치하였다. 본문에서 개발한 방법을 이용하여 레이저로 인해 유도된 표유 전하의 위치를 파악함으로써 표유 전하를 효율적으로 억제할 수 있을 것으로 예상되며, 나아가 이온 트랩 기반의 양자 컴퓨팅 시스템의 신뢰성과 안정성을 효율

적으로 향상시킬 수 있을 것으로 기대된다.